UNIVERSIDADE FEDERAL DE MINAS GERAIS

Escola de Engenharia

Programa de Pós-Graduação em Engenharia Elétrica

João Henrique de Oliveira

Xyn-converter Used in Isolated Two-phase Three-wire AC Power Grids

Belo Horizonte

2024

João Henrique de Oliveira

XYN-CONVERTER USED IN ISOLATED TWO-PHASE THREE-WIRE AC POWER GRIDS

Tese apresentada ao Programa de Pós-Graduação em Engenharia Elétrica da Universidade Federal de Minas Gerais, como requisito parcial à obtenção do título de Doutor em Engenharia Elétrica.

Orientador: Prof. Dr. Danilo Iglesias Brandão
Coorientador: Prof. Dr. Allan Fagner Cupertino

Belo Horizonte
2024

Oliveira, João Henrique de.
O48x *Xyn*-converter used in isolated two-phase three-wire AC power grids [recurso eletrônico] / João Henrique de Oliveira. - 2024.
1 recurso online (129 f. : il., color.) : pdf.

Orientador: Danilo Iglesias Brandão.
Coorientador: Allan Fagner Cupertino.

Tese (doutorado) - Universidade Federal de Minas Gerais, Escola de Engenharia.

Bibliografia: f. 121-128.
Exigências do sistema: Adobe Acrobat Reader.

1. Engenharia elétrica - Teses. 2. Redes elétricas - Teses. 3. Conversores eletrônicos - Teses. 4. Redes - Teses. 5. Confiabilidade (Engenharia) - Teses. 6. Potência reativa (Engenharia elétrica) - Teses. 7. Semicondutores - Teses. I. Brandão, Danilo Iglesias. II. Cupertino, Allan Fagner. III. Universidade Federal de Minas Gerais. Escola de Engenharia. IV. Título.

CDU: 621.3(043)

Ficha catalográfica elaborada pela Bibliotecária Ângela Cristina Silva - CRB-6/2361
Biblioteca Prof. Mário Werneck, Escola de Engenharia da UFMG.

UNIVERSIDADE FEDERAL DE MINAS GERAIS
ESCOLA DE ENGENHARIA
PROGRAMA DE PÓS-GRADUAÇÃO EM ENGENHARIA ELÉTRICA

FOLHA DE APROVAÇÃO

"XYN-CONVERTER USED IN ISOLATED TWO-PHASE THREE-WIRE AC POWER GRIDS"

JOÃO HENRIQUE DE OLIVEIRA

Tese de Doutorado submetida à Banca Examinadora designada pelo Colegiado do Programa de Pós-Graduação em Engenharia Elétrica da Escola de Engenharia da Universidade Federal de Minas Gerais, como requisito para obtenção do grau de Doutor em Engenharia Elétrica. Aprovada em 29 de fevereiro de 2024. Por:

Prof. Dr. Danilo Iglesias Brandão
DEE (UFMG) - Orientador

Prof. Dr. Allan Fagner Cupertino - Coorientador
DEE (UFJF)

Prof. Dr. Pedro Gomes Barbosa
DEE (UFJF)

Prof. Dr. Fabrício Bradaschia
DEE (UFPE)

Prof. Dr. Lenin Martins Ferreira Morais
DELT (UFMG)

Prof. Dr. Victor Flores Mendes
DEE (UFMG)

Documento assinado eletronicamente por **Victor Flores Mendes**, **Professor do Magistério Superior**, em 29/02/2024, às 16:18, conforme horário oficial de Brasília, com fundamento no art. 5º do Decreto nº 10.543, de 13 de novembro de 2020.

Documento assinado eletronicamente por **Lenin Martins Ferreira Morais**, **Professor do Magistério Superior**, em 29/02/2024, às 16:19, conforme horário oficial de Brasília, com fundamento no art. 5º do Decreto nº 10.543, de 13 de novembro de 2020.

Documento assinado eletronicamente por **Danilo Iglesias Brandao**, **Professor do Magistério Superior**, em 01/03/2024, às 10:08, conforme horário oficial de Brasília, com fundamento no art. 5º do Decreto nº 10.543, de 13 de novembro de 2020.

Documento assinado eletronicamente por **Fabrício Bradaschia**, **Usuário Externo**, em 04/03/2024, às 11:18, conforme horário oficial de Brasília, com fundamento no art. 5º do Decreto nº 10.543, de 13 de novembro de 2020.

Documento assinado eletronicamente por **Pedro Gomes Barbosa**, **Usuário Externo**, em 04/03/2024, às 11:26, conforme horário oficial de Brasília, com fundamento no art. 5º do Decreto nº 10.543, de 13 de novembro de 2020.

Documento assinado eletronicamente por **Allan Fagner Cupertino**, **Usuário Externo**, em 04/03/2024, às 16:15, conforme horário oficial de Brasília, com fundamento no art. 5º do Decreto nº 10.543, de 13 de novembro de 2020.

A autenticidade deste documento pode ser conferida no site https://sei.ufmg.br/sei/controlador_externo.php?acao=documento_conferir&id_orgao_acesso_externo=0, informando o código verificador **3063247** e o código CRC **145162DD**.

Referência: Processo nº 23072.211383/2024-87 SEI nº 3063247

À minha família e amigos.

Acknowledgment/Agradecimentos

In order to reach all the important people, initially I will write some words in Portuguese.

Agradeço prmeiramente à minha mãe Sônia pelo carinho. Tenho muita sorte de ter você em minha vida. Também à minha irmã Ana Carolina, minha primeira e mais querida amiga. Esse trabalho é dedicado à vocês.

Agradeço ao meu orientar Danilo Iglesias Brandão pela brilhante condução desse trabalho. É inspirador a forma que você orienta seus alunos. Obrigado pelo zelo e cuidado comigo e com meu trabalho. Ao meu co-orientador e amigo Allan Fagner Cupertino meu muito obrigado pela atenção e ideias para a realização desse trabalho. Seu talento e visão de trabalho foram essenciais para mim e para o resultado dessa tese.

Agradeço aos amigos Erick Brito e Rodrigo de Barros pela ajuda direta na construção da tese. O conhecimento e a colaboração de vocês foi indispensável no trabalho.

Agradeço aos companheiros de GESEP pela ajuda e disponibilidade sempre que precisei. Aos amigos do Laboratório Tesla Engenharia de Potência, obrigado por tornar meus dias de trabalho leves, divertidos e produtivos! Antônio, Dener, Diogo, Gabriel, Gideon, Gustavo, João Marcus, Kassiane, Lucas Savoi, Mari, Noah, Rodrigo, Tamires, obrigado por cada café, almoço e prosa divididos durante o doutorado.

Agradeço à Coordenação de Aperfeiçoamento de Pessoal de Nível Superior pelo financiamento de parte desse projeto. Agradeço também à Universidade Federal de Minas Gerais pela estrutura ofrecida para realização desse trabalho.

Now, some words in English.

I would like to thank my advisor at the University of Wisconsin, Giri Venkataramanan, for the support and care he provided me during my time as a visiting student in the United States. I consider myself lucky to have encountered someone as competent and caring for his students as you are. Thank you for the technical expertise that elevated the level of this work; it was a pleasure working with you. I also thank Professor Daniel Ludois for his partnership on the project I worked on during my stay at UW.

I extend my gratitude to my friends in Room 2568 Anvar, Feida, Justin, Nathan, Sangwhee, Shalini, Wenda, for the good conversations and for every shared Spotted Cow. I especially thank Jamie Turnbull for her patience with me and for her essential role in this work.

I would like to thank WEMPEC for the infrastructure provided for conducting

experiments for this dissertation. I thank the staff, Kathy, Kelly, and Pia, for their diligence and excellent work with WEMPEC students.

I also want to express my gratitude to my Wisconsin family, the residents of Coop Summit Avenue. Alyssa, Andy, Austin, Autumn, Colleen, Frank, Hà, Jorge, Kai, Lovely, Mingxin, Nate, Noelle, Ro, Selena, Sherry, Shuta, Susan, and Zach. Thank you for welcoming me during the 10 months we lived together. Every house meeting, movie session, ice cream and conversation at the dinner table were very special to me. I miss you all, especially Nora! I also thank my Brazilian friends Giuliana, Lucas, Mirella, Tuwilê, and Letícia for their friendship and for helping to alleviate the *saudade*.

"Um passo à frente e você não está mais no mesmo lugar."
(Chico Science)

RESUMO

Redes elétricas CA isoladas são soluções viáveis para energizar comunidades remotas, geralmente baseadas em energias renováveis e armazenadores de energia, conectadas por conversores eletrônicos de potência que exigem alta confiabilidade. O elemento-chave de tal sistema é o conversor formador de rede, que fornece magnitude de tensão e frequência aos demais elementos, como cargas. Assim, esta tese propõe o conversor-xyn bifásico a três fios (2Φ3W) aplicado a um estudo de caso em comunidades isoladas ribeirinhas na região amazônica brasileira. A tese compara o estresse de corrente de conversores formadores de rede (GFC), considerando três configurações diferentes de rede em termos de ângulos de deslocamento entre as tensões de fase: 90° ($\alpha\beta n$-GFC); 120° (abn-GFC) and 180° (xyn-GFC). Além disso, são obtidas expressões analíticas para o estresse de corrente nos semicondutores e no capacitor do barramento CC para cada conversor em condições de carga generalizada, i.e., balanceada e desbalanceada. A análise de vida útil do conversor formador de rede indica que o xyn-GFC tem o menor desgaste. Além disso, este trabalho destaca a influência de componentes harmônicas de alta frequência na corrente RMS do capacitor do barramento CC. O xyn-GFC demonstra uma menor probabilidade de falha do capacitor em comparação com os outros conversores, mesmo apresentando componentes de corrente de baixa frequência mais altos. Uma análise de sensibilidade mostra que o conversor formador de rede xyn-GFC pode aumentar sua potência de saída em 12% ou reduzir o volume do dissipador de calor em 25% para atingir a mesma vida útil B_{10} que o abn-GFC (considerado como referência) em condições nominais. Um experimento é conduzido usando um conversor de ponte completa e IGBTs discretos para medir as perdas de potência nos semicondutores e a temperatura de case dos IGBTs. Em comparação com o $\alpha\beta n$-GFC, o xyn-GFC mostra perdas de potência 44% menores, e o abn-GFC mostra perdas de potência 18% inferiores. Por fim, a análise de estresse térmico é validada por meio de um protótipo de conversor 2Φ3W com módulo semicondutor aberto. Para os conversores avaliados, o xyn-GFC tem o menor estresse térmico para condições de carga balanceada e desbalanceada, portanto, indicandi uma vida útil mais longa. A validação experimental mostra que a temperatura média do xyn-GFC é 19,4% e 23,3% menor do que os conversores abn-GFC e $\alpha\beta n$-GFC em condições de carga balanceada, respectivamente.

Palavras-chave: conversor formador de rede; redes isoladas CA; confiabilidade.

ABSTRACT

Isolated electric AC power grids are feasible solutions to energize remote communities, usually based on renewables and energy storage devices, interfaced by power electronics converters that require high reliability. The key element of such a system is the grid-forming converter that provides the voltage magnitude and frequency to other devices, such as loads. Therefore, this dissertation proposes the two-phase three-wire (2Φ3W) *xyn*-converter applied in a case study of isolated riverside communities in the Brazilian Amazon region. This dissertation compares the current stresses of grid-forming converters (GFC) under an isolated grid mission profile, considering three different grid configurations in terms of the displacement angle between the voltage in the phases: 90° ($\alpha\beta n$-GFC); 120° (*abn*-GFC) and 180° (*xyn*-GFC). Additionally, analytical expressions for current stress through the semiconductors and the DC-link capacitor are obtained for each converter under balanced and unbalanced load conditions. The lifetime analysis of the grid-forming converter indicates that the *xyn*-GFC has the lowest wear-out. Furthermore, this work highlights the influence of high-frequency components on the RMS current of the DC-link capacitor. The *xyn*-GFC demonstrates a lower probability of capacitor failure compared to the other converters, even with higher low-frequency components. A sensitivity analysis shows that the *xyn*-GFC can increase its output power in 12% or reduce its heatsink volume in 25% to achieve the same wear-out B_{10} lifetime as the *abn*-GFC (i.e., benchmark) under nominal conditions. An experiment is conducted using a full-bridge converter and discrete IGBTs to measure the power losses in the semiconductors and the case temperature of the IGBTs. Compared with the $\alpha\beta n$-converter, the *xyn*-converter shows 44% lower power losses, and the *abn*-converter shows 18% lower power losses. Finally, the thermal stress analysis is validated by means of a 2Φ3W converter prototype with an open semiconductor module. For the evaluated converters, the *xyn*-GFC has the lowest thermal stress for balanced and unbalanced load conditions and therefore the longest lifetime. Experimental validation shows that the average temperature of the *xyn*-GFC is 19.4% and 23.3% lower than both the *abn*-GFC and the $\alpha\beta n$-GFC under balanced load conditions.

Key-words: grid-forming converter; isolated AC power grids; reliability.

List of Figures

Figure 1 – People without access to electricity worldwide, 2012-2022 (IEA, 2022). 27
Figure 2 – The global population served by off-grid renewable energy solutions (IRENA, 2022). 28
Figure 3 – Total number of isolated locations and the number of people served by isolated systems in each state (EPE, 2022). 29
Figure 4 – Location of Mipindiaú. 30
Figure 5 – 2Φ3W system connected to a three-phase four-wire grid. Adapted from (Furtado; Barbosa, 2019). 32
Figure 6 – Isolated AC grids: (a) Distributed converters. (b) Central converter . . 38
Figure 7 – Examples of hybrid converters. 39
Figure 8 – The 'bathtub' curve. 43
Figure 9 – (a) Frequency of occurrence of fault elements in converters. (b) Stress sources of the faults in converters (Choi; Blaabjerg; Lee, 2015). 44
Figure 10 – Structure of IGBT module(Callegari et al., 2019). 45
Figure 11 – Structure of a grid-forming converter for 2Φ3W isolated ac power grid. 48
Figure 12 – Phase-to-neutral voltages of the 2Φ3W: (a) $\alpha\beta n$-system. (b) *abn*-system. (c) *xyn*-system. 49
Figure 13 – Phase current of the 2Φ3W: (a) $\alpha\beta n$-system.(b) *abn*-system. (c) *xyn*-system. *Remark*: These results were obtained based on the parameters of Table 4 and rated power injection. 50
Figure 14 – (a) Instantaneous power in $\alpha\beta n$, *abn*, *xyn*-systems. (b) Voltage in DC-link capacitor in $\alpha\beta n$, *abn*, *xyn*-systems. *Remark*: These results were obtained based on the parameters of Table 4 and rated power injection. 51
Figure 15 – DC-link capacitor current: (a) $\alpha\beta n$-system.(b) *abn*-system. (c) *xyn*-system. *Remark*: These results were obtained based on the parameters of Table I and rated power injection. 52
Figure 16 – Flowchart for the lifetime evaluation of semiconductor power devices and DC-link capacitors. 53
Figure 17 – Thermal model based on Foster model. 54
Figure 18 – Electro-thermal circuit for junction temperature estimation using the hybrid model with Cauer and Foster model. 55
Figure 19 – Electro-thermal circuit for estimating the hot-spot temperature of the capacitor. 56
Figure 20 – Communities load profile: (a) Marabá. (b) Monte Sinai. (c) Pagodão. (d) São Thomé. (e) Três Unidos. 61
Figure 21 – Mission profile created using the 5 communities. 61

Figure 22 – Power profiles: (a) One year load of a riverside community. (b) One year PV plant generation. (c) One year 2Φ3W GFC power. 62
Figure 23 – Control of the isolated 2Φ3W grid-forming converter. 63
Figure 24 – (a) Thermal measurement of the prototype semiconductors. (b) Top view of the open semiconductor module FP25R12KE3 by Infineon. In yellow are highlighted the phase semiconductors and in blue the neutral semiconductors. 64
Figure 25 – (a) Experimental test bench. (b) Detailed three-phase full-bridge converter of the experimental test bench. 64
Figure 26 – Power analyzer connections for semiconductor losses measurement. . . 66
Figure 27 – 2Φ3W reference signals for SPWM. θ is the displacement angle of the voltage references, which can assume 90°, 120° or 180°. Regions A, B, and C are a division of half of the fundamental period, used to calculate the current stress of the DC-link capacitor. 68
Figure 28 – Collector currents of IGBTs S_1 and S_2. 68
Figure 29 – Phase current of the 2Φ3W converters: $\alpha\beta n$, *abn*, and *xyn*. Balanced load conditions. 70
Figure 30 – RMS current through the IGBTs. Switches S_5-S_6 in the *xyn*-system have zero current value. ϕ is the displacement angle between voltage and current. 75
Figure 31 – RMS current through the diodes. Switches S_5-S_6 in the *xyn*-system have zero current value. ϕ is the displacement angle between voltage and current. 76
Figure 32 – RMS current through the IGBTs for different unbalanced factor. *Remark*: The RMS current in the phase legs is the same for all the considered converters. The main differences are observed in the neutral leg devices. 77
Figure 33 – RMS current through the active switches of the neutral leg (S_5 and S_6). 77
Figure 34 – RMS current through the active switches of the neutral leg (S_5 and S_6) considering I_j=I_k, and $\phi_j \neq \phi_k$. 78
Figure 35 – RMS current through the active switches of the neutral leg (S_5 and S_6) considering I_j=$I_k = 1$, for different ϕ_k and: (a) $\phi_j = -\pi$, (b) $\phi_j = -\frac{\pi}{2}$ 78
Figure 36 – Top view of the RMS current through the active switches of the neutral leg (S_5 and S_6) considering I_j=I_k, and $\phi_j \neq \phi_k$. 79
Figure 37 – Top view of the RMS current through the active switches of the neutral leg (S_5 and S_6) considering I_j=I_k, and -0.6435<ϕ<0.6435 rad. 80
Figure 38 – Detailed PWM signals over one switching period:(a) region A. (b) region B. (c) region C. 81
Figure 39 – 2Φ3W reference signals for *xyn*-converter. 85
Figure 40 – RMS current of the DC-link capacitor: (a) $\alpha\beta n$; (b) *abn* and (c) *xyn*. . 87

Figure 41 – Capacitor current of PLECS simulation: (a) $\alpha\beta n$-system. (b) *abn*-system. (c) *xyn*-system. (d) Capacitors current harmonic spectrum. 87
Figure 42 – RMS current through the DC-link capacitor for different unbalanced factor. 88
Figure 43 – (a) RMS current through the DC-link capacitor for different unbalance factor and different displacement angle. (b) Top view of RMS current through the DC-link capacitor. 89
Figure 44 – RMS current in DC-link capacitor under unbalanced conditions of: (a) $\alpha\beta n$-GFC. (b) *abn*-GFC. (c) *xyn*-GFC. (d) Three GFCs types. *Remark*: The dots are the simulated points in PLECS. 90
Figure 45 – Top view of the RMS current through the DC-link capacitor for different angle displacement. 91
Figure 46 – RMS current through the DC-link capacitor considering I_j=$I_k = 1$, for different ϕ_k and: (a) $\phi_j = -\pi$, (b) $\phi_j = -\frac{\pi}{2}$ 91
Figure 47 – Setup used for HIL results. 92
Figure 48 – Results in hardware-in-the-loop. Phase current and capacitor current of: (a) $\alpha\beta n$-GFC. (b) *abn*-GFC. (c) *xyn*-GFC. 93
Figure 49 – Current measurements in the experimental results in the discrete IGBT setup. 93
Figure 50 – Experimental results in reduced-scale prototype. Phase current and DC-link ripple current of: (a) $\alpha\beta n$-GFC. (b) *abn*-GFC. (c) *xyn*-GFC. . 94
Figure 51 – (a) Harmonic spectrum of the DC-link capacitor current obtained by means of the experimental test bench. (b) Harmonic spectrum of the DC-link capacitor current obtained by simulation o PLECS. *Both scenarios consider open loop operation.* 95
Figure 52 – Power profiles: (a) One year PV plant generation. (b) Two day PV plant generation. (c) One year load power. (d) Two day load power. (e) One year grid-forming inverter power. (f) Two day grid-forming inverter power. 96
Figure 53 – Average junction temperature: (a) IGBT S_1. (b) IGBT S_5. (c) DC-link capacitor. 97
Figure 54 – Monte Carlo simulations of the components: (a) IGBT S_1. (b) IGBT S_5. (c) DC-link capacitor. 98
Figure 55 – (a) IGBTs and Capacitors unreliability functions. (b) Overall converter level unreliability functions. 99
Figure 56 – Unreliability functions for different output power levels in the: (a) $\alpha\beta n$-GFC. (b) *xyn*-GFC. Sensitivity analysis of the output power for: (c) $\alpha\beta n$-GFC. (d) *xyn*-GFC. 100
Figure 57 – Relation between specific cost and rated power for a total cost of €1000. 101

Figure 58 – Unreliability functions for different thermal resistance in the: (a) $\alpha\beta n$-GFC. (b) *xyn*-GFC. Sensitivity analysis of the thermal resistance for: (c) $\alpha\beta n$-GFC. (d) *xyn*-GFC. 102
Figure 59 – Relation between volume and thermal resistance for a CSPI of 5 W/K/L. 103
Figure 60 – Semiconductor losses of the 2Φ3W converter considering the $\alpha\beta n$, *abn* and *xyn* converters. 104
Figure 61 – Case temperature on IGBTs S_1 and S_2 of the 2Φ3W converter considering the $\alpha\beta n$, *abn* and *xyn* converters. 104
Figure 62 – (a) IGBT S_1 unreliability function. (b) IGBT S_5 unreliability function. (c) Overall converter level unreliability function considering all semiconductors. 105
Figure 63 – Thermal images of the semiconductors of the GFC operating on: (a) $\alpha\beta n$-GFC; (b) *abn*-GFC; (c) *xyn*-GFC; (d) *xyn*-GFC with different temperature scale. 107
Figure 64 – Histogram of temperatures in thermal images for balanced load conditions. 108
Figure 65 – $\alpha\beta n$ converter operating under: (a) balanced load conditions, flowing 250W in each phase; (b) unbalanced load conditions, flowing 250W in phase j and 75 W in phase k. 109
Figure 66 – *abn* converter operating under: (a) balanced load conditions, flowing 250W in each phase; (b) unbalanced load conditions, flowing 250W in phase j and 75 W in phase k. 109
Figure 67 – *xyn* converter operating under: (a) balanced load conditions, flowing 250W in each phase; (b) unbalanced load conditions, flowing 250W in phase j and 75 W in phase k. 110
Figure 68 – 2Φ3W converter immersed in oil. 114
Figure 69 – Current during the experiment for: (a) $\alpha\beta n$-GFC. (b) *abn*-GFC. (c) *xyn*-GFC. 115
Figure 70 – Case temperature of the IGBTs S_1 and S_5 for: (a) air converter. (b) oil-immersed converter. 115
Figure 71 – Hi-Pot test on the PCB. 117

List of Tables

Table 1 – Conditions of low-voltage 2Φ3W power supplying in Brazil. Adapted from Furtado (2019). 32
Table 2 – Control methods for inverter-based microgrids. Adapted from Fani et al. (2022). 39
Table 3 – Comparison of correlate papers in literature: grid configuration, result types, analytical current stress and reliability method. 47
Table 4 – Parameters of the isolated 2Φ3W GFC. 65
Table 5 – Proposed analytical expressions of current stresses on the power semiconductor devices of 2Φ3W converter. 75
Table 6 – Analytical expressions of current stress of the DC-link capacitor for 2Φ3W GFCs. 86
Table 7 – RMS DC-link capacitor current in PLECS simulations, HIL and experimental test bench. 95
Table 8 – Key Thermal and Physical Properties of Air at nominal T= 26.85 ^{o}C (300K) and Cargill FR3 (Nellis; Klein, 2021) (Martin, 2008). 113
Table 9 – Hi-Pot results for dc and ac voltage application at the PCB terminals. . 117

Acronyms

2Φ3W two-phase three-wire. 12, 13, 15, 16, 24, 31–35, 37, 39–41, 48–50, 52, 54, 55, 62, 63, 65–68, 74–76, 79, 85, 86, 88, 89, 111, 114, 118–120

AC Alternating Current. 12, 33, 37, 38, 41, 48, 116

APF active power filter. 40

BESS batery energy storage systems. 37, 48

CDF cumulative density function. 59

D-STATCOM Static Synchronous Compensators. 40

DC Direct Current. 13, 14, 16, 25, 40, 41, 45, 48, 51, 52, 67, 68, 79, 81–91, 116

DCB direct copper-bonded. 44

ESR equivalent series resistance. 54, 55

IEA International Energy Agency. 27

IGBT Insulated-gate bipolar transistor. 12, 15, 24, 44, 45, 52, 54, 55, 58, 63, 65, 66, 69, 98, 103, 106, 114–116

IRENA International Renewable Energy Agency. 27

MPPT Maximum Power Point Tracking. 40

PDF Weibull Probability Density Function. 59

PoF physics of failure. 43

PV photovoltaic. 37, 40, 45, 46, 48, 60

SHS solar home system. 27

Si-IGBT Silicon insulated-gate bipolar transistor. 45

SiC silicon carbide. 45, 46

SIN Sistema Interconectado Nacional. 28, 30

SPWM sinusoidal pulse-width modulation. 67, 76, 79

SRC series resonant converter. 45

SVC Static Var Compensators. 40

UPS Uninterruptible Power Supplies. 33

List of symbols

β_1	temperature fluctuation coefficient
β_2	minimum junction temperature coefficient
β_3	pulse duration coefficient
β_4	current per bond-foot coefficient
β_5	blocking voltage coefficient
β_6	bond-wire diameter coefficient
β_w	shape parameter of the Weibull Probability Density Function
ΔT_j	temperature cycling
δ	duty cycle
δ_{d_1}	duty cycle for the diode d_1
$\zeta_{A,B,C}$	percentage of regions A, B and C, respectively
δ_{S_1}	duty cycle for the IGBT S_1
η_w	scale parameter of the Weibull Probability Density Function
θ	angular displacement between phase voltages
σ	unbalance factors
$\tau_{0,A,B,C}$	angles of the border of each region defined over half modulation signal period for the current stress calculation of the DC-link capacitor
ϕ_j	angular displacement between voltage and current in phase j
ϕ_k	angular displacement between voltage and current in phase k
ω	line angular frequency
ψ_i	start of the integration period for average and RMS current calculation
ψ_f	end of the integration period for average and RMS current calculation
A	Technology Factor
C	DC-link capacitor

C_{th}	thermal capacitance
D	bond-wire diameter
E_{off}	turn-off energy
E_{on}	turn-on energy
E_{rec}	recovery energy in the diode
$f(x)$	Weibull Probability Density Function
$F(x)$	unreliability function
$F_m(x)$	reliability computed by the CDF for each device
f_n	grid fundamental frequency
F_{sys}	converter-level lifetime consumption
f_{sw}	switching frequency
H	number of components of the converter
i	number of nodes in the Foster network
I	generic amplitude peak of phase currents
I_{AVG}	average current in power devices
$I_{AVG,(A,B,C)}$	average DC-link current in regions A, B or C
I_{AVG,d_1}	average current stress for the diode d_1
$I_{dc,AVG}$	total average DC-link current
I_{AVG,S_1}	average current stress for the diode S_1
I_{AVG,S_5}	average current stress for the diode S_5
$I_{AVG,S_5,\alpha\beta n}$	average current stress for the diode S_5 in the $\alpha\beta n$-converter
$I_{AVG,S_5,abn}$	average current stress for the diode S_5 in the abn-converter
$I_{AVG,S_5,xyn}$	average current stress for the diode S_5 in the xyn-converter
I_{bf}	current per bond-foot
i_c	collector current
i_dc	DC-link current

i_f	forward current in diode
i_j	current in phase j
I_j	amplitude peak current in phase j
i_k	current in phase k
I_k	amplitude peak current in phase j
i_n	current in neutral conductor
I_{RMS}	RMS current in power devices
$I_{RMS,(A,B,C)}$	RMS DC-link current in regions A, B or C
I_{RMS,d_1}	RMS current stress for the diode d_1
$I_{dc,RMS}$	total RMS DC-link current
I_{RMS,S_1}	RMS current stress for the IGBT S_1
I_{RMS,S_5}	RMS current stress for the IGBT S_5
$I_{RMS,S_5,\alpha\beta n}$	RMS current stress for the diode S_5 in the $\alpha\beta n$-converter
$I_{RMS,S_5,abn}$	RMS current stress for the diode S_5 in the abn-converter
$I_{RMS,S_5,xyn}$	RMS current stress for the diode S_5 in the xyn-converter
L	capacitor lifetime under the hotspot temperature
L_0	test operating voltage of capacitors
LC_s	semiconductor or capacitor lifetime consumption
m	number of mission profile points
M	modulation index
n	voltage stress exponent
N_f	number of cycles to failure
p	instantaneous power
$p_{\alpha\beta n}$	instantaneous power for the $\alpha\beta n$ system
p_{abn}	instantaneous power for the abn system
$P_{c,diode}$	conduction loss in diode

$P_{c,IGBT}$	conduction loss in IGBT
P_{loss}	power losses dissipated on the generic power semiconductor device
$P_{loss,cap}$	loss in the capacitor
$P_{loss,diode}$	total losses in diode
$P_{loss,IGBT}$	total losses in IGBT
$P_{sw,diode}$	switching loss diode
$P_{sw,IGBT}$	switching loss IGBT
p_{xyn}	instantaneous power for the *xyn* system
R_{ha}	equivalent series resistance from the hotspot to ambient
R_{th}	thermal resistance
S_1	upper IGBT in phase j
S_2	lower IGBT in phase j
S_3	upper IGBT in phase k
S_4	lower IGBT in phase k
S_5	upper IGBT in phase n
S_6	lower IGBT in phase n
t_0	start time
$T_{0,1,2,3}$	intervals for current stress calculation of DC-link capacitor
T_a	ambient temperature
T_h	capacitor hot-spot temperature
T_{jm}	average junction temperature
t_{on}	heating time
$t_{on,long}$	heating time for long-cycles calculation
$t_{on,short}$	heating time for short-cycles calculation
T_s	switching period
T_{sg}	period of the collector current in IGBT

$T_{sg,d}$	period of the forward current in the diode
v_c	test operating voltage for capacitors
v_{ce}	collector-emitter voltage
v_{cr}	carrier signal
v_{dc}	DC-link voltage
V_{LN}	line-to-neutral peak voltage
v_f	forward voltage in diode
v_j	phase-to-neutral voltage in phase j
V_j	amplitude peak voltage in phase j
$v_{(j,k,n),n}$	modulation signals
v_k	phase-to-neutral voltage in phase k
V_k	amplitude peak voltage in phase j
V_n	rated voltage test condition for capacitors
V_{sd}	blocking voltage of the power semiconductor device
x	operation time
Z_{th}	generic thermal impedance
$Z_{th(ch)}$	transient thermal impedance between the case and heatsink
$Z_{th(ha)}$	transient thermal impedance between the heatsink and environment
$Z_{th(jc)}$	transient thermal impedance between the junction and case

Contents

1	**INTRODUCTION**	**27**
1.1	**Contextualization**	**27**
1.2	**Motivation and Relevance**	**31**
1.3	**Objectives**	**33**
1.3.1	Main objectives	33
1.3.2	Methodology	33
1.4	**Contributions**	**34**
1.5	**Organization of this Ph.D. dissertation**	**34**
1.6	**Publications**	**35**
1.6.1	Journal Papers	35
1.6.2	Conference Papers	35
1.6.3	Participation in other work	36
2	**LITERATURE REVIEW**	**37**
2.1	**Isolated power grid systems**	**37**
2.2	**Converter control in 2Φ3W systems**	**39**
2.3	**Reliability**	**41**
2.3.1	Reliability and 2Φ3W systems	45
2.4	**Chapter closure**	**46**
3	**TWO-PHASE THREE-WIRE POWER GRIDS**	**48**
3.1	**Basics of Two-phase Three-wire circuits**	**48**
3.2	**Mission profile-based reliability analysis**	**52**
3.2.1	Power losses look-up table	52
3.2.2	Thermal model	54
3.2.3	Long and short-cycles computation	55
3.2.4	Lifetime model and Miner's Rule	57
3.2.5	Monte Carlo analysis	58
3.3	**Case Study**	**60**
3.3.1	Characterization of Riverside Communities in Amazon Region	60
3.3.2	Converter design for PLECS simulations	60
3.3.3	Open module setup	63
3.3.4	Discrete IGBT setup	63
3.4	**Chapter closure**	**66**

4 CURRENT STRESSES EVALUATION IN TWO-PHASE THREE-WIRE CONVERTERS 67
4.1 Proposed semiconductors current stresses evaluation for general load condition 67
4.1.1 $\alpha\beta n$ semiconductors current stress evaluation 68
4.1.1.1 Current stress for amplitude current unbalance in $\alpha\beta n$-converters 71
4.1.1.2 Current stress for different angle displacements unbalance in $\alpha\beta n$-converters 71
4.1.2 *abn* semiconductors current stress evaluation 72
4.1.2.1 Current stress for amplitude current unbalance in *abn*-converters 72
4.1.2.2 Current stress for different angle displacements unbalance in *abn*-converters 73
4.1.3 *xyn* semiconductors current stress evaluation 73
4.1.3.1 Current stress for amplitude current unbalance in *xyn*-converters 73
4.1.3.2 Current stress for different angle displacements unbalance in *xyn*-converters 74
4.1.4 Balanced load conditions - semiconductors 74
4.1.5 Unbalanced load conditions - semiconductors 76
4.1.5.1 Effect of current amplitude unbalance ($I_j \neq I_k$, $\phi_j = \phi_k$) 76
4.1.5.2 Effect of different angle displacements ($I_j = I_k$, $\phi_j \neq \phi_k$) 76
4.2 Proposed DC-link capacitors current stresses evaluation for general load condition 79
4.2.1 $\alpha\beta n$ DC-link capacitors current stress evaluation 83
4.2.2 *abn* DC-link capacitors current stress evaluation 84
4.2.3 *xyn* DC-link capacitors current stress evaluation 84
4.2.4 Balanced load conditions - capacitor 85
4.2.5 Unbalanced load conditions - capacitor 88
4.2.5.1 Effect of current amplitude unbalance ($I_j \neq I_k$, $\phi_j = \phi_k$) 88
4.2.5.2 Effect of different angle displacements ($I_j = I_k$, $\phi_j \neq \phi_k$) 88
4.3 Chapter closure 89

5 SIMULATION AND EXPERIMENTAL RESULTS 92
5.1 Discrete IGBTs setup results 92
5.1.1 HIL and experimental results 92
5.1.2 Wear-out Failure Probability 95
5.1.2.1 Sensitivity analysis 99
5.1.3 Power losses and semiconductor temperature 103
5.2 Open module setup results 105
5.2.1 Unreliability Results 105
5.2.2 Thermal Results 106
5.2.2.1 Balanced load conditions 106
5.2.2.2 Unbalanced load conditions 108
5.3 Further discussion 110

5.4 Chapter closure 111

6 OIL IMMERSED TWO-PHASE THREE-WIRE CONVERTER 112
6.1 Thermal Characteristics in Liquid-immersed Converters 113
6.2 Thermal Performance of Liquid-immersed Power Converter 114
6.3 Voltage Breakdown Analysis in Liquid-Immersed Power Converter 116
6.4 Chapter closure 117

7 CONCLUSIONS 119
7.1 Research perspectives 119

REFERENCES 121

1 Introduction

1.1 Contextualization

According to IEA (2022), the global population without access to electricity is expected to increase by almost 20 million in 2022, reaching a staggering 775 million people, as shown in Figure 1. This is the first worldwide increase in two decades since the International Energy Agency (IEA) began monitoring these figures. Most of this surge is observed in sub-Saharan Africa, where the number of people without electricity is approaching the levels last seen in 2013. Soaring fuel and food prices disproportionately affect those in developing regions, where resources to address these challenges are limited.

Off-grid solutions are facing tougher times as rising prices hurt customer demand. Key components such as solar panels, batteries, and inverters are becoming more expensive, especially as local currencies lose value compared to the dollar. The costs of solar and hybrid mini-grids have increased by at least 20% in 2022 compared to before the COVID-19 pandemic. The average price for a new solar home system (SHS) has jumped by about 30% since 2020, leading families to opt for smaller or less fancy systems. In 2021, sales of bigger SHS dropped by almost a third compared to their peak in 2019, the most significant declines occurring in East Africa. These problems are pushing many off-grid companies to the edge, and most of them are concerned that they will go out of business in the next three years (IEA, 2022).

The International Renewable Energy Agency (IRENA) estimates that approximately 179 million people had access to electricity through off-grid renewable energy solutions in 2022 (IRENA, 2022). This includes approximately 138 million people who use solar lamps (comprising a LED lamp, solar panels, battery, power controller of less than 11 W), 30 million who use residential solar systems (power exceeding 11 W), and at least 3.4 million connected to microgrids, as illustrated in Figure 2. It is noticeable that since 2019, there has been a decrease in the population served by renewable solutions. The total number of global populations served by renewable energy off-grid decreases 15.81% between 2019

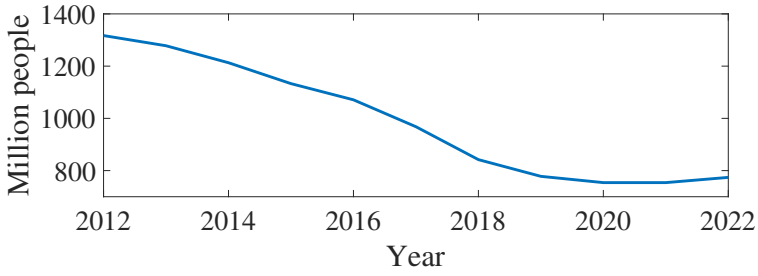

Figure 1 – People without access to electricity worldwide, 2012-2022 (IEA, 2022).

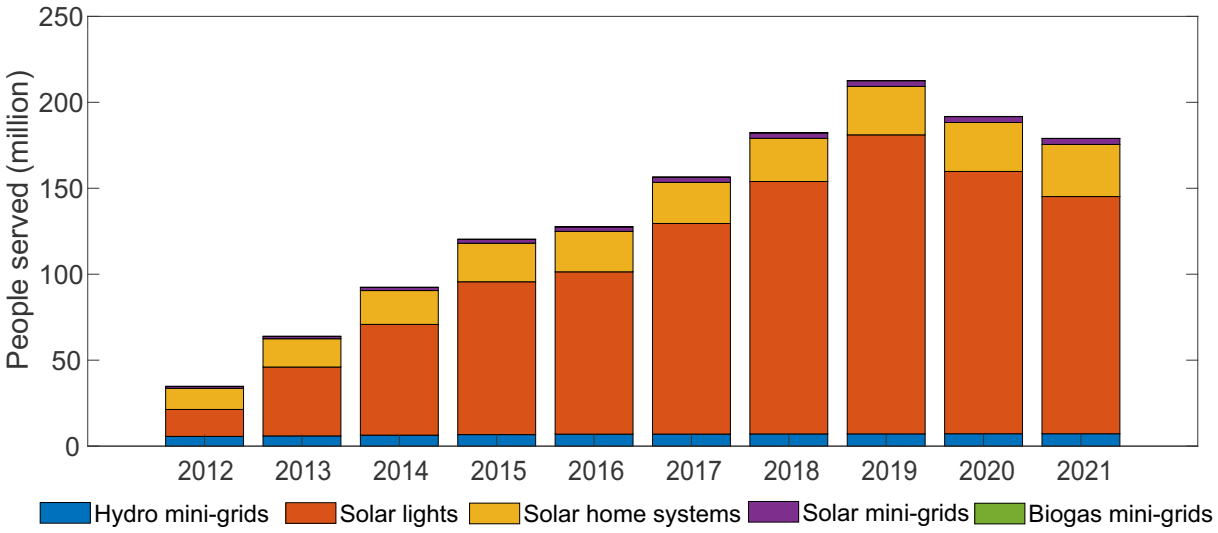

Figure 2 – The global population served by off-grid renewable energy solutions (IRENA, 2022).

and 2022. The most significant change is observed in the number of people using solar lamps, which has decreased by 20.67% since 2019, highlighting the energy crisis influenced by COVID-19.

In Brazil, about 2 million people live without access to electricity (IBGE, 2019). 990,113 Brazilians in the Legal Amazon region live without electricity. It is estimated that 19% of the population living on Indigenous land in the Amazon lacks access to electricity (IEMA, 2019). According to Trindade and Cordeiro (2019), in 2018 around 5% of the Amazonas State population in Brazil, distributed in 2261 communities and 41167 households, did not have access to electricity.

3.3 million people live in places where the electric system is isolated, not connected to the Sistema Interconectado Nacional (SIN) (National Interconnected Power System), ranging from 15 people in the Maici community, in the state of Rondônia, to 436,500 people in Boa Vista, the capital of Roraima (EPE, 2022). In isolated locations in Brazil, the energy supply is limited to a few hours a day, is very expensive, inefficient, and is the result of a mobilization of people who share the costs of fuel and maintenance and often install and operate their own electric grid.

Due to the continental dimensions of Brazil, some regions of the country operate with an isolated electrical system from the rest of the country. There are a total of 212 locations served by 8 distributors, as shown in Figure 3. These systems have a maximum demand between 2 kW and 243 MW, and the installed power at 53% of these locations is less than 1000 kW. Although modest, the numbers represent a high impact on public accounts, since the generation in isolated systems is subsidized through the Fuel Consumption Account program, and the budget forecast in 2018 for this program was R$ 6.2 billion. The high cost is due to the high share of diesel oil generation, which corresponds to 97%

generation in isolated systems in Brazil, so solutions that can reduce diesel consumption and generation cost are extremely important(EPE, 2019).

The Amazonas State represents 18% of the geographical area of the country, surrounded and flooded by the Amazon river basin, with few roads and extensive use of rivers as a means of transport to its rural area. Due to these characteristics, some programs such as *Luz Para Todos* (Light For All), which aims to provide access to electricity to all parts of Brazil, have had limited reach in the Amazonas State due to the difficulties in extending the grid to remote regions of the Amazon Rainforest (Gyamfi et al., 2020). Electric energy is important for the development of the Amazon State, enabling education in rural areas and providing access to modern means of communication. The arrival of electricity in itself does not provide immediate development, but can provide the introduction of technical and technological innovations, improving agricultural and production practices, and integrating these communities into what is most modern in these areas (Andrade, 2010). Note that after providing access to electricity, an increase in the power demand is expected because people may return or arrive at the electrified community. Thus, it is mandatory that the electrification be expandable.

The Northern region of Brazil shows a large number of non-electrified communities, with very different social, cultural, and geographic characteristics when compared to the rest of the country, and the universalization of energy must take into account that access to services must be implemented in an unprecedented way, different from the techniques

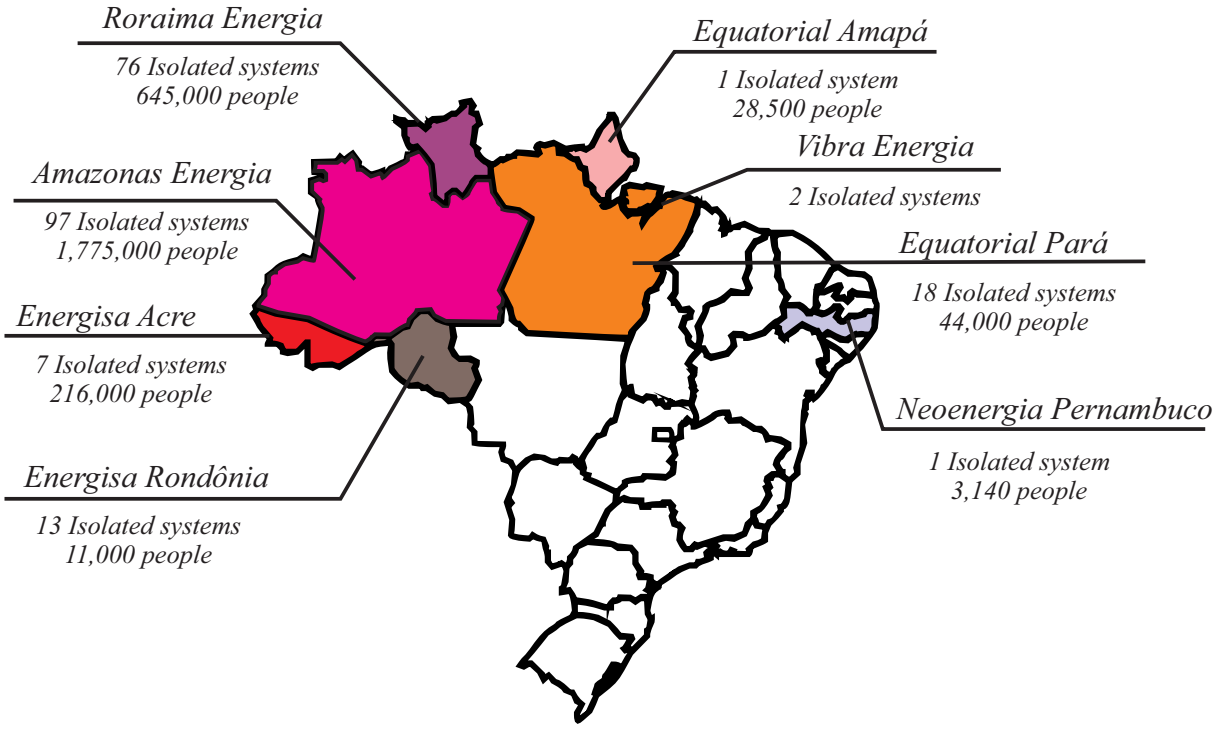

Figure 3 – Total number of isolated locations and the number of people served by isolated systems in each state (EPE, 2022).

of generation and distribution adopted in other Brazilian regions (Andrade, 2010).

This work aims to study the electrification of riverside communities with characteristics similar to the community of Mipindiaú in the Amazon, as shown in Figure 4. Mipindiaú comprises 43 houses, a school, and a health center, totaling 45 consumer units. The main challenges facing this community are intense rainfall, high temperatures, humidity and being isolated from the SIN. The diesel generator in this community has not been functional for four years, leaving the entire community without access to electricity (Alderton, 2020). The trip between Manaus and several of these communities depends on the size of the boat and the motor capacity, with 14 of them studied in Gyamfi et al. (2020). It takes two hours to travel from Manaus to Mipindiaú on a boat with a 150 HP motor.

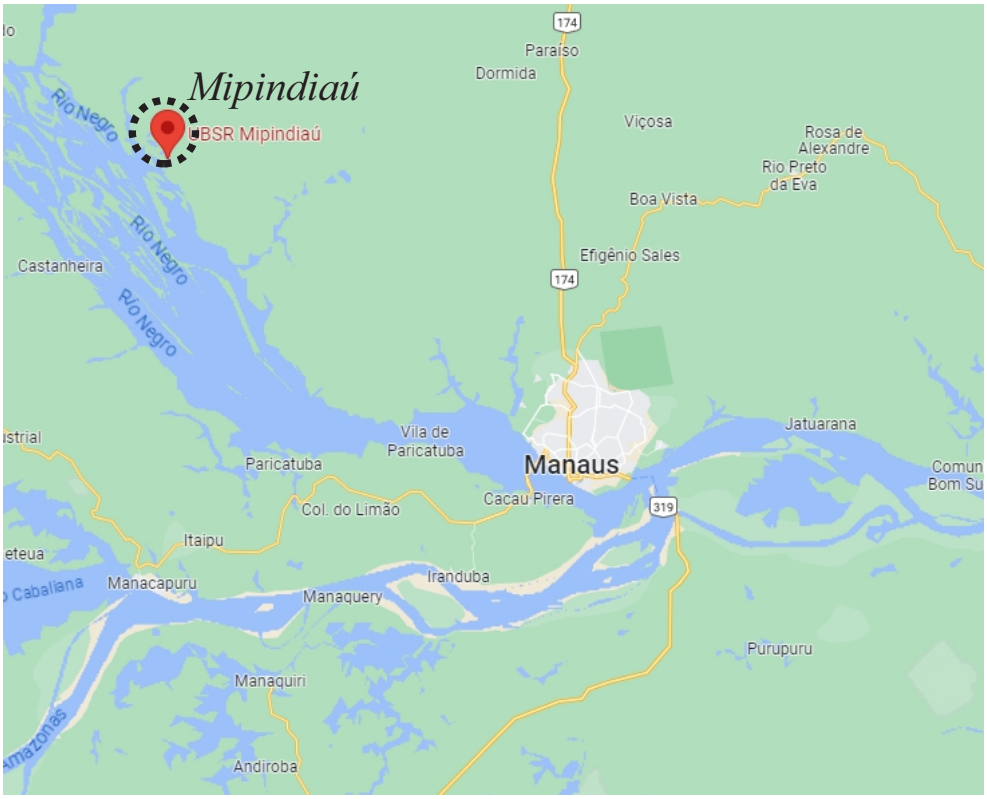

Figure 4 – Location of Mipindiaú.

Solar energy and biomass are two abundant resources in these communities. In Mipindiaú, the average annual global horizontal solar irradiation is 4.63 kWh/m^2/day. Solar irradiance levels remain relatively constant throughout the year, and atmospheric clarity levels do not change dramatically. The use of hybrid systems, which incorporate solar energy, batteries and biogas generation, may be the solution for communities like this to have access to electricity, which is essential for social development and crucial for the health and well-being of the riverside population in the state of Amazonas (Alderton, 2020).

Despite the abundance of rivers in the Amazon region, hydropower generation is

challenging in the area. In general, rivers have slow flow water and carry a significant amount of organic material, such as branches, leaves, and other debris. Economic and social impacts can also be a concern. Regarding downstream impacts on residents, they can lose their livelihoods based on fishing and agriculture in the floodplain. The health impacts of reservoirs include the proliferation of insects and the methylation of mercury (which transforms this metal into its toxic form). Vegetation loss can occur not only due to direct flooding, but also due to deforestation by displaced residents, as well as by immigrants and investors attracted to the area (including the construction of roads to dam sites) and agribusiness facilitated by the waterways associated with the dams. This makes hydropower generation unsuitable for the Amazon region (Fearnside, 2015). It is important to mention that most waterfalls in this region are too small to build large reservoir hydroelectric power plants. However, there are projects for small run-of-the-river hydroelectric power plants that have a much smaller environmental impact. Nevertheless, implementing a storage strategy with batteries would be necessary to synchronize the generation and demand curves.

1.2 Motivation and Relevance

Several configurations are proposed for AC power grids in the literature: three-phase with four wires and two voltage levels (Li; Vilathgamuwa; Loh, 2005), (Chilipi et al., 2017); three-phase with three wires with one voltage level (Kasal; Singh, 2011); single-phase or two-phase (Kanavaros; Oriti; Julian, 2020). Two configurations are feasible for two-phase grids: a two-wire system with two phases and three-wire with two phases and neutral (2Φ3W). An advantage of 2Φ3W system is to provide two different voltage levels (phase-to-neutral and phase-to-phase) to the loads. In real applications, the 2Φ3W grid is a common practice in some regions of South America, especially in Brazil, for rural areas using a single-phase transformer with tapped secondary and neutral (Kersting, 2008), and for isolated grids it can be found in some parts of Africa, Central America, Asia, and Europe (Henry, 2018).

Even in grid-connected installations, in practice, there are grid branches and consumer facilities supplied with two phases and a neutral conductor derived from four-wire three-phase grids. A simple 2Φ3W system is illustrated in Figure 5, which shows a three-phase four-wire electrical grid that supplies a load and a connected 2Φ3W converter. This is the case for residential and small commercial consumer installations, for example. In this context, the development of specific topologies and control schemes for 2Φ3W power converters can contribute to the introduction of smart grid features in small consumer facilities (Furtado; Barbosa, 2019).

Three-phase circuits are commonly used to supply high-power loads, whereas

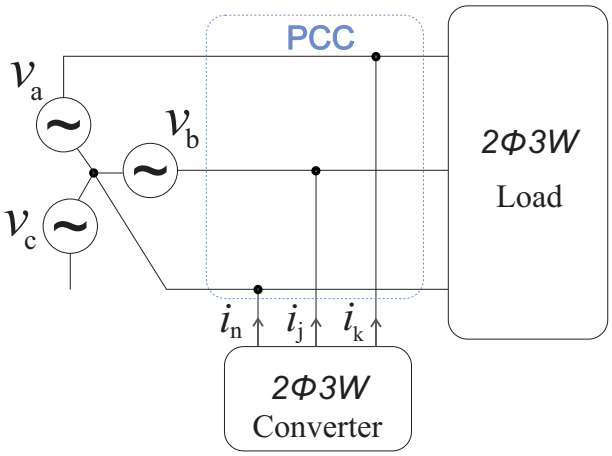

Figure 5 – 2Φ3W system connected to a three-phase four-wire grid. Adapted from (Furtado; Barbosa, 2019).

single-phase supplies are typically used for low-power applications. Furthermore, electricity distribution companies in several countries use 2Φ3W circuits to provide power to low-power electrical consumers, such as homes and small businesses.

Two-phase three-wire power supplies offer a straightforward and cost-effective solution that allows consumers to use two voltage levels to connect single-phase loads. It is common practice to supply regular wall sockets and lighting circuits using phase-neutral circuits. However, equipment with higher power ratings, such as electric showers and heaters, is generally connected in phase-to-phase circuits (Furtado, 2019). The key conditions for providing 2Φ3W power supplies, as specified by certain Brazilian utility companies, are described in Table 1.

Table 1 – Conditions of low-voltage 2Φ3W power supplying in Brazil. Adapted from Furtado (2019).

Utility Company	Voltage[1] (V)	Power (kVA)
AES Eletropaulo	127/220	≤20
	120/208	≤20
	115/230	>5
CEMIG	127/220	<15
	127/254	
COPEL	127/220	<14
CPFL Paulista	127/220	12-15
	220/380	15-25
Light	127/220	<8
Ampla	127/220	8-10
CELG-D	220/380	12.1-25

[1] Phase-to-neutral voltage/phase-to-phase voltage

Usually, 2Φ3W systems are implemented in *abc* coordinates, meaning that the phase voltages of the system are 120° apart from each other, considering the extension of the conventional three-phase electrical grid. However, in applications in remote areas,

such as riverside communities, a grid-forming converter is required to provide voltage and frequency references to the grid. Therefore, several power system topologies can be addressed in terms of voltage magnitude, frequency, and phase relationship in isolated systems.

From Table 1, it is observed that most utility companies provide two-phase systems for loads below 20 kW. Reference Gyamfi et al. (2020) indicates that 8 of the 14 communities shown in the study have loads below 15 kW. In this context, this work focuses on 2Φ3W converter applications with power below 15 kW.

Regardless of the electrical power system used, the reliability of power converters in an isolated AC power grid is a key issue. Depending on the geographical location of the system, maintenance costs become considerably high. Under such circumstances, the design of reliability and condition monitoring is a key concept to reduce maintenance and replacement costs in remote isolated grids (Song; Wang, 2013).

In this context, this work lies in the use of a wear-out prediction method to evaluate converters in two-phase three-wire systems, which can be used in isolated systems as in this dissertation, or even be valuable in expanding the adoption of distributed generation technologies by a large number of 2Φ3W consumers in countries like Brazil. The use of converters in 2Φ3W systems can contribute to the proper integration of distributed generation resources and functionalities in two-phase residential and commercial installations. These functionalities include photovoltaic systems, electric vehicles, active filters, smart meters, Uninterruptible Power Supplies (UPS), and others.

1.3 Objectives

1.3.1 Main objectives

The main objective of this dissertation is to propose the *xyn*-converter as a two-phase three-wire AC system for riverside communities. A wear-out prediction method is used to statistically calculate the lifetime consumption of 2Φ3W converters for three types of grid configuration, which differ in terms of displacement angle between voltage in phases: 90°, 120°, and 180° (referred to as $\alpha\beta n$-converter, *abn*-converter, and *xyn*-converter in this work, respectively).

1.3.2 Methodology

Most references focus on the characteristics of the power system rather than the converter itself. In fact, a noticeable gap in the literature lies in the discussion of the current stresses and wear-out experienced by 2Φ3W power converters. Hence, this dissertation aims to fulfill this gap with the following contributions:

- Propose analytical expressions for the semiconductor and DC-link current stress under realistic current unbalances between phases for 2Φ3W converters.
- Quantitatively compare the $\alpha\beta n$, *abn* and *xyn* converters in terms of lifetime prediction to evaluate the best performance indices.
- Propose the utilization of the *xyn*-converter immersed in oil to improve the thermal performance of the converter.

1.4 Contributions

The main contributions of this dissertation are highlighted according to each topic related to the developed objectives:

1. Equations that assess the current stress for 2Φ3W converters are proposed in Chapter 4. These equations help to understand the thermal stress in semiconductors and DC link capacitors and serve as a basis to demonstrate the superior performance of the *xyn*-converter compared to the other converters used in two-phase three-wire systems.
2. The experiments presented in this work are crucial, as they demonstrate the efficiency of the *xyn*-converter from the thermal stress perspective. It is possible to compare the results between two types of setups: one that employs a power semiconductor module and the other that utilizes discrete semiconductor devices.
3. This work proposes the utilization of an oil-immersed converter to enhance the thermal and dielectric characteristics of the converter. The oil-immersed converter has intriguing features that allow higher power and voltage levels to be applied to the converter within a smaller volume. Chapter 6 provides insights on the use of an oil-immersed converter and presents experimental results that demonstrate the benefits of employing the *xyn*-converter operating in an oil-immersed environment.

1.5 Organization of this Ph.D. dissertation

This Ph.D thesis is organized into seven chapters. Chapter 1 concerns the introduction of the thesis, with the context and relevance of the problem, motivations, and objectives to be addressed. Chapter 2 presents a literature review of isolated power grids, control of 2Φ3W converters, mission profile reliability analysis, and shows the gap filled by this dissertation. Chapter 3 presents the basics of 2Φ3Wcircuits, details the case study of this dissertation, and explains the prototypes developed for experimental results of thermal stress. In Chapter 4, analytical equations are proposed to evaluate current

stress under general load conditions. Chapter 5 shows the results of the simulations to evaluate the reliability of the converters studied in this dissertation and the results of the experiments to measure the thermal stress of the semiconductors of the 2Φ3W converters. Chapter 6 presents an empirical investigation to demonstrate the potential performance improvement achieved by immersing test prototypes in insulating fluids to improve heat dissipation. Chapter 7 states the conclusions obtained from this research and a proposal of future development works.

1.6 Publications

The results presented in this dissertation are a collection of research published in scientific journals and national and international conferences, as listed below:

1.6.1 Journal Papers

1. **J. H. De Oliveira**, A. F. Cupertino, E. M. S. Brito and D. I. Brandao, "Wear-out analysis of a grid-forming two-phase three-wire converter under unbalanced load," in IEEE Open Journal of Power Electronics, doi: 10.1109/OJPEL.2024.3379027.

2. **J.H. de Oliveira**, R.C. de Barros, A.F. Cupertino, H.A. Pereira, D.I. Brandao, Analysis of component current stresses of grid-forming converters for two-phase three-wire isolated AC power grids, Microelectronics Reliability, Volume 149, 2023, 115226, ISSN 0026-2714, https://doi.org/10.1016/j.microrel.2023.115226.

3. A. M. S. Alonso, **J. H. Oliveira**, D. I. Brandao, J. P. Bonaldo, H. K. M. Paredes, F. P. Marafao, Cpt-based control strategy for a two-phase three-wire pv inverter: A multifunctional perspective and a comprehensive review, Brazilian Journal of Power Electronics (2022), https://doi.org/10.18618/REP.2022.2.0052.

1.6.2 Conference Papers

1. **J. H. de Oliveira**, R. de Barros, A. F. Cupertino, H. A. Pereira, D. I. Brandao, Wear-out prediction of grid-following converters for two-phase three-wire isolated ac power grids, in: 2021 IEEE Green Technologies Conference (GreenTech), 2021, pp. 372–379, doi: 10.1109/GreenTech48523.2021.00065.

2. **J. H. de Oliveira**, Jamie E. Turnbull, Giri Venkataramanan, Daniel Ludois, Experimental Evaluation of Thermal Performance of Oil-immersed Power Converter, in: COBEP-SPEC 2023 Conference, 2023, doi: 10.1109/SPEC56436.2023.10407651.

1.6.3 Participation in other work

1. G. Reis, D. I. Brandao, **J. H. Oliveira**, L. S. Araujo, and B. J. Cardoso Filho, "Case Study of Single-Controllable Microgrid: A Practical Implementation," Energies, vol. 15, no. 17:6400, 2022, https://doi.org/10.3390/en15176400.

2 Literature Review

This chapter examines different aspects of isolated power systems, including their setups, technologies used, control methods, and converter implementation in 2Φ3W systems. The section concludes with a discussion of the current reliability status in the 2Φ3W converters.

2.1 Isolated power grid systems

Solutions to supply electricity in isolated locations are usually classified according to the type and number of generation sources in addition to the energy demand (Aberilla et al., 2020). Historically, these isolated systems have been composed of diesel generators. Recently, with increased environmental awareness and greater concerns about energy security, states and other stakeholders have shown an increasing interest in alternative energy sources for isolated power systems and rural electrification (IRENA, 2018). Thus, hybrid electric power generation systems are being increasingly used. Renewable energies such as photovoltaic (PV), biogas, and others, diesel generation, and batery energy storage systems (BESS), including lead-acid and lithium, are typical elements of isolated power systems in remote communities.

Different configurations of hybrid systems considered for household installations and community microgrids are shown in Figure 6. Figure 6(a) shows an AC system with diesel/biogas generation, PV generation, battery bank and loads. This system has more than one converter. In systems with dispatchable energy, converters can be of two types: grid-forming or grid-following converters. In the literature, these architectures are widely discussed under the name of microgrids, which can be connected to a main grid or not. In this study, only isolated microgrids are discussed.

As shown in Figure 6(a), distributed energy resource units are classified into two groups according to their connection to a microgrid. The initial group comprises traditional or rotary units connected to the microgrid through rotating machinery. In contrast, the second group comprises electronically linked units that use electronic power converters to establish a connection to the host system (Katiraei et al., 2008).

Depending on the type of power delivery, microgrid configurations are categorized into DC, AC, hybrid and 3-NET topologies. AC microgrid systems operate similarly to traditional AC power systems, incorporating frequency, voltage levels, and protection mechanisms. The rise of power electronics technology has led to the recent implementation of DC microgrids due to increased DC loads and the availability of power converters for DC

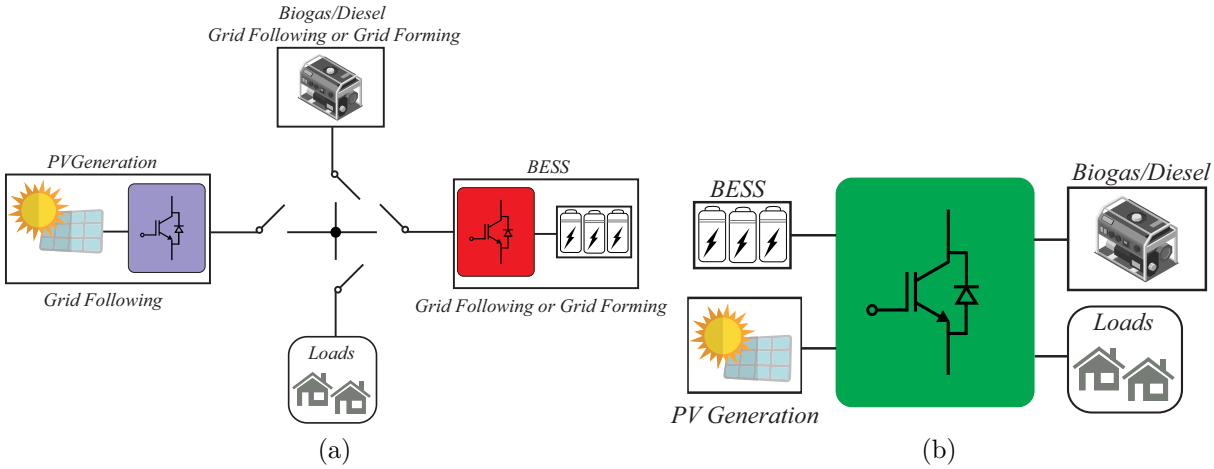

Figure 6 – Isolated AC grids: (a) Distributed converters. (b) Central converter

voltage transformation across various levels and applications. Hybrid microgrids are capable of supplying both AC and DC loads within the same system, using different converters to interface between power sources and loads (Cabana-Jiménez; Candelo-Becerra; Sousa Santos, 2022)(Gupta; Doolla; Chatterjee, 2018)(Lotfi; Khodaei, 2017).

The 3-NET microgrid topology integrates three different types of grids: a high-quality DC grid, a low-quality DC grid, and an AC network. This setup enables the supply of energy within a single microgrid to components with varying levels of sensitivity to changes in power quality parameters (Cabana-Jiménez; Candelo-Becerra; Sousa Santos, 2022).

In off-grid systems, it is common to implement load or generation shedding to maintain power balance and subsequently stabilize the voltage or angle of the microgrid. Consequently, the operational strategy must prioritize providing service to critical loads within the microgrid. Additionally, microgrid operation should include functionalities such as customer service distinction, improving power quality for specific loads, and improving the reliability of predefined load categories. Load control can also be used to optimize distributed storage unit ratings and distributed generation units by mitigating peak loads and managing a wide range of load fluctuations (Katiraei et al., 2008).

The specifications of power converters depend on the type of microgrid (AC or DC) and other characteristics of the device such as voltage levels, power flow direction, etc. In addition, they may incorporate a transformer for galvanic isolation purposes. Due to the limited prevalence of DC grids, there are no standardized power converter topologies for connecting distributed energy resources to them yet. Generally, power converters in DC systems require fewer components compared to those in three-phase AC systems. Certain DC topologies can utilize high-frequency transformers, resulting in smaller and lighter transformers compared to the low-frequency ones used in AC microgrids (Planas et al., 2015).

Hybrid converters are found on the market today. Figure 6(b) shows that all generation sources and loads are connected to a single converter. In Brazil, it is possible to find some commercial brands. Figure 7 shows some examples of converters found. *Growatt* and *Phocos* hybrid converters allow synchronism control, grid disconnection, and power management and can be used in isolated locations. The *SMA* converter presents a difference compared to the two previously mentioned brands and does not allow direct connection of photovoltaic modules, which requires a photovoltaic inverter. These models are single-phase, but can be used in configurations that allow the creation of a three-phase system using at least three converters, one emulating each phase of the system separately in a master and follower architecture.

Figure 7 – Examples of hybrid converters.

2.2 Converter control in 2Φ3W systems

The design of control systems for inverter-based microgrids is crucial to shaping the dynamic behavior of the system. Inverter-based microgrids can operate in grid-connected mode or islanded mode. The control architectures of these systems typically employ droop-based control, where active power is connected to frequency control, and reactive power is linked to voltage control (Fani et al., 2022). Table 2 outlines the microgrid control methods and parameters for both operating modes.

Table 2 – Control methods for inverter-based microgrids. Adapted from Fani et al. (2022).

Operation Mode	The parameters must be controlled		Control method
	Active and reactive power	Voltage and frequency	
Grid-connected mode	Yes	No	Constant current control PQ control
Islanded mode	Yes	Yes	P-f control Q-V control

DC microgrids offer the advantage of not requiring frequency or reactive power control. This simplifies control tasks because devices can be connected directly to the microgrid without the need for synchronization processes (Fani et al., 2022). Voltage

balancing in three-phase AC microgrids can be achieved through several methods. This includes implementing special control loops for converter-based distributed generators and static sources, using reactive support devices like Static Var Compensators (SVC) or Static Synchronous Compensators (D-STATCOM) with suitable control algorithms and employing straightforward switched capacitors (Lidula; Rajapakse, 2014).

Droop control is the preferred option for controllable distributed generators, such as gas turbines and small diesel generators, where the primary energy is adjustable. This control method is highly reliable and operates without the need for communication between distributed energy resources (Planas et al., 2015)(Lopes; Moreira; Madureira, 2006). On the other hand, for non-controllable distributed generators such as wind turbines and PV systems, which have non-adjustable primary energy, nonlinear droop control or hybrid droop control combined with Maximum Power Point Tracking (MPPT) can be employed (Schonbergerschonberger; Duke; Round, 2006)(J.Bryan; Duke; Round, 2004).

Some references in the literature investigate the control of 2Φ3W power converters. The authors of Viola et al. (2018) present the results of an active power filter to compensate harmonics and inject reactive power into the 2Φ3W grid. The development of a small signal model and the control of a 2Φ3W active filter is shown in Rodrigues et al. (2017). Reference Alonso et al. (2022) shows a flexible control strategy based on Conservative Power Theory capable of adequately synthesizing control references for a PV-based multifunctional inverter operating in a 2Φ3W grid. All of these works use a displacement angle of 120° between the line voltages. The main advantage of this grid configuration is the direct connection to the distribution system, which is usually set as a three-phase system. In this dissertation, this 2Φ3W grid configuration is called *abn*-system.

The authors of Furtado and Barbosa (2019) show the modeling of 2Φ3W inverters connected to the grid considering predictive control techniques integrated with space vector modulation to obtain fixed switching frequency and exemplary performance in tracking sinusoidal and non-sinusoidal current references. Control is performed in reference $\alpha\beta$ in this work.

Several works are dedicated to applying 2Φ3W converters as active power filter (APF). In Furtado, Rodrigues and Barbosa (2015), an adaptation of the Instantaneous Power Theory (p-q theory) is proposed for 2Φ3W systems to identify power components and to generate reference signals for a three-arm APF, seeking to mitigate reactive components, harmonics, and load imbalances. Alternative methods also formulated through the p-q theory focus on the control of 2Φ3W converters driven as two independent single-phase APF (Furtado et al., 2014) or with the overlap of two simultaneous operation modes to further mitigate neutral currents (Furtado; Barbosa; Rodrigues, 2015). The authors of Fajardo et al. (2015) propose active power conditioning in 2Φ3W circuits based on the exchange of powers between existing phases, using the DC link of multilevel converters.

Another configuration of the 2Φ3W grid considers the lines displaced by 180° instead of 120°. It is common in rural areas, and the voltages are obtained based on center-tapped transformers (Kersting, 2008). The neutral current is zero under balanced conditions since it is the 2Φ3W system according to Fortescue's Theorem (Fortescue, 1918). It is referred to herein as *xyn*-system.

Finally, the authors of Alibeik, dos Santos Jr. and Blaabjerg (2014) and dos Santos Jr. and Alibeik (2015) have proposed the quadrature voltages for the 2Φ3W electrical system (i.e., displaced by 90°). In this grid configuration, the instantaneous power is constant, which reduces the inherent DC-link voltage oscillation. It is called $\alpha\beta n$-system.

Railway traction systems also take advantage of the 2Φ3W topology. In Kaleybar et al. (2017), a 2Φ3W quasi-Z compensator is used to improve power quality in AC railway networks, mainly used for harmonic current mitigation, negative sequence compensation, and power factor correction. Another converter topology, composed of two step-down transformers and based on the 2Φ3W configuration, is proposed by Wu et al. (2012) to eliminate negative sequence components in railway traction systems.

The review shows that the works found in the literature focus on grid-following converters. Thus, there is a gap to be filled in the grid-forming converters in 2Φ3W systems.

2.3 Reliability

Failures in systems can stem from a variety of factors, encompassing: inherent inadequacy within the project leading to product weakness; overload, wherein excessive stress surpasses a product's capability, inducing failure; the gradual erosion of robustness over time due to wear, transforming an initially sturdy item into a fragile one; errors in product specifications and improper maintenance practices. Furthermore, failures can also be the result of additional time-dependent elements, including battery deterioration and structural distortion triggered by fluctuations in temperature or tensile stress (O'Connor; Kleyner, 2012)(Rocha, 2014).

Reliability predominantly addresses failures within time domains, establishing a fundamental divergence between conventional quality control and the discipline of reliability engineering. Conventional quality control aligns with the inspectors concept, wherein a product is evaluated against specified criteria or a collection of attributes, and once deemed compliant, it is dispatched to the consumer. However, reliability lies within the realm of engineering uncertainty. The question of whether an entity will function for a specific duration is solved through a probabilistic framework (O'Connor; Kleyner, 2012). This culminates in the standard engineering delineation of reliability as:

- *The ability of an item to perform a required function under stated conditions for a*

> *certain period of time, which is often measured by probability of failure, by frequency of failure, or in terms of availability* (IEEE, 2009).

According to this definition, reliability assumes the form of a probability quantified within the bounds of 0 and 1. Characterizing failure requires a precise delineation within the context of the system under examination. Frequently, an item need not be entirely non-functional to be deemed defective. A device undergoing reliability assessment must perform a designated function under specified conditions that must be respected. Ultimately, every item must demonstrate accurate operation throughout a designated time frame (O'Connor; Kleyner, 2012)(Ushakov, 2012).

Distinguishing between repairable and non-repairable items is essential when dealing with reliability predictions or measurements. For non-repairable things like transistors, reliability refers to how likely they are to work throughout their expected lifespan, whether it is the entire duration or a specific period where only one failure can occur. While they are in use, the chance of experiencing the first and only failure is known as the hazard rate. Other reliability aspects include the mean life or mean time to failure (MTTF) or the time when a certain percentage might fail (such as 10% or B_{10}, known as percentile life). For repairable items, reliability is about the probability that they do not fail at a specific time, even if more than one failure could occur. This can also be thought of as the rate at which failures occur, sometimes called the failure rate (O'Connor; Kleyner, 2012).

This dissertation focuses on non-reparable items. Such items exhibit a distinctive pattern of failures over time, famously represented by the 'bathtub curve' illustrated in Figure 8. There are three fundamental ways in which the failure pattern can evolve. The hazard rate may decrease, increase, or remain constant. Decreasing hazard rates are observed in items that become less prone to failure as their operational lifespan extends. This is often seen in electronic equipment and components. This segment of the curve is termed 'infant mortality', characterized by an initially high but decreasing failure rate. Initial failures are due to inherent defects, design errors, faulty components, improper manufacturing processes, and inexperienced labor, among other factors. The failure rate decreases over time as defect rectifications eliminate the most fragile elements or as design or installation errors are identified and addressed (O'Connor; Kleyner, 2012)(Rocha, 2014).

During useful life, failures outside the system occur due to random causes, such as accidents, excessive energy releases, misuse, or improper operation. In this period, the best maintenance strategy is predictive: monitoring to detect the beginning of the wear-out phase (Rocha, 2014).

Wear-out failure modes exhibit an increasing hazard rate. For instance, material fatigue caused by weakening due to repetitive loading represents a failure mode that does not manifest itself within a finite time, but instead displays an increasing likelihood of

occurrence. In the senile mortality phase, the final stage of the item lifetime begins as the failure rate increases. This phase is marked by component wear, corrosion, fatigue, mechanical, electrical, or chemical deterioration, inadequate maintenance, and related factors. In this stage, the most effective maintenance strategy is preventive. This involves taking advantage of the imminent failure of the equipment to replace or renovate the item strategically (O'Connor; Kleyner, 2012)(Rocha, 2014).

The landscape of reliability research in power electronics is transforming significantly, transcending conventional statistical methods, and gravitating toward physics-grounded approaches. This evolution aims to offer improved insight into the origins of failures and design flaws, prioritizing the identification of remedies to enhance reliability rather than focusing solely on numerical analysis. At the forefront of reliability research in power electronics lies the physics of failure (PoF) approach, which focuses on dissecting the fundamental triggers of failure mechanisms (Wang; Ma; Blaabjerg, 2012)(Pecht; Dasgupta, 1995)(Ferreira, 2016).

Reliability predictions are based on understanding how systems might fail due to stress and damage. This involves understanding the causes of failures, their potential locations, and the conditions that contribute to them. The approach involves analyzing the system design, materials and operational aspects, such as its electrical connections and the surrounding environment. However, the effectiveness of this method depends on the precision and availability of models used to estimate the system time-to-failure, with ongoing research working to enhance these models (IEEE, 2003).

To make these predictions, representative models of the system are constructed to simulate its behavior under various conditions. These models help predict the likelihood of failure at specific points based on stress data obtained from simulations. The precision of these predictions is influenced by the quality of the models and the input data. This technique helps identify vulnerable areas within the system, establish safety margins,

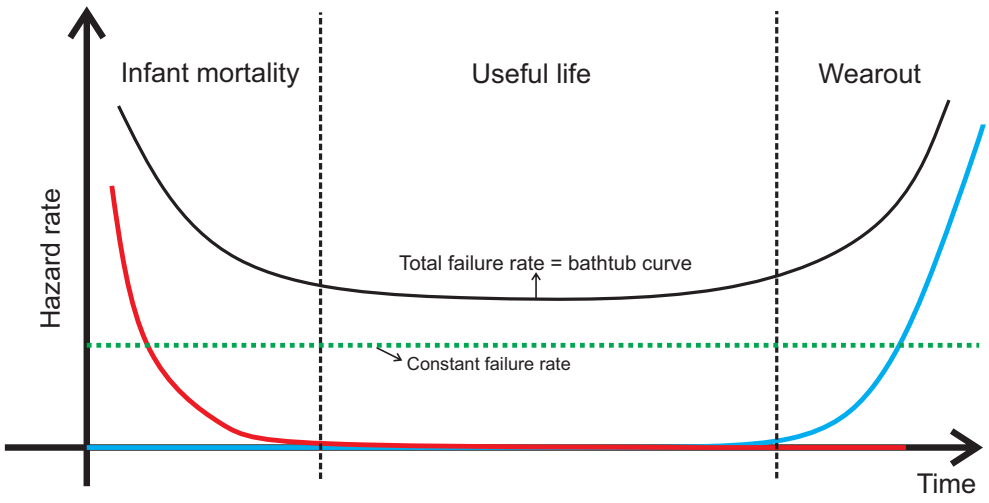

Figure 8 – The 'bathtub' curve.

design testing procedures, and establish connections between controlled laboratory tests and real-world usage scenarios. Although this methodology is valuable, it is recommended to complement it with empirical testing to validate its alignment with actual failure occurrences (IEEE, 2003).

Recent surveys indicate that semiconductors and capacitors are the devices most prone to failure in power converters used in industry (Falck et al., 2018),(Wang et al., 2014). Figure 9(a) shows that 38% of power converter failures occur in semiconductor and solder modules. The most significant sources of stress that affect the reliability of components come from thermal cycling, which is the variation of temperature inside or outside devices, accounting for 55% of failure causes, as shown in Figure 9(b).

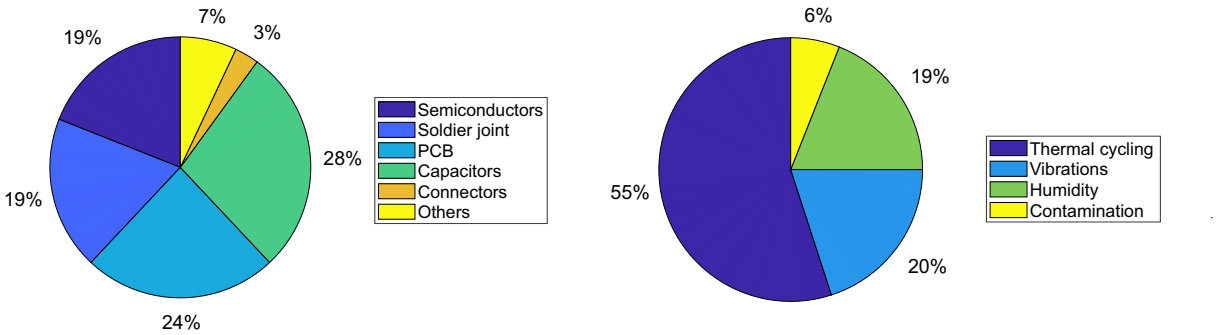

Figure 9 – (a) Frequency of occurrence of fault elements in converters. (b) Stress sources of the faults in converters (Choi; Blaabjerg; Lee, 2015).

IGBT power modules are commonly classified into two primary types: module packaging and press-pack packaging. Modules exhibit elevated thermal resistance, reduced power density, and increased likelihood of failures attributed to solder joints and bond-wire within the assembly. On the contrary, encapsulation techniques that employ pressure connections eliminate the need for bond wires, improving the reliability, power density, and cooling efficiency of the module (Ma; Blaabjerg, 2012a)(Ferreira, 2016).

Due to the direct relationship with reliability, there are three concerns when it comes to the thermal stress of semiconductor components: temperature cycling (ΔT_j), heating time (t_{on}) and average junction temperature (T_{jm}). The internal structure of an IGBT module is composed of several layers of different materials, as shown in Figure 10. $Z_{th(jc)}$ refers to the transient thermal impedance between the junction of the IGBT chip and the case module,$Z_{th(ch)}$ refers to the thermal impedance between the case and the heatsink, and $Z_{th(ha)}$ is the transient thermal impedance between the heatsink and the environment. The primary failure mechanism of IGBT modules is associated with thermal fatigue of the solder alloy layers. There are three main ways IGBTs fail due to thermal cycling stress: bond wire debonding, cracked solder joints under the chip (diode and IGBT), and cracked solder joints under the direct copper-bonded (DCB) (Reigosa,

2014),(Ciappa, 2002).

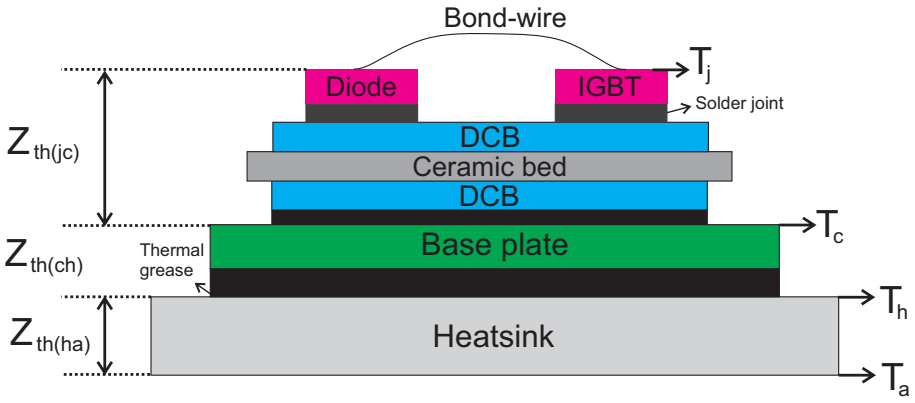

Figure 10 – Structure of IGBT module(Callegari et al., 2019).

2.3.1 Reliability and 2Φ3W systems

Steady-state temperature and thermal cycling are the main stress factors originating from current stresses, which must be considered in the overall reliability assessment (Song; Wang, 2013). The wear-out is typically used to quantify lifetime consumption and is based on a well-validated methodology in literature (Sangwongwanich et al., 2018a)-(Yang; Sangwongwanich; Blaabjerg, 2016). Reference Kshatri et al. (2022) shows a very reliable PV inverter with a hybrid Si/SiC power module, consisting of a Si-IGBT with a SiC anti-parallel diode. In Bakeer, Chub and Shen (2022), the authors investigated the reliability of an isolated buck-boost dc-dc converter (IBBC) based on the configuration of a series resonant converter (SRC). The reference Peyghami et al. (2019) explores the reliability performance of different converters operating in a power system and indicates converters prone to failure from the point of view of wear-out, analyzing the unreliability of IGBTs, diodes, and capacitors in a DC microgrid. Reference Brito et al. (2022) evaluates the reliability at the system level of a single-phase, two-stage PV inverter performing reactive power compensation. The analysis is carried out using three different mission profiles (Aalborg, Goiânia, and Izaña). In Sangwongwanich and Blaabjerg (2022), a method is proposed to evaluate the reliability of fault-tolerant power converters, considering wear-out failure. These papers use mission-based profile reliability analysis.

Some papers analyze the impact of mission profile used to calculate lifetime consumption. Reference Sangwongwanich et al. (2018b) investigates the impacts of mission profile resolutions on the reliability of PV inverters. Reference Silva et al. (2022) proposes a correction strategy to reduce errors in the lifetime consumption estimations of a single-phase grid-connected photovoltaic inverter due to decreasing mission profile resolution. The authors of Cupertino et al. (2019) evaluate how the length of the mission profile affects the reliability at the system level of a 5.5 kW PV inverter. Reference Sintamarean et al. (2014)

introduces a reliability-oriented design tool to study the impact of the mission profile on the reliability of SiC-based PV inverter devices.

Since the thermal loading directly affects the lifetime of power converters, the phase displacement angle plays an important role. The authors of Alonso et al. (2019), Silva et al. (2019) have compared the systems *abn*, $\alpha\beta n$ and *xyn* for active power oscillation and neutral current magnitude. Most references focus on the characteristics of the power system rather than the converter itself. In fact, a discussion of the effect of different line voltage displacements on current stresses and wear-out of power converters is a gap in the current literature. In addition, the impact of current high-frequency components on the capacitor current stress and therefore on the wear-out analysis has not been previously reported in the literature. Table 3 presents a comparison of several papers in the literature, evaluating the type of grid configuration, the type of result in the paper (simulations, hardware-in-the-loop, experimental results), if there is any analytical analysis of semiconductors or dc-capacitor current stress, and if there is any reliability evaluation method. The proposed work addresses an existing gap in 2Φ3W systems, as they currently lack a more detailed analysis of reliability studies for the converters.

2.4 Chapter closure

This chapter provided a literature review on the main topics addressed in this dissertation. Isolated power systems were characterized and important reliability concepts, particularly related to the physics of failure, were presented.

Semiconductors and capacitors are the devices most prone to failure in power converters. Most of these failures are caused by thermal stress. The study on reliability in 2Φ 3W converters remains a gap in the literature. The next chapters will provide more details on 2Φ3W converters, presenting equations to analyze the current stress of semiconductors and capacitors, which help to understand the reliability results of 2Φ3W converters.

Table 3 – Comparison of correlate papers in literature: grid configuration, result types, analytical current stress and reliability method.

Reference	Grid configuration	Isolated system	Results	Analytical current stress	Reliability
(Kshatri et al., 2022)	Single-phase	No	Simulations	No	*Mission-profile based*
(Bakeer; Chub; Shen, 2022)	dc grid	No	Simulations, Experiment	No	*Mission-profile based*
(Peyghami et al., 2019)	dc grid	No	Simulations	No	*Mission-profile based*
(Brito et al., 2022)	Single-phase	No	Simulations	No	*Mission-profile based*
(Sangwongwanich; Blaabjerg, 2022)	Three-phase	No	Simulations, Experiment	No	*Mission-profile based*
(Alonso et al., 2022)	*abn* 2Φ3W	No	HIL	No	No
(Viola et al., 2018)	*abn* 2Φ3W	No	Simulations	No	No
(dos Santos Jr.; Alibeik, 2015)	$\alpha\beta n$ 2Φ3W	No	Simulations	No	No
(Fajardo et al., 2015)	*abn* 2Φ3W	No	Simulations	No	No
(Furtado; Barbosa, 2019)	*abn* 2Φ3W	No	Simulations	No	No
(Furtado; Barbosa; Rodrigues, 2015)	*abn* 2Φ3W	No	Simulations	No	No
(Silva et al., 2019)	*abn* 2Φ3W	No	Simulations	No	No
This dissertation	**$\alpha\beta$*n*, *abn* and *xyn* 2Φ3W**	**Yes**	**Simulations, HIL Experiment**	**Yes**	***Mission-profile based***

3 Two-phase Three-wire power grids

3.1 Basics of Two-phase Three-wire circuits

Figure 11 illustrates the isolated two-phase three-wire system studied in this work, composed of a grid-forming converter, a set of grid-following inverters, and loads. The grid-forming converter consists of a full-bridge converter with an LC filter at the output. A BESS is connected to the DC-link of the converter, which has capacitance C. The photovoltaic system (a set of small solar plants) injects active power into the AC grid. The power processed by the grid-forming converter is the difference between the generated PV power and the load profile in the AC system.

All results in this thesis consider the BESS as a voltage source with a small internal resistance. Voltage fluctuations in the DC bus would directly impact the BESS lifetime. Moreover, a DC-DC converter might need to be employed for DC bus voltage control, which would introduce additional components in the converter's lifespan analysis. In this thesis, the analysis focuses on the grid-forming converter; therefore, at this stage of the work, a simplification of the BESS model is chosen.

In 2Φ3W systems, phase-to-neutral voltages are defined by:

$$v_j = V_j \sin(\omega t), \tag{3.1}$$

$$v_k = V_k \sin(\omega t + \theta), \tag{3.2}$$

where $V_{j,k}$ is the amplitude, ω is the angular frequency and θ is the angle displacement between phases. In this dissertation, the subscripts j and k refer to the phases of the

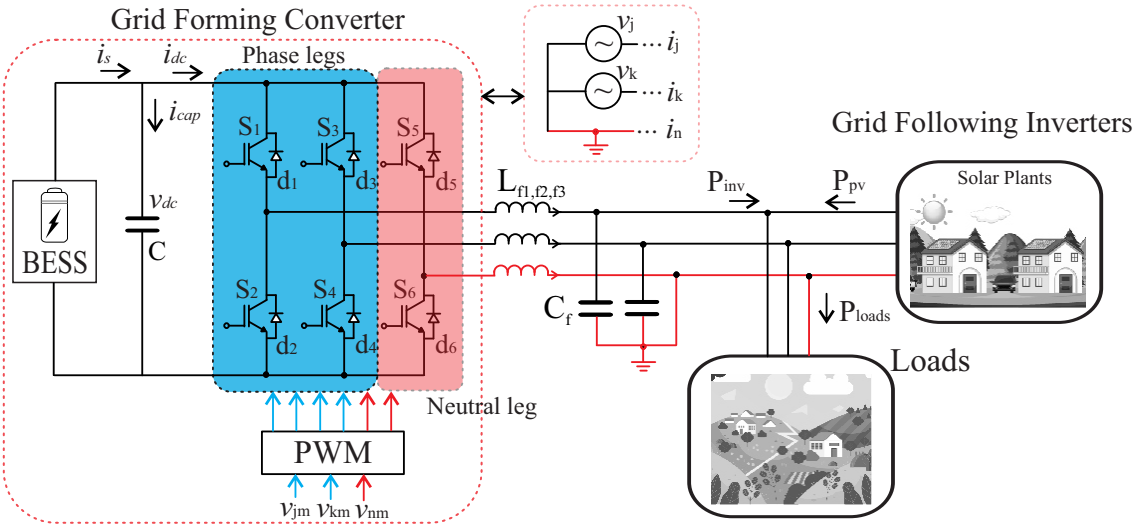

Figure 11 – Structure of a grid-forming converter for 2Φ3W isolated ac power grid.

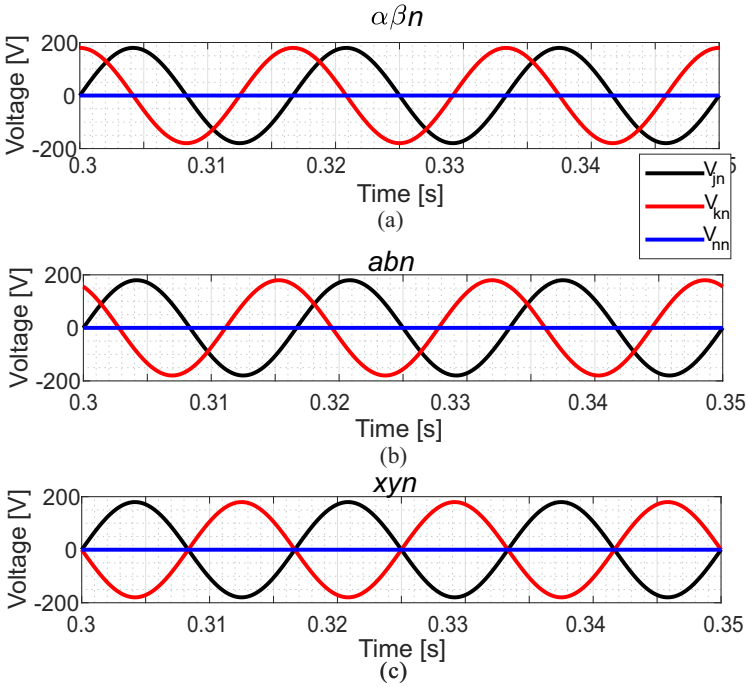

Figure 12 – Phase-to-neutral voltages of the 2Φ3W: (a) $\alpha\beta n$-system. (b) abn-system. (c) xyn-system.

grid, and n to the neutral. Figure 12 shows the phase-to-neutral voltages in $\alpha\beta n$, abn and xyn-systems obtained through simulation in the PLECS environment simulations. The currents are defined by:

$$i_j = I_j \cos(\omega t + \phi_j), \tag{3.3}$$

$$i_k = I_k \cos(\omega t + \theta + \phi_k), \tag{3.4}$$

$$i_n = -i_j - i_k, \tag{3.5}$$

where $I_{j,k}$ is the amplitude and $\phi_{j,k}$ is the angle displacement between voltage and current in each phase. The neutral current for each system under balanced conditions is (Silva et al., 2019):

$$i_{n,\alpha\beta n} = \sqrt{2} I \cos\left(\omega t + \phi - \frac{\pi}{4}\right), \tag{3.6}$$

$$i_{n,abn} = I \cos\left(\omega t + \phi + \frac{\pi}{3}\right), \tag{3.7}$$

$$i_{n,xyn} = 0. \tag{3.8}$$

where I is the peak amplitude of the line currents.

Note that the neutral current is zero for the xyn-system. On the other hand, $\alpha\beta n$-system shows the highest value among the three configurations. Figure 13 shows the phase currents in $\alpha\beta n$, abn and xyn-systems with the grid-following converter injecting balanced active power into the grid.

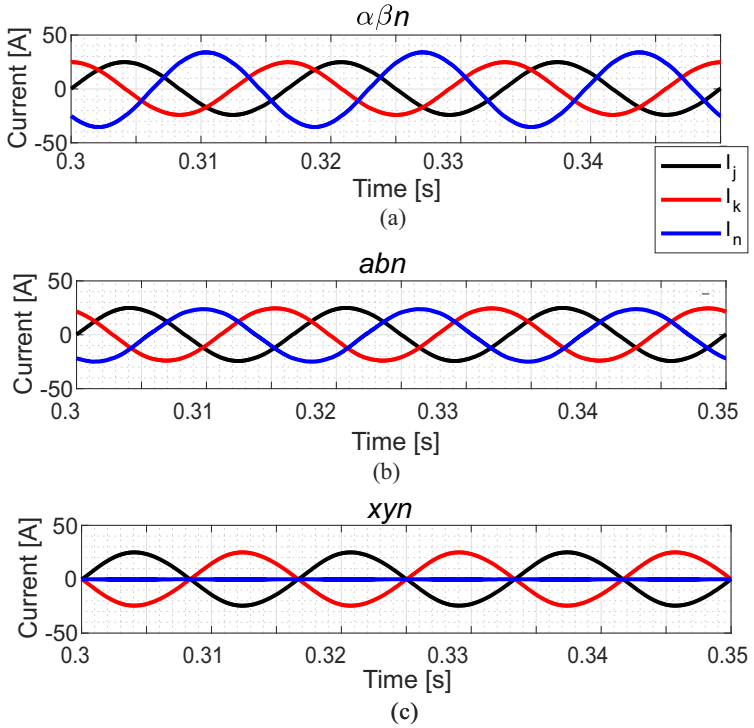

Figure 13 – Phase current of the 2Φ3W: (a) $\alpha\beta n$-system.(b) abn-system. (c) xyn-system. *Remark*: These results were obtained based on the parameters of Table 4 and rated power injection.

The instantaneous power is given by:

$$p = v_j i_j + v_k i_k. \tag{3.9}$$

Using (3.1)-(3.4), considering balanced load conditions the instantaneous power for each system are:

$$p_{\alpha\beta n} = V_{LN} I \cos(\phi), \tag{3.10}$$

$$p_{abn} = V_{LN} I \cos(\phi) + \frac{V_{LN} I}{2} \cos(2\omega t + \phi - \frac{\pi}{3}), \tag{3.11}$$

$$p_{xyn} = V_{LN} I \cos(\phi) + V_{LN} I \cos(2\omega t + \phi). \tag{3.12}$$

where V_{LN} is the line-to-neutral peak voltage, and ϕ the displacement angle between voltage and current in each phase.

As expected, a second-harmonic oscillation is presented in the abn-system. The xyn-system shows double power oscillation compared to the abn-system. Finally, the instantaneous power in the $\alpha\beta n$-system is essentially constant. The instantaneous power in $\alpha\beta n$,abn and xyn-systems, considering the grid-following converter injecting balanced active power, is shown in Figure 14(a).

Regarding the power semiconductor devices, xyn-system leads to the lowest thermal stress in the neutral leg components. This also leads to some temperature reduction in

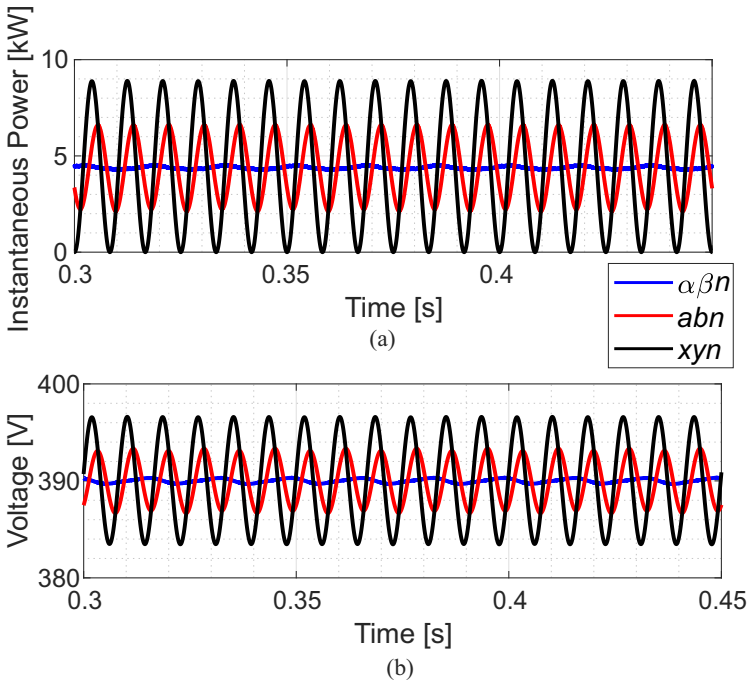

Figure 14 – (a) Instantaneous power in $\alpha\beta n$, *abn*, *xyn*-systems. (b) Voltage in DC-link capacitor in $\alpha\beta n$, *abn*, *xyn*-systems. *Remark*: These results were obtained based on the parameters of Table 4 and rated power injection.

phase legs, since typical designs consider the same heatsink for the whole inverter. The opposite is expected for the $\alpha\beta n$-system, due to the higher neutral current.

From the DC-link capacitor perspective, the absence of instantaneous power oscillation in the $\alpha\beta n$-system seems to be an advantage. First, for the same voltage ripple requirement, the DC-link capacitance can be reduced. Second, for the same DC-link capacitance, the second harmonic current is lower in $\alpha\beta n$ and *abn* systems than in *xyn*-system and the thermal stress seems to be lower. The voltage in DC-link capacitor is shown in Figure 14(b). The voltage oscillation observed in the $\alpha\beta n$-system is due to the high-frequency switching of the semiconductors and a slight load unbalance.

On the other hand, when analyzing the current in the capacitor, shown in Figure 15, it is noticed that by the root mean square (RMS) value, the current in the $\alpha\beta n$ (12.24 A) is higher than the *abn*-system (10.84 A) and *xyn*-system (10.45 A) even without low-frequency oscillation. As expected, the losses in the capacitor depend on the low and high-frequency components in the current in addition to the DC-link voltage oscillation.

Reference Alibeik, dos Santos Jr. and Blaabjerg (2014) states that there are no low-frequency components in the DC-link capacitors in the $\alpha\beta n$-system which benefits its design. Analyzing the voltage of the DC-link capacitor and the instantaneous power, it is noticed that the *xyn*-system presents highest low-frequency oscillation in the DC-link capacitor. This can lead to the conclusion that the $\alpha\beta n$-system has lower capacitor losses. However, when high-frequency components are taken into account, the conclusions are

quite different. The RMS DC-link current is higher in the $\alpha\beta n$-system than in other systems, showing that high-frequency components can also influence losses.

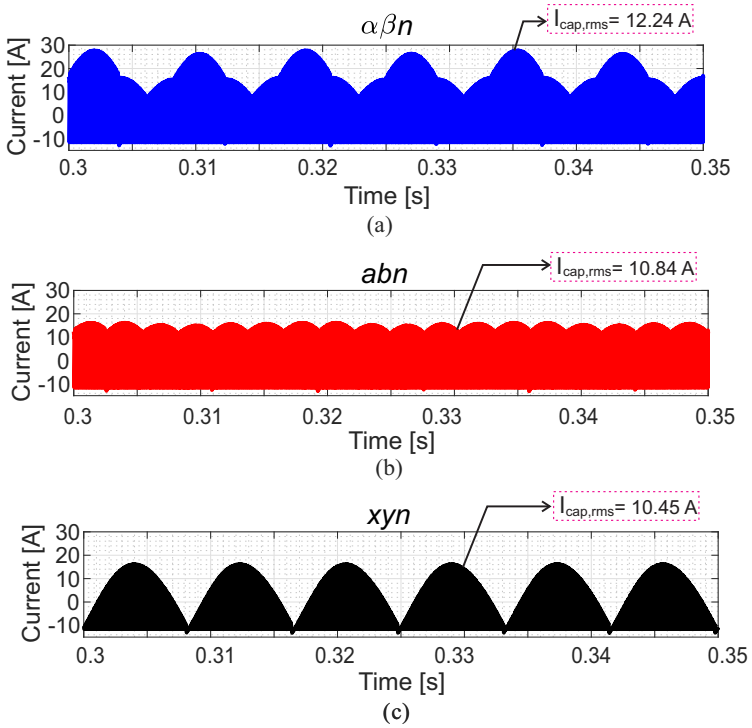

Figure 15 – DC-link capacitor current: (a) $\alpha\beta n$-system.(b) *abn*-system. (c) *xyn*-system. *Remark*: These results were obtained based on the parameters of Table I and rated power injection.

3.2 Mission profile-based reliability analysis

3.2.1 Power losses look-up table

This dissertation proposes using the mission profile-based reliability analysis applied to 2Φ3W converters. The flowchart in Figure 16 shows each step for the reliability evaluation of semiconductor power devices and DC-link capacitors. Temperature is identified as the most critical factor affecting the overall reliability of the converter components (Song; Wang, 2013).

Losses in power semiconductor devices are separated into conduction and switching losses. The IGBT losses are given as follows:

$$P_{loss,IGBT} = P_{c,IGBT} + P_{sw,IGBT}, \tag{3.13}$$

$$P_{c,IGBT} = \frac{1}{T_{sg}} \int_{t_0}^{t_0+T_{sg}} v_{ce} i_c(t) dt, \tag{3.14}$$

$$P_{sw,IGBT} = f_{sw}(E_{on} + E_{off}), \tag{3.15}$$

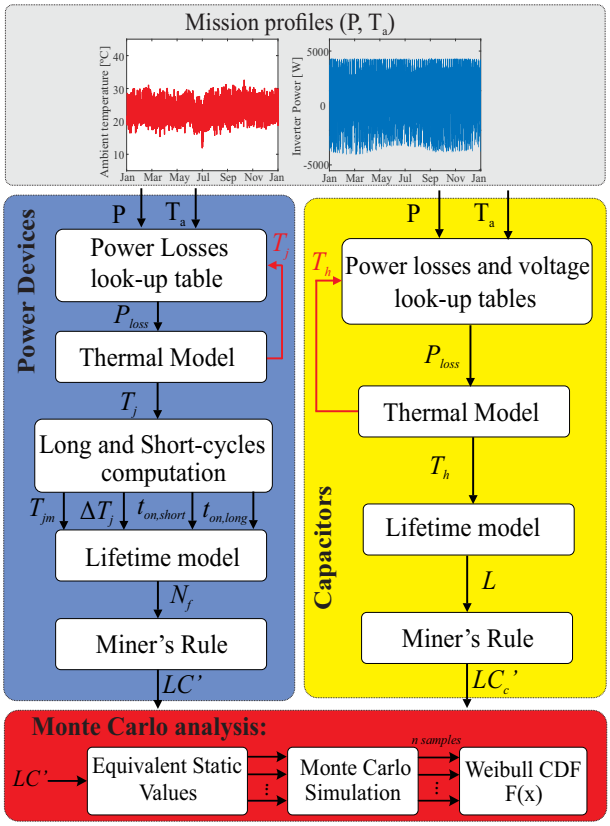

Figure 16 – Flowchart for the lifetime evaluation of semiconductor power devices and DC-link capacitors.

where $P_{c,IGBT}$ is the conduction loss, $P_{sw,IGBT}$ is the switching loss, v_{ce} is the collector-emitter voltage, i_c is the collector current, t_0 is a given start time, T_{sg} is the period of the signal, f_{sw} is the switching frequency, E_{on} and E_{off} are the turn-on and turn-off energies, respectively. The diode losses are estimated as follows:

$$P_{loss,diode} = P_{c,diode} + P_{sw,diode}, \tag{3.16}$$

$$P_{c,diode} = \frac{1}{T_{sg,d}} \int_{t_0}^{t_0+T_{sg,d}} v_f i_f(t) dt, \tag{3.17}$$

$$P_{sw,diode} = f_{sw} E_{rec}, \tag{3.18}$$

where v_f and i_f are the forward voltage and current, $T_{sg,d}$ is the period of the forward current, and E_{rec} is the recovery energy. The turn-on energy is neglected in the diode.

A one-year mission profile containing power and ambient temperature (T_a) is used to evaluate the lifetime of the GFC. The losses are estimated based on the look-up tables built according to data provided by the manufacturer. The dependence of losses with temperature and blocking voltage is considered in the estimation of power losses (Graovac; Purschel, 2009).

For capacitor losses ($P_{LOSS,cap}$), the simulation in PLECS is used to obtain current and voltage data. Then, current FFT is performed to separate the harmonic components. In the model, the dependence of the equivalent series resistance (ESR) with temperature and frequency is taken into account. The ESR frequency dependence is obtained through the equations shown in (Wang et al., 2020). Capacitor loss is calculated by adding the losses of each harmonic component. The look-up table is generated for different hot spot temperatures (0 °C to 110 °C , in steps of 10 °C) and power levels (-6 kW to 6kW, in steps of 0.5 kW) for the 2Φ3W grid-forming converter.

3.2.2 Thermal model

Semiconductor losses are integrated into a thermal model to determine the junction temperature (T_j). In this dissertation, two thermal models are employed in the results. One is the Foster thermal model, illustrated in Figure 17. The parameters of the Foster model are derived through mathematical fitting of the temperature data obtained from measurements and simulations. It is important to note that the individual RC parameters within the Foster network have no physical meaning. Furthermore, transient thermal impedance $Z_{th(jc)}$ is typically provided in data sheets using a Foster model approach (Infineon, 2020)(Sousa, 2022). The Foster model provides a straightforward analytical expression of $Z_{th,jc}$, given by:

$$Z_{th(jc)} = \sum_i R_{th,i} \left[1 - exp\left(\frac{-t}{R_{th,i} C_{th,i}} \right) \right], \tag{3.19}$$

where i is the number of nodes in the Foster network, R_{th} is the thermal resistance, and C_{th} is the thermal capacitance. The thermal resistance and thermal capacitance values of the models are obtained from the data sheets provided by the manufacturer of the IGBTs.

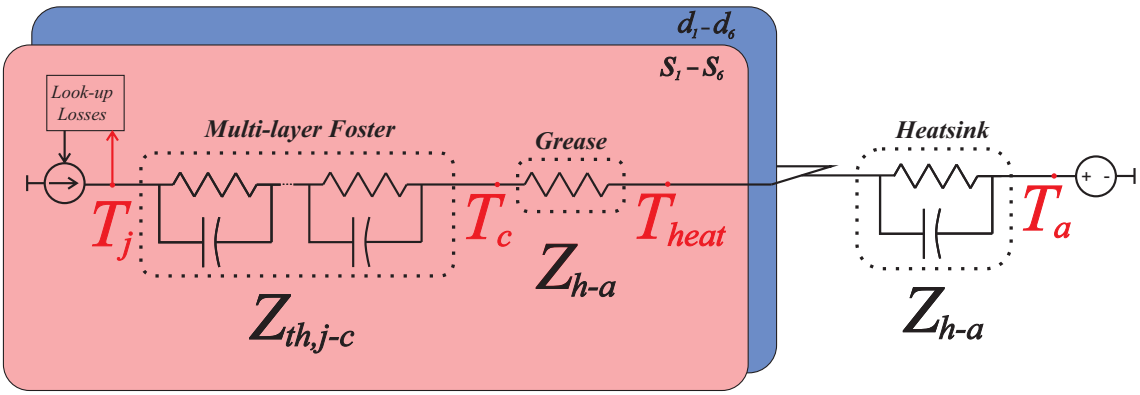

Figure 17 – Thermal model based on Foster model.

The second thermal model is a hybrid model composed of the Equivalent Cauer Model and the Multi-layer Foster Model shown in Figure 18, as performed in (Ma; Blaabjerg; Liserre, 2013). This model provides an accurate estimate of the junction and case temperature. The multilayer Foster thermal network is used for the junction

temperature estimation. This path avoids abrupt changes of case/junction temperature. The Cauer thermal network is used for the case and heatsink temperature estimation. The thermal resistance and thermal capacitance values of the models are obtained from the data sheets provided by the manufacturer. The heatsink-to-ambient thermal resistance value is sized so that the average temperature of the semiconductors does not exceed 100 °C at nominal power. This value is adjusted by observing the temperature of the semiconductors in the PLECS simulation.

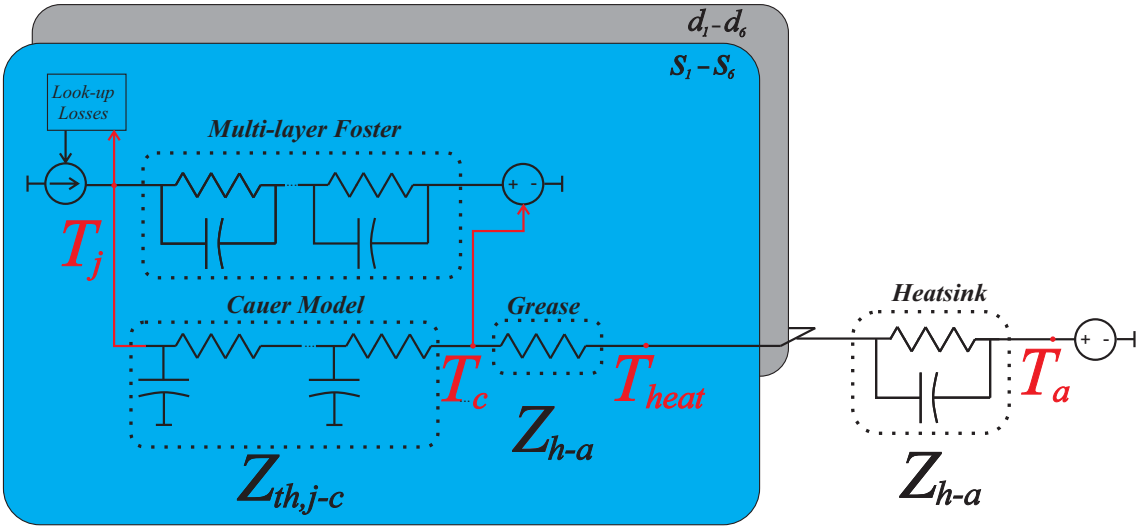

Figure 18 – Electro-thermal circuit for junction temperature estimation using the hybrid model with Cauer and Foster model.

Simulations have been carried out using a 4.5 kW 2Φ3W grid-forming converter in the PLECS software. A look-up table has been generated for the IGBTs, encompassing various input power levels (-6 kW to 6 kW in increments of 0.5 kW) and junction temperatures (-15 °C to 135 °C in increments of 15 °C). The losses of the semiconductor devices are computed directly within the software by incorporating their characteristic curves.

The thermal model used for the DC-link capacitors is shown in Figure 19. The thermal resistance of the capacitor is calculated to estimate the hot-spot temperature given by:

$$T_h = T_a + R_{ha}.P_{loss,cap}, \tag{3.20}$$

where T_a is the ambient temperature, R_{ha} is the ESR from the hotspot to ambient, and $P_{loss,cap}$ is the loss in the capacitor.

3.2.3 Long and short-cycles computation

Power semiconductor devices are subjected to different thermal cycling. The thermal cycles obtained from the models are divided into two parts: long cycles (related to mission

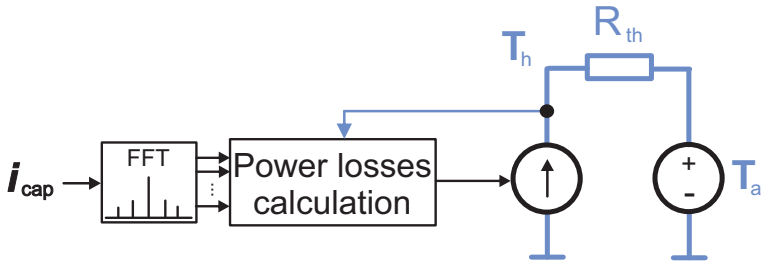

Figure 19 – Electro-thermal circuit for estimating the hot-spot temperature of the capacitor.

profile variations) and short cycles (related to the grid frequency and harmonics). The counting algorithm known as rainflow is used to extract long cycle information from the temperature profile obtained from the thermal model, extracting regular cycles from the profile obtained in the simulations. For each cycle obtained, the following parameters are estimated: heating time ($t_{on,long}$), junction temperature fluctuation, and average junction temperature.

Rainflow was first created to calculate strain stress fatigue in mechanical applications. In these applications, the time it takes to apply a deformation force does not affect the resulting fatigue. However, heating time affects fatigue calculation in estimating the useful life of semiconductor devices (Antonopoulos et al., 2020). The works that use MATLAB rainflow written by Nieslony (2003) consider that the heating time is half of the time cycle calculated by the function, based on the principle that the heating and cooling times are identical, which is not always the case. The discussions presented by Antonopoulos et al. (2020) show an alternative to modifying the original algorithm to calculate the heating time used in this dissertation.

Short cycle effects are calculated using the analytical approach proposed by Ma and Blaabjerg (2012b). The junction temperature fluctuation due to the frequency in the grid is calculated by:

$$\Delta T_j = P_{loss}\left[Z_{th}\left(\frac{1}{8f_n}\right) + 2Z_{th}\left(\frac{1}{4f_n}\right)\right], \tag{3.21}$$

where P_{loss} are the power losses dissipated on the power semiconductor device, and f_n is the grid fundamental frequency. T_{jm} is obtained directly from the thermal model where $t_{on,short}$ is constant $(1/(2f_n))$.

The primary data series obtained for short and long cycles collected through rainflow and effective heating time calculations are the starting inputs for the lifetime model. This dissertation employs an empirical lifetime model rooted in accelerated power cycling trials and draws insights from extensive databases and accumulated experience spanning numerous years. An inherent limitation of empirical models lies in their need for distinct models tailored to individual failure mechanisms (such as bond wire fatigue and solder joint fatigue). Additionally, these models face a challenge of accurately extending

predictions beyond the parameter range, thus displaying an element of imprecision in such extrapolations (Schmidt; Zeyss; Scheuermann, 2013)(Brito, 2021).

3.2.4 Lifetime model and Miner's Rule

Empirical models used to assess the lifetime are formulated regarding the number of cycles to failure (N_f). Accelerated power cycling tests are conducted to establish a relationship between N_f and factors such as junction temperature, heating duration, voltage, current, and chip technology. This dissertation applies the model developed by Bayerer et al. (2008). The Bayerer model is a statistical approach derived from analyzing more than 150 accelerated power cycling tests, encompassing various package designs by Infineon, defined by equation 3.22. This model improves previous lifetime models by incorporating chip technology details, such as current per bondfoot, blocking voltage class, and bond wire diameter. Additionally, manufacturers of power modules often do not disclose such information due to its confidential and restricted nature. Therefore, it becomes essential to ensure that these parameters remain within the specified range of values utilized during accelerated power cycling tests (Brito, 2021).

$$N_f = A(\Delta T_j)^{\beta_1} \exp(\frac{\beta_2}{T_{jm} + 273}) t_{on}^{\beta_3} I_{bf}^{\beta_4} V_{sd}^{\beta_5} D^{\beta_6}, \tag{3.22}$$

where A is the Technology Factor, β_1 is the temperature fluctuation coefficient, β_2 is the minimum junction temperature coefficient, β_3 is the pulse duration coefficient, β_4 is the current per bond-foot coefficient, β_5 is the blocking voltage coefficient, β_6 is the bond-wire diameter coefficient, I_{bf} is the current per bond-foot, V_{sd} is the blocking voltage of the power semiconductor device, and D is the bond-wire diameter. β_i, $i = 1$ to 6, are curve-fitting parameters.

It is known that the wear-out model has limitations, such as parameter sensitivity and uncertainties of power cycling, among others discussed in the literature. Lutz et al. (2020) shows the values of the parameters used in the Bayerer model and defines the operating range of the parameters according to the fluctuations of the temperature. Antonopoulos et al. (2020) point out the uncertainties that appear in the process of applying a lifetime model based on results from power-cycling experiments and on stress patterns deriving from field applications. It is important to highlight that the main objective herein is to use the lifetime estimation method as a figure of merit to compare the three configurations presented in this dissertation.

The following capacitor lifetime model is employed:

$$L = L_0 \left(\frac{v_c}{V_n} \right)^{-n} 2^{\frac{T_0 - T_h}{10}}, \tag{3.23}$$

where L is the capacitor lifetime under the hotspot temperature, L_0 (5,000 hours) is the rated lifetime given by manufactures, v_c is the test operating voltage, and V_n (420 V) is the rated voltage test condition. T_0 (85 °C) is the temperature under test conditions, and n refers to the voltage stress exponent, defined between 3 and 5. In (Albertsen, 2021) is proposed values of n as a function of the ratio $\frac{v_c}{V_n}$. For $0.8 \leq \frac{v_c}{V_n} \leq 1$, the value used herein is n equal to 5.

Finally, the accumulated damage is calculated by the Miner's Rule:

$$LC_s = \sum_{i}^{m} \frac{1}{N_{fi}}, \tag{3.24}$$

where LC_s is the semiconductor lifetime consumption evaluated over m mission profile points. For the capacitors:

$$LC_c = \sum_{i}^{m} \frac{L_i}{L_0}, \tag{3.25}$$

where LC_c is the capacitor lifetime consumption evaluated over m mission profile points. This is a conservative method to analyze the damage accumulated in capacitors and semiconductors. The Miner's rule considers that a given point of operation that causes thermal stress on the devices is the same for their entire lifetime, since the models used do not take degradation into account. However, it is still a useful figure of merit to compare the impact of different mission profiles and/or models on the damage suffered by capacitors and semiconductors (Lenz; Pinheiro, 2018).

3.2.5 Monte Carlo analysis

The lifetime model for semiconductors and capacitors results considering fixed accumulated damage is far from validation, as the variations and uncertainties in the IGBT and capacitor parameters are not considered by the statistical properties of the lifetime models in the literature. Thus, Monte Carlo simulation is used to perform a statistical analysis of the damage values found by the Miner's rule, according to the methodology proposed by Reigosa et al. (2016). The Monte Carlo simulation is performed to include the manufacturing process uncertainties and thermal variations in the lifetime consumption evaluation. This simulation allows to vary some parameters in lifetime models and observe the junction temperature behavior at various operating points, obtaining a histogram of accumulated damage for each converter component.

The Monte Carlo simulation requires organizing the inputs in a clearly defined probability function in a normal distribution. To achieve this, uneven thermal loading values must be transformed into constant values that result in identical lifetime usage. This enables the execution of the Monte Carlo simulation using a set of k samples, where distinct parameter changes are applied to each component. Firstly, Monte Carlo analysis

demands the conversion of stochastic parameters (T_{jm}, ΔT_j) into equivalent deterministic static values ($T_{jm}^{'}$, $\Delta T_j^{'}$) that result in the same lifetime, when applied to the lifetime model (Reigosa et al., 2016). The static value is a power cycling with constant parameters (amplitude, average value, and heating time) that provides the same LC_s.

Regarding the power components, the average steady junction temperature $T_{jm}^{'}$ is derived from the average value of the thermal loading pattern. Moreover, the consistent heating cycle period $t_{on,short}$ is set at the duration of one fundamental frequency heating time (1/120 s), given its increased stress on the power device. Ultimately, $\Delta T_j^{'}$ can be determined, guaranteeing an equivalent lifetime consumption as calculated in Equation 3.24. Once all the static parameters are acquired for each component, the Monte Carlo simulation can be executed, introducing parameter fluctuations for each component. In conclusion, the technology factor A is adjusted up to 20%, reflecting uncertainties in the manufacturing process (Reigosa et al., 2016) (Brito, 2021). The other lifetime parameters of the semiconductor power device were not varied due to missing information on their confidence interval.

Electrolytic capacitors experience thermal stress due to power dissipation in the ESR. Manufacturers typically do not specify the maximum variation in ESR. A 20% variation in the rated useful life (L_0) is often considered to account for uncertainties in the manufacturing process.

The results of the Monte Carlo simulation are arranged in a histogram fitted with the Weibull Probability Density Function (PDF), given by:

$$f(x) = \frac{\beta_w}{\eta^{\beta_w}} x^{\beta_w - 1} exp\left[-\left(\frac{x}{\eta_w} \right)^{\beta_w} \right], \tag{3.26}$$

where β_w is the shape parameter, η_w is the scale parameter, and x is the operation time (Sangwongwanich et al., 2018a). The cumulative density function (CDF), also called unreliability function *F(x)*, represents the proportion of population failure, according to the time obtained through the integral of PDF, given as:

$$F(x) = \int_0^x f(x)dx. \tag{3.27}$$

This unreliability function reflects failure rates at the component level, with a primary focus on failure mechanisms. To establish the unreliability at the system level, it is necessary to build a reliability block diagram that incorporates the associations of the component-level functions (Yang; Sangwongwanich; Blaabjerg, 2016). Several methodologies are available in the literature, including part-count models, combinatorial models, and state-space models. This paper employs the model found in (Song; Wang, 2013). The part-count model relies on the following assumptions: Any fault that occurs to each of the components or subsystems will cause the overall system to fail; at the

components level, the failure rates of the same components are assumed equal during useful lifetime; the system is treated as a series structure of all components or subsystems. Finally, the converter-level lifetime of is approximated as follows:

$$F_{sys}(x) = 1 - \prod_{m=1}^{H} (1 - F_m(x)) \tag{3.28}$$

where H is the number of components of the converter, and $F_m(x)$ is the unreliability computed by the CDF for each device.

3.3 Case Study

3.3.1 Characterization of Riverside Communities in Amazon Region

As shown in the previous section, the wear-out prediction method used in this dissertation requires mission profiles for statistical analysis to estimate the lifetime consumption of semiconductors. The power load profile is created considering five Brazilian riverside communities in Amazon Region (*Marabá, Monte Sinai, Pagodão, São Tomé, and Três Unidos)* found in (Gyamfi et al., 2020). Figures 20(a)-20(e) show the five load profiles of each community. These power profiles were used to create a standard profile for a riverside community.

All communities with peak values greater than 5 kW were scaled down to ensure that the peak does not exceed this value. Here, the most important aspect is the shape of the curve, not the magnitude. Each community is considered a day of consumption in a generic riverside community, where the peak consumption is 5 kW. The final result is shown in Figure 21. This 5-day pattern is repeated to obtain a one-year mission profile with a 10-minute sampling rate, shown in Figure 22(a).

The profile of the PV generation mission profile is created using data collected in (NREL, 2023), shown in Figure 22(b). The shape of the curves follows the respective solar irradiance profile, as a common characteristic of PV systems. The dynamic saturation of the PV inverter limits the output power of the inverter, 4.5 kW in this study. In this dissertation, global horizontal irradiance and temperature data in the Brazilian Amazon (2°58'48.0"S 64°52'12.0"W) are considered. The power mission profile shown in Figure 22(c) and used in the grid-forming 2Φ3W converter is the difference between load (P_{load}) and PV generation (P_{PV}). The grid-forming mission profile presents only active power.

3.3.2 Converter design for PLECS simulations

Since the objective of this work is to analyze small riverside communities, the nominal power of the converter is set at 4.5 kW. For the case study that considered an

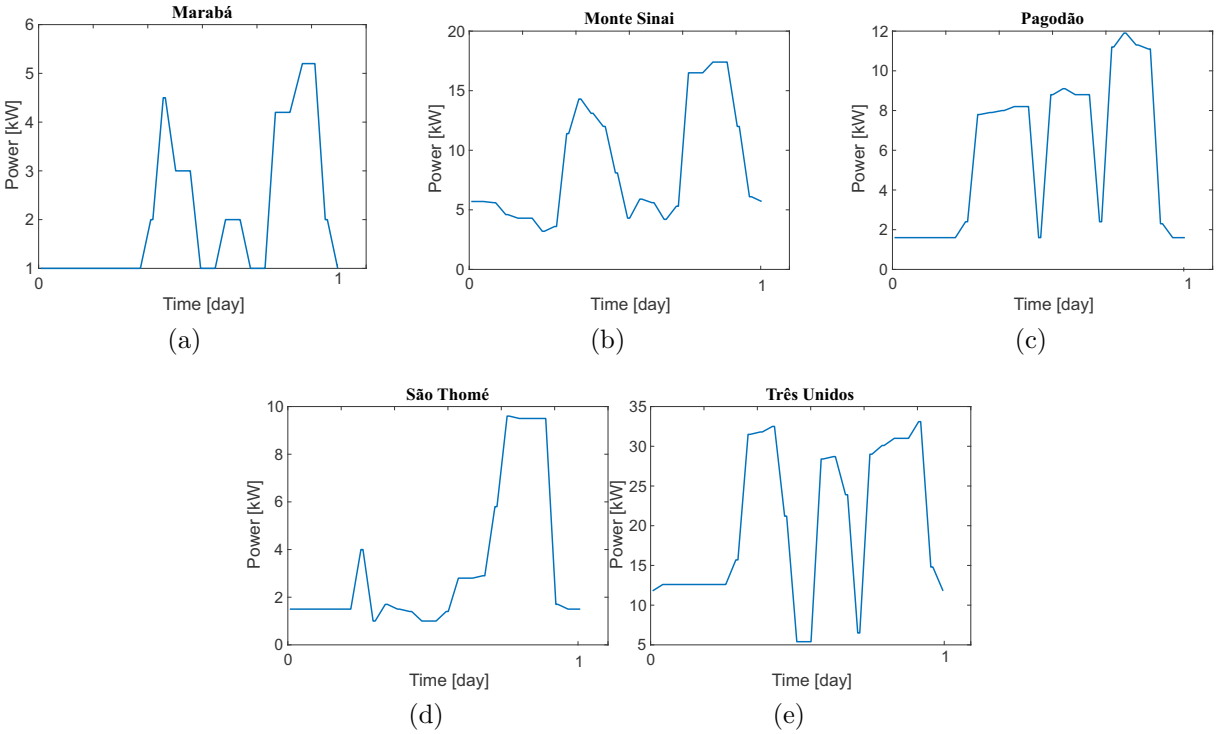

Figure 20 – Communities load profile: (a) Marabá. (b) Monte Sinai. (c) Pagodão. (d) São Thomé. (e) Três Unidos.

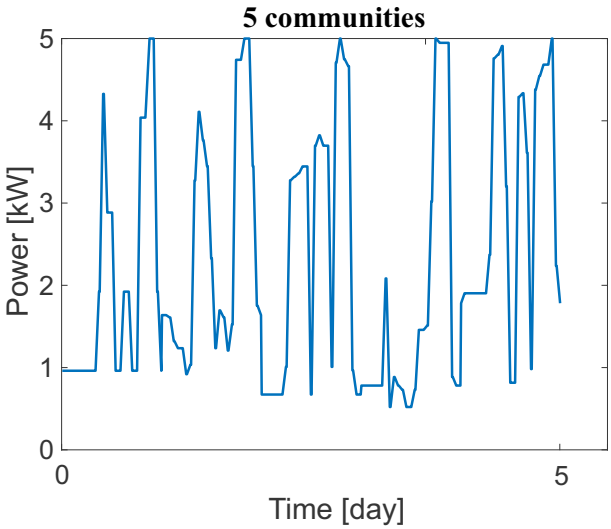

Figure 21 – Mission profile created using the 5 communities.

isolated power system in Brazil, the phase-to-neutral voltage is set at 127 V_{rms} and the line frequency at 60 Hz. The switching frequency is defined as 12 kHz. The hardware is developed for the *abn*-converter since most of the available converters on the market are designed considering a phase difference of 120° between phase voltages.

The DC bus voltage is chosen as 390 V. The DC bus capacitance is calculated considering the nominal power, the nominal phase voltage and a maximum 3% voltage fluctuation on the *abn*-converter DC bus. The total capacitance value is divided into five

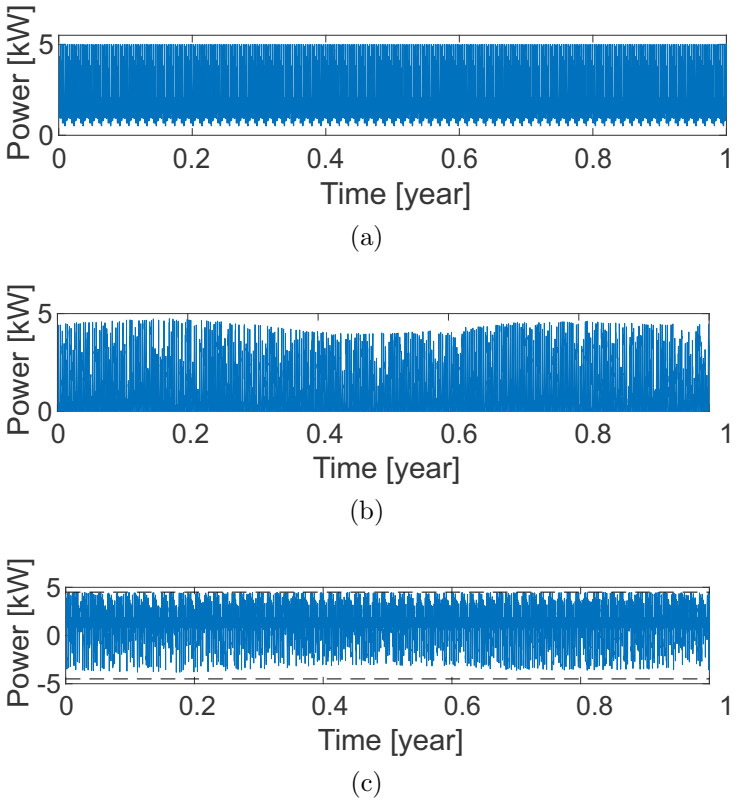

Figure 22 – Power profiles: (a) One year load of a riverside community. (b) One year PV plant generation. (c) One year 2Φ3W GFC power.

capacitors of 470 μF each, to distribute losses between multiple capacitors and reduce their operating temperature. It is important to note that the design for the xyn and $\alpha\beta n$ converters could be optimized to improve the DC bus voltage performance and minimize fluctuations. However, for comparison purposes, this dissertation uses the same hardware for all converters.

The values for the output LC filter were chosen based on previous assembly experience. A 1 mH inductor is selected and the capacitance chosen is 40 μF. For grid-forming converters, this capacitance is generally higher compared to grid-following converters.

In this study, a cascade control is used for the isolated grid-forming converter, as illustrated in Fig. 23. The outer loop regulates the line voltage through a resonant proportional-integral controller. The inner control loop is based on a resonant proportional controller. The reference voltage is sent to a PWM modulator (Chen; Chen; Yu, 2018). The current control loop is tuned using the methodology described in (Yepes et al., 2011). The discretization of resonant controllers is based on the Tustin method. The voltage control loop is tuned using the pole placement method, with a phase margin and crossover frequency of 54.4° and 532 Hz. The controller gains are shown in Table 4.

The heatsink-to-ambient thermal resistance value is sized so that the average

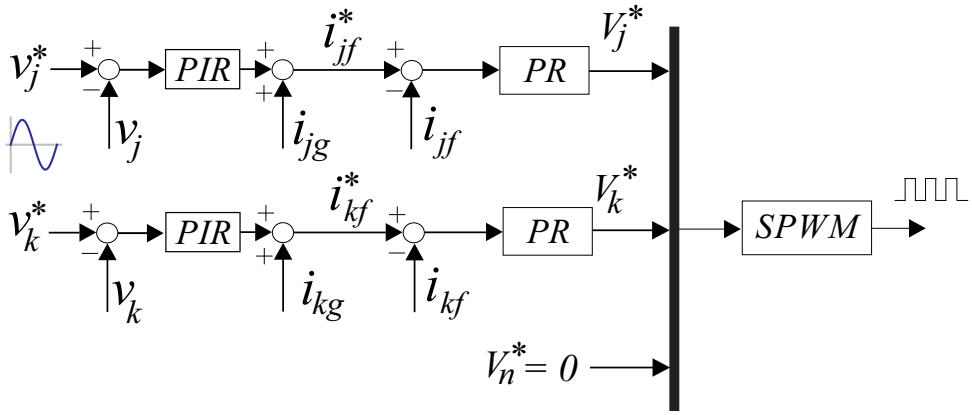

Figure 23 – Control of the isolated 2Φ3W grid-forming converter.

temperature of the semiconductors does not exceed 100 °C at nominal power. This value is adjusted by observing the temperature of the semiconductors in the PLECS simulation.

3.3.3 Open module setup

Table 4 shows the parameters used in PLECS simulations for lifetime evaluation to extract module loss information. The experimental results are obtained by means of a 2Φ3W GFC prototype, described in Table 4. Two setups were employed for the experiments. In the first, the converter design allows access to the semiconductor module for thermal images, as shown in Figure 24(a). Infineon's module has been chosen for simulations and experiment test bench, the FP25R12KE3 module. The silica gel layer was removed from the power module and the module was painted black to improve the accuracy of the measurement. The FLIR i60 thermal camera captured the thermal images. Due to the alteration of the dielectric properties caused by removing the gel layer, precautionary action was taken during the tests. The maximum voltage applied to the DC bus was limited to 150 V for safety reasons. Moreover, the value of the switching frequency was twice that of the simulation for the sake of attaining higher thermal stress at lower power levels.

The position of the IGBTs and diodes is shown in Figure 24(b). The subscripts j, k, and n refer to the phase of the converter, and the subscript h refers to the high-side semiconductors (positioned on the left side of the image) and l stands for the low-side semiconductors (positioned on the right side of the image).

3.3.4 Discrete IGBT setup

The second setup consists of a three-phase full-bridge converter shown in Figure 25. For semiconductors, the IXYS model IXBH20N300 IGBTs were selected. The rated current for these IGBTs is 20 A. The gate driver used is the 2SD315AI from Power Integrations. The experimental setup parameters are shown in Table 4. This prototype was developed

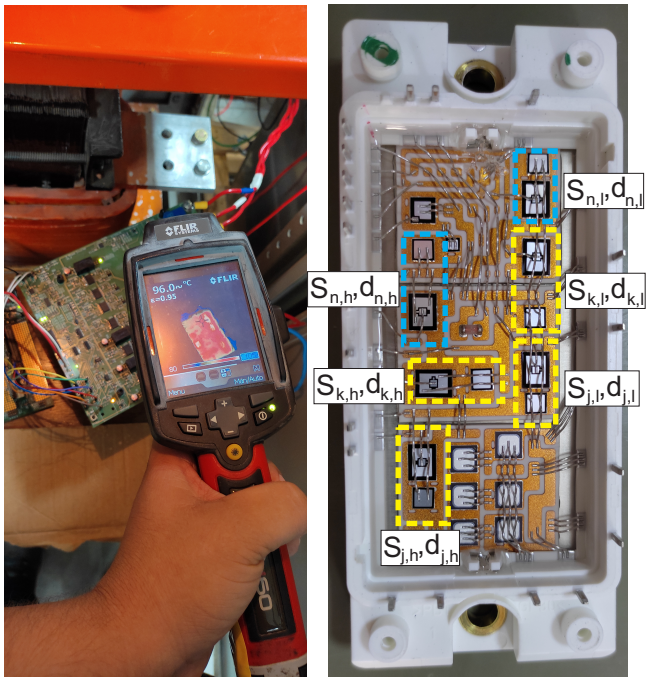

(a) (b)

Figure 24 – (a) Thermal measurement of the prototype semiconductors. (b) Top view of the open semiconductor module FP25R12KE3 by Infineon. In yellow are highlighted the phase semiconductors and in blue the neutral semiconductors.

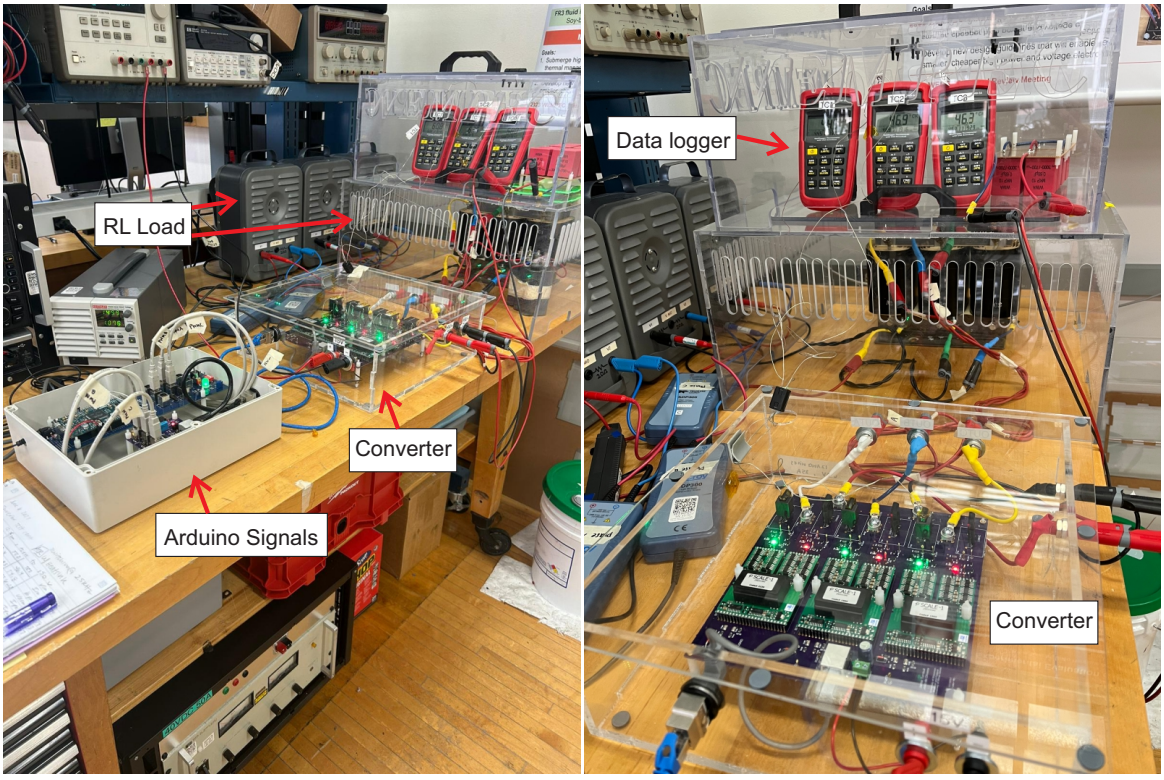

(a) (b)

Figure 25 – (a) Experimental test bench. (b) Detailed three-phase full-bridge converter of the experimental test bench.

Table 4 – Parameters of the isolated 2Φ3W GFC.

PLECS	
Parameter	Value
Converter rated power	4.5 kW
Phase-to-neutral voltage	127 V_{rms}
Line frequency	60 Hz
Switching frequency	12 kHz
DC-link capacitor (C)	5x470 μF
DC-link voltage	390 V
Output filter capacitor (C_f)	40 μF
Output filter inductors (L_{f1}, L_{f2}, L_{f3})	1 mH,
Output filter X/R ratio	20
Damping resistor	4 Ω
Voltage controller	$K_i = 123.37$, $K_p = 0.1359$, $K_{res} = 200$
Current controller	$K_p = 18.541$, $K_{res} = 2000$
Heatsink-to-ambient thermal resistance	0.13 K/W
Experimental setup - Open module	
Parameter	Value
DC-link voltage	150 V
Switching frequency	24 kHz
Line frequency	60 Hz
Load inductance	1.2 mH
Load resistance	8 Ω
Output filter capacitor	40 μF
Experimental setup - discrete IGBT	
Parameter	Value
DC-link voltage	80 V
Switching frequency	10 kHz
Line frequency	50 Hz
Load inductance	5 mH
Load resistance	40 Ω

and assembled at the Wisconsin Electric Machines and Power Electronics Consortium (WEMPEC) at the University of Wisconsin Madison, where the author was a visiting student for 10 months.

Experiments were conducted to analyze semiconductor power losses and semiconductor temperatures in two-phase three-wire converters. To analyze the losses, the Yokogawa WT1800 is used to measure the losses of the converter switches, as shown in Figure 26. The experiment varies the DC link voltage while keeping the RL load fixed at the converter output. Note that heatsinks or heat extraction techniques were not used on the semiconductors. For higher accuracy, the current measurement used by the meter is

the shunt measurement, where the current passes through a sensor inside the equipment.

Due to the encapsulation of the discrete IGBTs used in the prototype, direct access to the junction temperature was not possible. As an alternative, the case temperature of the IGBTs was monitored. K-type thermocouples were attached to the IGBT cases. Measurements were carried out for the top IGBT of phase and neutral legs. To record temperature data, the Amprobe TMD-56 datalogger was used, which captures temperatures at 10-second intervals throughout the test. The temperature measurement test lasted 3 hours and each converter operated for one hour at a constant voltage value on the DC link of 150 V. The line frequency of this prototype is 50 Hz because it was developed in the USA, where the distribution system frequency is set at that value.

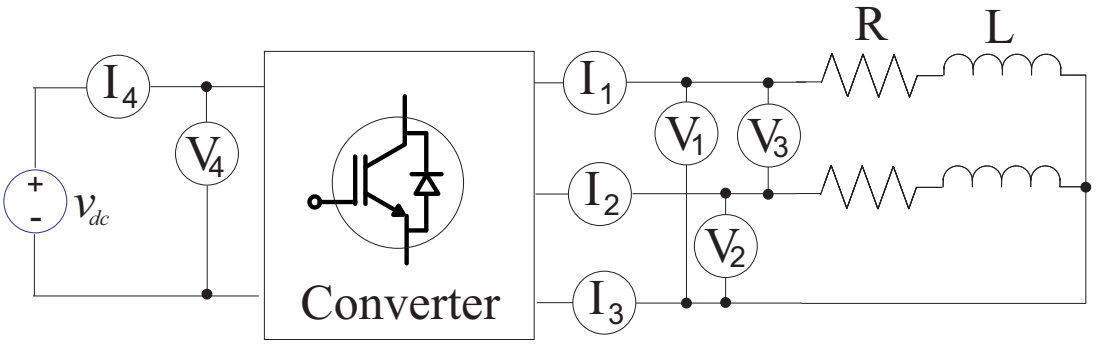

Figure 26 – Power analyzer connections for semiconductor losses measurement.

3.4 Chapter closure

This chapter provided detailed information on the 2Φ3W systems studied in this thesis. A remote community was characterized based on data from riverside communities in the Amazon region for the reliability study.

The adopted reliability method was explained in detail. The method based on mission profile will be used as a figure of merit for the analysis of the 2Φ3W converters. Two setups were developed for experiments. The results are important for measuring the thermal stress of converters. The next chapter presents analytical equations for analyzing current stress in semiconductor and capacitor devices of 2Φ3W converters.

4 Current stresses evaluation in two-phase three-wire converters

In this chapter, analytical equations are proposed to evaluate current stress under general load conditions. In the conducted analyses, load unbalances are considered, both in terms of current amplitude and the angle displacement between voltage and current in each phase. These results are essential for understanding the wear-out outcomes obtained later for two-phase three-wire converters.

4.1 Proposed semiconductors current stresses evaluation for general load condition

Analytical expressions are obtained for the average current (I_{AVG}) and the RMS current (I_{RMS}) in power devices (S_1-S_6 and d_1-d_6), to evaluate the current stress of semiconductors in the 2Φ3W converters. The analytical model neglects the current ripple in the converter output and considers perfect sinusoidal signal modulation for sinusoidal pulse-width modulation (SPWM) shown in Figure 27. The duty cycle δ of the voltage pulses is obtained by comparing the modulation signal ($v_{(j,k,n),n}$) with the carrier signal (v_{cr}) given by:

$$\delta = \frac{1}{2}[1 + Mv_{(j,k,n),m}], \tag{4.1}$$

where M is the modulation index given by:

$$M = \frac{2V_L}{v_{DC}}, \tag{4.2}$$

where v_{DC} is the DC-link voltage. This definition assumes balanced voltages at the output of the converter. As it is a grid-forming converter, this premise is valid because it is a consequence of the operation of this type of converter.

Current flows through the IGBT during the switching period T_s, as shown in Figure 28. The calculation of the average and RMS currents is based on the approach derived in Bierhoff and Fuchs (2004), which has calculated the current stress for a three-phase converter under balanced load conditions and has been adapted for the 2Φ3W converter. The average and RMS currents are given by:

$$I_{AVG} = \frac{1}{T}\int_{t_0}^{T+t_0} \delta i_t.dt, \tag{4.3}$$

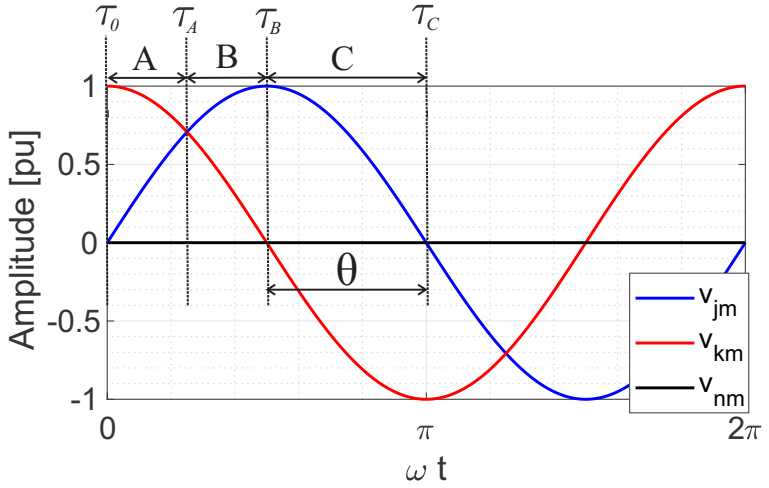

Figure 27 – 2Φ3W reference signals for SPWM. θ is the displacement angle of the voltage references, which can assume 90°, 120° or 180°. Regions A, B, and C are a division of half of the fundamental period, used to calculate the current stress of the DC-link capacitor.

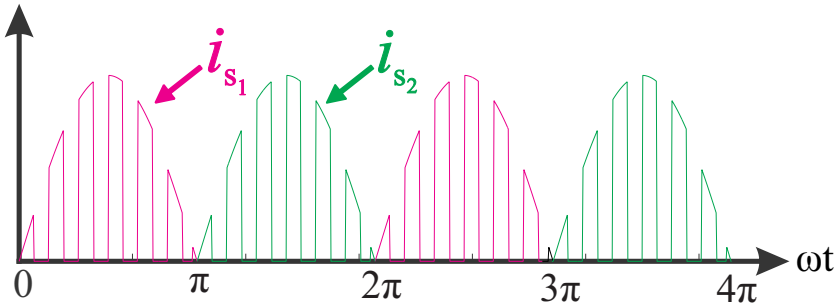

Figure 28 – Collector currents of IGBTs S_1 and S_2.

$$I_{RMS}^2 = \frac{1}{T}\int_{t_0}^{T+t_0} \delta i_t^2 . dt. \tag{4.4}$$

where T is half of the fundamental period of the current.

4.1.1 $\alpha\beta n$ semiconductors current stress evaluation

In this converter configuration, $\theta = \frac{\pi}{2}$. The output converter currents are defined by:

$$\begin{cases} i_j(t) = I_j \sin(\omega t + \phi_j) \\ i_k(t) = I_k \sin(\omega t + \phi_k + \pi/2) \\ i_n(t) = -i_j(t) - i_k(t) \end{cases} \tag{4.5}$$

The average current trough the phase leg semiconductor S_1 at the $\alpha\beta n$ converter consider the duty cycle as:

$$\delta_{S_1} = \frac{1}{2}[1 + M v_{jn}] = \frac{1}{2}[1 + M \sin(\omega t)]. \tag{4.6}$$

Using equations (4.3), (4.4), (4.5), and (4.6), the average and RMS currents through the switch S_1 are:

$$I_{AVG,S_1} = \frac{1}{\pi}\int_0^{\pi}\frac{1}{2}\left[I_j\sin(\omega t+\phi_j) + MI_j\sin(\omega t)\sin(\omega t+\phi_j)\right]d\omega t, \tag{4.7}$$

$$I_{AVG,S_1} = \frac{I_j}{\pi} + \frac{MI_j}{4}\cos(\phi_j). \tag{4.8}$$

$$I^2_{RMS,S_1} = \frac{1}{\pi}\int_0^{\pi}\frac{1}{2}[1+M\sin(\omega t)]I_j^2\sin^2(\omega t+\phi_j)d\omega t, \tag{4.9}$$

$$I_{RMS,S_1} = I_j\sqrt{\frac{1}{4}+\frac{2M\cos(\phi_j)}{3\pi}}. \tag{4.10}$$

The average and RMS currents stress for the switch S_2 is similar to S_1 presented in this section, regardless of the adopted converter configuration. The procedure for the switches S_3 and S_4 differs in the peak current, which is I_k instead I_j, and ϕ_k instead of ϕ_j.

The procedure for evaluating current stress for the diodes is similar to that for IGBTs. The difference is the duty cycle. As example, the duty cycle for diode d_1 is given by:

$$\delta_{d_1} = 1-\frac{1}{2}[1+Mv_{jn}] = 1-\frac{1}{2}[1+M\sin(\omega t)]. \tag{4.11}$$

Thus, the average and RMS current stress for the diode d_1 are:

$$I_{AVG,d_1} = \frac{I_j}{\pi} - \frac{MI_j}{4}\cos(\phi_j). \tag{4.12}$$

$$I_{RMS,d_1} = I_j\sqrt{\frac{1}{4}-\frac{2M\cos(\phi_j)}{3\pi}}. \tag{4.13}$$

The average and RMS currents stress for the diode d_2 is similar to the diode d_1 regardless of the adopted converter configuration. For diodes d_3 and d_4, the difference is the peak current which is I_k instead of I_j, and ϕ_k instead of ϕ_j.

As shown in Figure 27, the modulation signal to compare with the carrier signal for neutral IGBTs is a constant signal (v_{nm}=0). Therefore, the duty cycle for neutral semiconductors does not depend on the modulation index and presents a constant value ($\delta = \frac{1}{2}$). Figure 29 shows the currents at the output of each converter topology, considering balanced load conditions, highlighting the period when the switch S_5 conducts during the positive half-cycle of the neutral current.

The integration interval for calculating the average and RMS current of the neutral leg switches depends on the neutral current. Figure 29 shows the current and the intervals for the balanced load conditions at the converter output. In an unbalanced load condition,

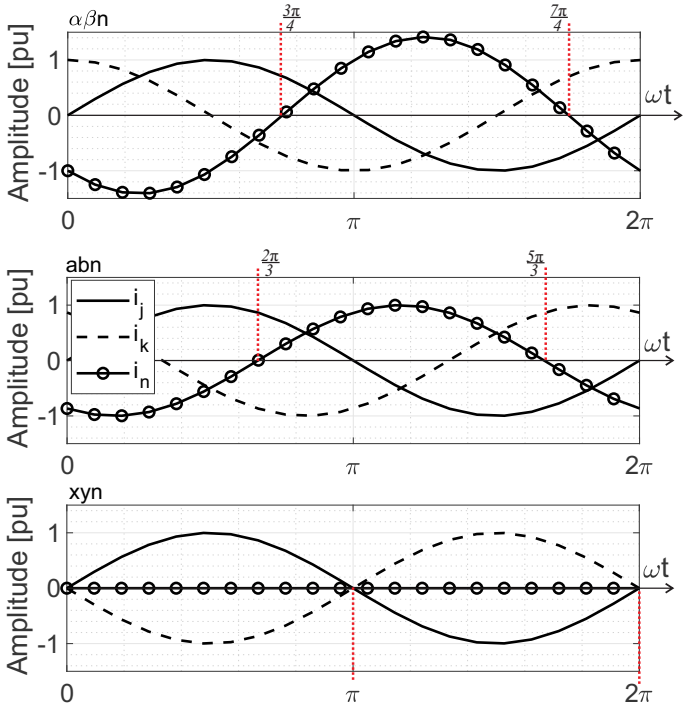

Figure 29 – Phase current of the 2Φ3W converters: $\alpha\beta n$, abn, and xyn. Balanced load conditions.

either in current amplitude or in angular phase displacement between voltage and current in the phases, the integration interval changes.

In this dissertation, these two types of unbalance are considered separately for the analysis of current stress in neutral semiconductor devices. Next, equations for average and RMS current are derived for the three converter topologies studied, taking this unbalance into account. The average and RMS current stresses on switch S_5 are as follows:

$$I_{AVG,S_5} = \frac{1}{\pi}\int_{\psi_i}^{\psi_f} \frac{1}{2} i_n(t)dt = \frac{1}{\pi}\int_{\psi_i}^{\psi_f} \frac{1}{2}\left[-I_j \sin(\omega t + \phi_j) - I_k \sin(\omega t + \phi_k + \theta)\right] d\omega t, \quad (4.14)$$

$$I^2_{RMS,S_5} = \frac{1}{\pi}\int_{\psi_i}^{\psi_f} \frac{1}{2} i^2_n(t)dt = \frac{1}{\pi}\int_{\psi_i}^{\psi_f} \frac{1}{2}\left[-I_j \sin(\omega t + \phi_j) - I_k \sin(\omega t + \phi_k + \theta)\right]^2 d\omega t, \quad (4.15)$$

where ψ_i and ψ_f are the start and end of the integration period. Equations (4.14) and (4.15) can be used for the three converters studied in this dissertation. The difference for each topology is the integration interval.

Note that for neutral semiconductors the duty cycle is identical for IGBTs and diodes. Therefore, the current stress is the same for semiconductors from the same converter.

4.1.1.1 Current stress for amplitude current unbalance in $\alpha\beta n$-converters

For this analysis, $I_j \neq I_k$, $\phi_j = \phi_k = \phi$. In this case, the integration interval to obtain the current stress occurs when the neutral current is equal to zero, thus:

$$-I_j \sin(\psi_i) - I_k \sin(\psi_i + \pi/2) = 0 \Leftrightarrow \tag{4.16}$$

$$-I_j \sin(\psi_i) - I_k \cos(\psi_i) = 0 \Leftrightarrow \tag{4.17}$$

$$\frac{\sin(\psi_i)}{\cos(\psi_i)} = -\frac{I_k}{I_j} \Leftrightarrow \tag{4.18}$$

$$\tan(\psi_i) = -\frac{I_k}{I_j} \Leftrightarrow \tag{4.19}$$

$$\psi_i = \arctan(-\frac{I_k}{I_j}). \tag{4.20}$$

The integration interval is then defined by:

$$\begin{cases} \psi_{i,\alpha\beta n,AU} = \arctan(-\frac{I_k}{I_j}), \\ \psi_{f,\alpha\beta n,AU} = \arctan(-\frac{I_k}{I_j}) + \pi. \end{cases} \tag{4.21}$$

where the subscript AU represents the current amplitude unbalance analysis.

The average and RMS currents for the $\alpha\beta n$-converter, using Equations (4.14), (4.15), and (4.21) are:

$$I_{AVG,S_5,\alpha\beta n,AU} = \frac{\sqrt{I_j^2 + I_k^2}\cos(\phi)}{\pi}, \tag{4.22}$$

$$I^2_{RMS,S_5,\alpha\beta n,AU} = \frac{1}{4}\left(I_j^2 + I_k^2\right) \tag{4.23}$$

4.1.1.2 Current stress for different angle displacements unbalance in $\alpha\beta n$-converters

For this analysis, $I_j = I_k$, $\phi_j \neq \phi_k$. As explained in previous subsection, the integration interval to obtain the current stress occurs when the neutral current is equal to zero, thus:

$$-I_j \sin(\omega t + \phi_j) - I_k \sin(\omega t + \phi_k + \theta) = 0 \Leftrightarrow \tag{4.24}$$

$$-\sin(\omega t + \phi_j) = \sin(\omega t + \phi_k + \theta) \Leftrightarrow \tag{4.25}$$

$$\sin(-\omega t - \phi_j) = \sin(\omega t + \phi_k + \theta) \Leftrightarrow \tag{4.26}$$

$$-\omega t - \phi_j = \omega t + \phi_k + \theta. \tag{4.27}$$

The integration interval is then defined by:

$$\begin{cases} \psi_{i,\phi U} = -\frac{\phi_j + \phi_k + \theta}{2}, \\ \psi_{f,\phi U} = -\frac{\phi_j + \phi_k + \theta}{2} + \pi. \end{cases} \tag{4.28}$$

where the subscript ϕU represents the different angle displacements unbalance analysis.

The average and RMS currents for the $\alpha\beta n$-converter, using Equations (4.14), (4.15), and (4.28) are:

$$I_{AVG,S_5,\phi U} = \frac{(I_j + I_k)\cos\left[\frac{1}{2}\left(\theta + \phi_k - \phi_j\right)\right]}{\pi}, \tag{4.29}$$

$$I^2_{RMS,S_5,\phi U} = \frac{1}{4}\left[I_j^2 + 2I_jI_k\cos(\theta + \phi_k - \phi_j) + I_k^2\right], \tag{4.30}$$

$$I_{AVG,S_5,\alpha\beta n,\phi U} = \frac{(I_j + I_k)\cos\left[\frac{1}{2}\left(\pi/2 + \phi_k - \phi_j\right)\right]}{\pi}, \tag{4.31}$$

$$I^2_{RMS,S_5,\alpha\beta n,\phi U} = \frac{1}{4}\left[I_j^2 + 2I_jI_k\cos(\pi/2 + \phi_k - \phi_j) + I_k^2\right]. \tag{4.32}$$

4.1.2 *abn* semiconductors current stress evaluation

As mentioned previously, the current stress on the phase IGBTs maintains consistency with the earlier calculations. In relation to the current stress on the switches of the *abn*-converter, a value of $\theta = 2\pi/3$ is considered. This leads to the definition of the output currents as follows:

$$\begin{cases} i_j(t) = I_j\sin(\omega t + \phi_j), \\ i_k(t) = I_k\sin(\omega t + \phi_k + 2\pi/3), \\ i_n(t) = -i_j(t) - i_k(t). \end{cases} \tag{4.33}$$

4.1.2.1 Current stress for amplitude current unbalance in *abn*-converters

For this analysis, $I_j \neq I_k$, $\phi_j = \phi_k = \phi$. In this case, the integration interval to obtain the current stress occurs when the neutral current is equal to zero, thus:

$$-I_j\sin(\psi_i) - I_k\sin(\psi_i + 2\pi/3) = 0 \Leftrightarrow \tag{4.34}$$

$$-I_j\sin(\psi_i) - I_k\left(\frac{\sqrt{3}}{2}\cos(\psi_i) - \frac{1}{2}\sin(t_i)\right) = 0 \Leftrightarrow \tag{4.35}$$

$$\frac{\sqrt{3}}{2}\frac{\cos(\psi_i)}{\sin(\psi_i)} = \frac{1}{2} - \frac{I_k}{I_j} \Leftrightarrow \tag{4.36}$$

$$\tan(\psi_i) = \frac{\frac{\sqrt{3}}{2}}{\frac{1}{2} - \frac{I_j}{I_k}} \Leftrightarrow \tag{4.37}$$

$$\psi_i = \arctan\left(\frac{\frac{\sqrt{3}}{2}}{\frac{1}{2} - \frac{I_j}{I_k}}\right). \tag{4.38}$$

The integration interval is then defined by:

$$\begin{cases} \psi_{i,abn,AU} = \arctan\left(\frac{\frac{\sqrt{3}}{2}}{\frac{1}{2}-\frac{I_j}{I_k}}\right), \\ \psi_{f,abn,AU} = \arctan\left(\frac{\frac{\sqrt{3}}{2}}{\frac{1}{2}-\frac{I_j}{I_k}}\right) + \pi. \end{cases} \tag{4.39}$$

The average and RMS currents for the *abn*-converter, using Equations (4.14), (4.15), and (4.39) are:

$$I_{AVG,S_5,abn,AU} = \frac{(I_k - 2I_j)\sqrt{\frac{I_j^2 - I_j I_k + I_k^2}{(I_k - 2I_j)^2}}\cos(\phi)}{\pi}, \tag{4.40}$$

$$I^2_{RMS,S_5,abn,AU} = \frac{1}{4}\left(I_j^2 - I_j I_k + I_k^2\right) \tag{4.41}$$

4.1.2.2 Current stress for different angle displacements unbalance in *abn*-converters

For this analysis, $I_j = I_k$, $\phi_j \neq \phi_k$. The average and RMS currents for the *abn*-converter, using $\theta = 2\pi/3$ and Equations (4.14), (4.15) and (4.28) are:

$$I_{AVG,S_5,abn,\phi U} = \frac{(I_j + I_k)\cos\left[\frac{1}{2}\left(2\pi/3 + \phi_k - \phi_j\right)\right]}{\pi}, \tag{4.42}$$

$$I^2_{RMS,S_5,abn,\phi U} = \frac{1}{4}\left[I_j^2 + 2I_j I_k \cos(2\pi/3 + \phi_k - \phi_j) + I_k^2\right]. \tag{4.43}$$

4.1.3 *xyn* semiconductors current stress evaluation

At a voltage angular displacement of $\theta = \pi$, the currents at the output of the *xyn*-converter are defined as follows:

$$\begin{cases} i_j(t) = I_j \sin(\omega t + \phi_j), \\ i_k(t) = I_k \sin(\omega t + \phi_k + \pi), \\ i_n(t) = -i_j(t) - i_k(t). \end{cases} \tag{4.44}$$

4.1.3.1 Current stress for amplitude current unbalance in *xyn*-converters

For this analysis, $I_j \neq I_k$, $\phi_j = \phi_k = \phi$. In the *xyn*-converter, the integration interval is not affected by the current amplitude in the phases, thus:

$$\begin{cases} \psi_{i,xyn,AU} = \pi, \\ \psi_{f,xyn,AU} = 2\pi. \end{cases} \tag{4.45}$$

The average and RMS currents for the *abn*-converter, using Equations (4.14), (4.15), and (4.45) are:

$$I_{AVG,S_5,xyn,AU} = \frac{(I_j - I_k)\cos(\phi)}{\pi}, \tag{4.46}$$

$$I^2_{RMS,S_5,xyn,AU} = \frac{1}{4}\left(I_j - I_k\right)^2. \tag{4.47}$$

4.1.3.2 Current stress for different angle displacements unbalance in *xyn*-converters

For this analysis, $I_j = I_k$, $\phi_j \neq \phi_k$. The average and RMS currents for the *abn*-converter, using $\theta = \pi$ and Equations (4.14), (4.15) and (4.28) are:

$$I_{AVG,S_5,xyn,\phi U} = \frac{(I_j + I_k)\cos\left[\frac{1}{2}(\pi + \phi_k - \phi_j)\right]}{\pi}, \tag{4.48}$$

$$I^2_{RMS,S_5,xyn,\phi U} = \frac{1}{4}\left[I_j^2 + 2I_jI_k\cos(\pi + \phi_k - \phi_j) + I_k^2\right]. \tag{4.49}$$

Table 5 summarizes the expressions proposed for semiconductors, considering a generic 2Φ3W converter. The unbalanced load is taken into account in the current stress evaluation assuming the following relation in the phase currents:

$$I_k = \sigma I_j, \tag{4.50}$$

where σ is the unbalance factor, the ratio between the peak currents of phase k and phase j. The converter is under balanced load conditions when $\sigma = 1$.

4.1.4 Balanced load conditions - semiconductors

The expressions of Table 5 are compared with simulations developed in PLECS for balanced load conditions, i.e., $\sigma = 1$, and $\phi_j = \phi_k = 0$. The RMS current stress is plotted in per unit (pu) values of the rated current. For all results in this chapter, the nominal current is adopted as the base value. Displacement angles between voltage and current from $-\pi$ to π are considered to draw some conclusions about both inverter and rectifier operation modes (i.e., discharging and charging the BESS embedded in the 2Φ3W converter). At this point, the following conclusions are stated:

- The average current through the semiconductors of the phase legs is the same regardless of the converter adopted, due to the SPWM modulation. In the IGBTs, the average current decreases as the converter exchanges capacitive or inductive reactive power, while the opposite behavior is observed through the diodes. The RMS current in the converter follows the same behavior as the average current, as shown in Figure 30. The RMS current of the diodes is shown in Figure 31.

- When the converter injects active power into the grid ($\frac{-\pi}{2} < \phi < \frac{\pi}{2}$), the higher the modulation index, the higher the RMS current. When the rectifier absorbs active power ($-\pi < \phi < \frac{-\pi}{2}$ and $\frac{\pi}{2} < \phi < \pi$), the lower the modulation index, the higher the RMS current. The behavior of the diodes is contrary.

- Table 5 reveals that the loading currents of S_5, S_6, d_5, and d_6 do not depend on the modulation index. Since the converters show different neutral currents, different stresses are obtained for S_5, S_6, d_5, and d_6.

Table 5 – Proposed analytical expressions of current stresses on the power semiconductor devices of 2Φ3W converter.

System	I_{AVG}	I_{RMS}
S_1-S_4		
All systems	$\frac{I_{j,k}}{\pi} + \frac{M I_{j,k}\cos\phi_{j,k}}{4}$	$I_{j,k}\sqrt{\frac{1}{4} + \frac{2M\cos\phi_{j,k}}{3\pi}}$
d_1-d_4		
All systems	$\frac{I_{j,k}}{\pi} - \frac{M I_{j,k}\cos\phi_{j,k}}{4}$	$I_{j,k}\sqrt{\frac{1}{4} - \frac{2M\cos\phi_{j,k}}{3\pi}}$
S_5-S_6, d_5-d_6		
Amplitude unbalance		
$\alpha\beta n$	$\frac{\sqrt{I_j^2+I_k^2}\cos(\phi)}{\pi}$	$\sqrt{\frac{I_j^2+I_k^2}{4}}$
abn	$\frac{(I_k-2I_j)\sqrt{\frac{I_j^2-I_jI_k+I_k^2}{(I_k-2I_j)^2}}\cos(\phi)}{\pi}$	$\sqrt{\frac{I_j^2-I_jI_k+I_k^2}{4}}$
xyn	$\frac{(I_j-I_k)\cos(\phi)}{\pi}$	$\sqrt{\frac{(I_j-I_k)^2}{4}}$
Angle displacement unbalance		
$\alpha\beta n$	$\frac{(I_j+I_k)\cos\left[\frac{1}{2}(\pi/2+\phi_k-\phi_j)\right]}{\pi}$	$\sqrt{\frac{I_j^2+2I_jI_k\cos(\pi/2+\phi_k-\phi_j)+I_k^2}{4}}$
abn	$\frac{(I_j+I_k)\cos\left[\frac{1}{2}(2\pi/3+\phi_k-\phi_j)\right]}{\pi}$	$\sqrt{\frac{I_j^2+2I_jI_k\cos(2\pi/3+\phi_k-\phi_j)+I_k^2}{4}}$
xyn	$\frac{(I_j+I_k)\cos\left[\frac{1}{2}(\pi+\phi_k-\phi_j)\right]}{\pi}$	$\sqrt{\frac{I_j^2+2I_jI_k\cos(\pi+\phi_k-\phi_j)+I_k^2}{4}}$

- The maximum error between the simulations and the analytical model is 1.5%.

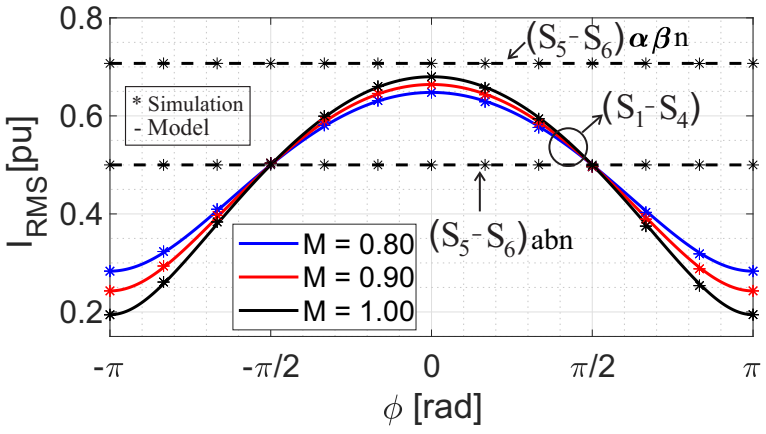

Figure 30 – RMS current through the IGBTs. Switches S_5-S_6 in the *xyn*-system have zero current value. ϕ is the displacement angle between voltage and current.

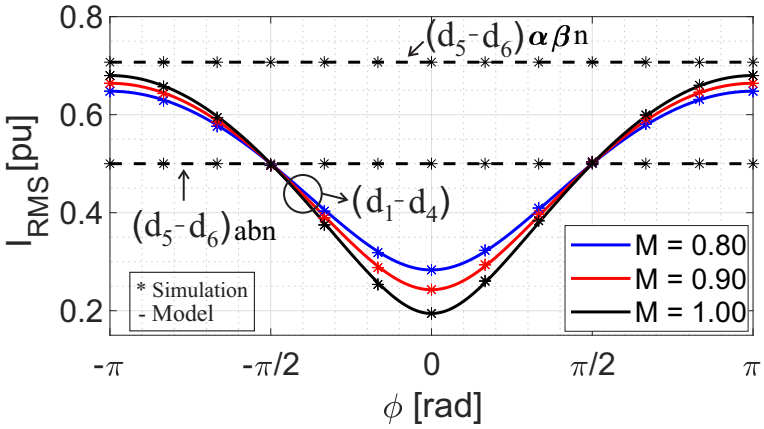

Figure 31 – RMS current through the diodes. Switches S_5-S_6 in the *xyn*-system have zero current value. ϕ is the displacement angle between voltage and current.

4.1.5 Unbalanced load conditions - semiconductors

4.1.5.1 Effect of current amplitude unbalance ($I_j \neq I_k$, $\phi_j = \phi_k$)

The behavior of current stress in semiconductors is analyzed when the system experiences an unbalance in current amplitude, and the phase currents exhibit the same angular displacement in relation to the phase voltages (i.e., $\phi_j = \phi_k = \phi$). Figure 32 shows the currents through the switches S_1, S_3, and S_5 under current unbalance in the phase legs of 2Φ3W converters, considering $\phi_j = \phi_k = \phi = 0$. The RMS values of the current stress, obtained using Table 5, are plotted in per unit (pu) values of the rated current. Due to the SPWM modulation, the current stress only differs on the neutral leg. When the converter is under balanced load condition, the current through the switches S_1 and S_3 is the same. However, when $\sigma \neq 1$, the current through the switch S_3 increases with an increase of σ. Regardless of the value of the unbalance factor, the RMS current through switch S_5 is always lower in the *xyn*-GFC than in the other two converters, leading to a lower loss. The $\alpha\beta n$-GFC shows the highest loss value in neutral switches, regardless of the current unbalance between the phases. The values of the analytical equations were compared with the simulations carried out in PLECS for several operating points, as shown in Fig. 32. The maximum error obtained between the simulation and the equations is 0.1%.

In the literature, it is advised that loads should be distributed in the system equally among phases, and the maximum value adopted for the difference in maximum current from one phase to another should be 10% (Cruz; Aniceto, 2019). Figure 33 shows the effect of the current unbalance on the neutral switches for each converter for a different angle displacement between voltage and current. Regardless of the value of σ, the *xyn*-GFC shows the lowest stress value under current amplitude unbalanced load conditions.

4.1.5.2 Effect of different angle displacements (I_j=I_k, $\phi_j \neq \phi_k$)

For this analysis, identical current amplitudes in phases are considered ($I_j = I_k$ = 1 pu), and the effects of different angular displacements between voltage and current

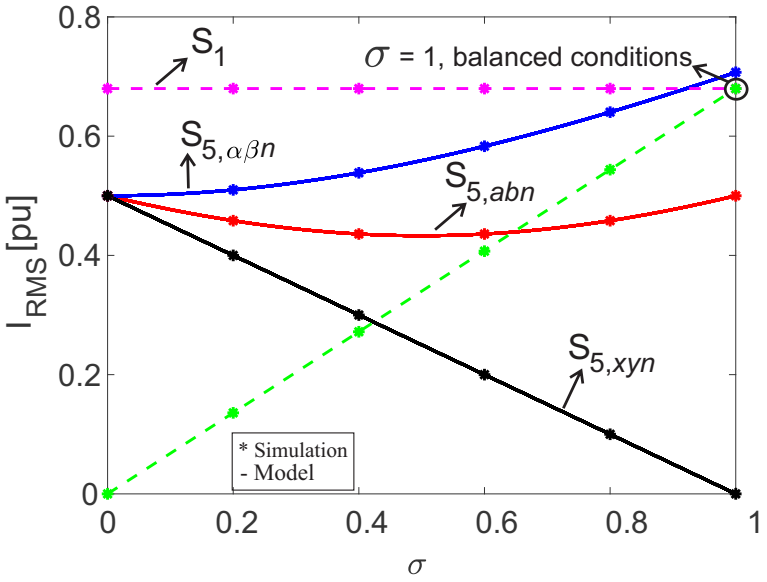

Figure 32 – RMS current through the IGBTs for different unbalanced factor. *Remark*: The RMS current in the phase legs is the same for all the considered converters. The main differences are observed in the neutral leg devices.

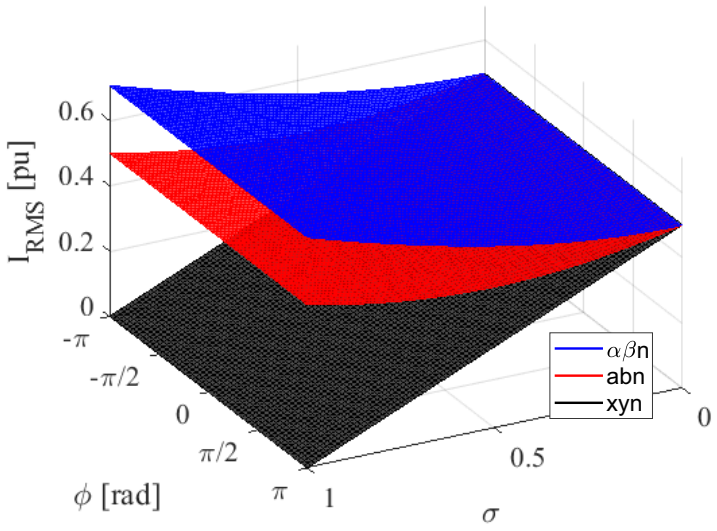

Figure 33 – RMS current through the active switches of the neutral leg (S_5 and S_6).

in each phase (i.e., $\phi_j \neq \phi_k$) on semiconductor current stress are investigated. Figure 34 illustrates the current stress for different values of angular displacement between voltage and current in the phases. It is evident that there are regions where each converter shows the highest stress. The values of the analytical equations were compared with simulations conducted in PLECS for several operating points, as shown in Figure 34. The maximum error obtained between the simulation and the equations is 0.1%.

Figure 35 provides more detailed results obtained in simulations using PLECS for different operating points. It is observed that in most of the operating points, the $\alpha\beta n$-GFC and *xyn*-GFC exhibit higher stress. Only at brief ϕ_k values is it possible to notice a higher stress in the *abn*-GFC.

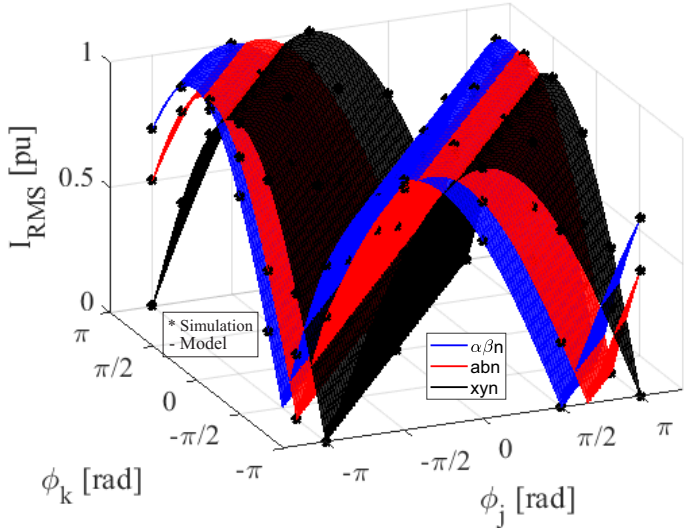

Figure 34 – RMS current through the active switches of the neutral leg (S_5 and S_6) considering I_j=I_k, and $\phi_j \neq \phi_k$.

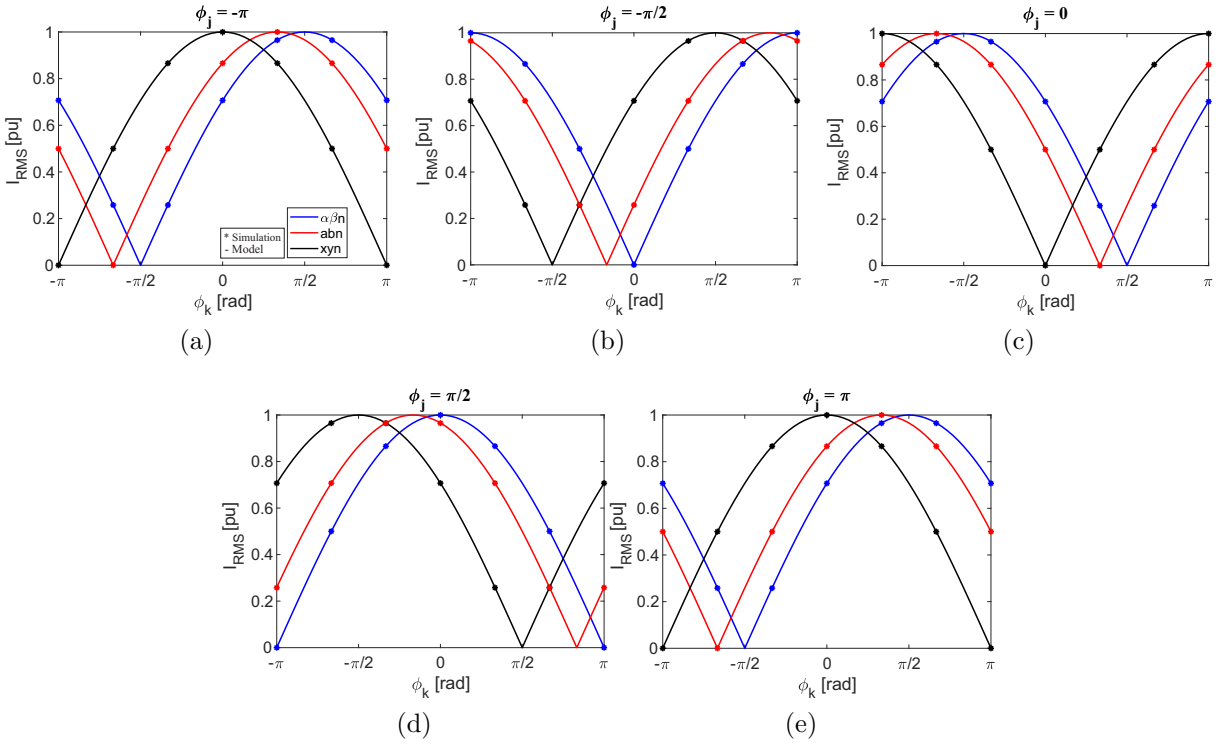

Figure 35 – RMS current through the active switches of the neutral leg (S_5 and S_6) considering I_j=I_k = 1, for different ϕ_k and: (a) $\phi_j = -\pi$, (b) $\phi_j = -\frac{\pi}{2}$, (c) $\phi_j = 0$, (d) $\phi_j = \frac{\pi}{2}$, (e) $\phi_j = \pi$.

Figure 36 provides a top view of Figure 34, considering only the angular displacement values of each phase. This result shows that all three converters have regions where they are the most stressed. It should be noted that the *abn*-converter exhibits smaller stressed regions compared to the other converters.

Following the Brazilian Regulatory Energy Agency (ANEEL), responsible for

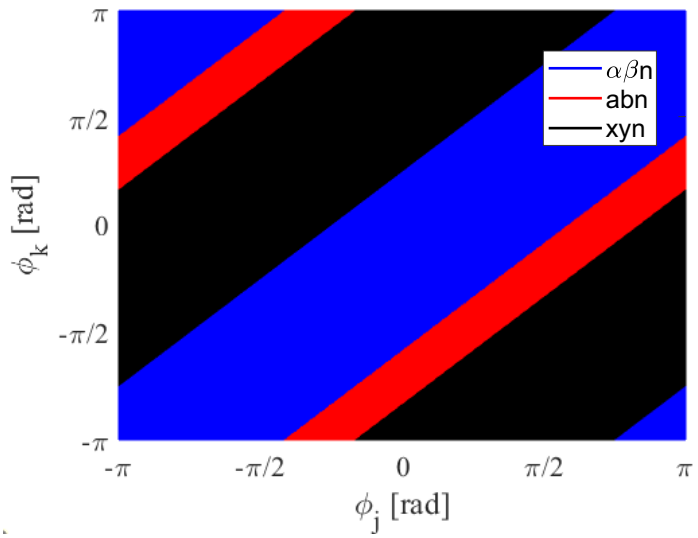

Figure 36 – Top view of the RMS current through the active switches of the neutral leg (S_5 and S_6) considering I_j=I_k, and $\phi_j \neq \phi_k$.

standardizing all electricity consumption, the power factor value is limited to 0.92 for industrial consumers connected to the grid. These parameters do not apply to isolated systems but provide a good operating standard for loads. Considering that isolated areas typically have loads with a lower power factor (such as electric motors), the analysis focuses on current stress in regions where these loads typically operate. In this study, the angle displacement values between voltage and current representing power factors ranging from 0.8 to 1 (that is, -0.6435<ϕ< 0.6435 rad) were examined.

Figure 37 shows the top view of Figure 34, considering the angular displacement values corresponding to the angles at which loads in isolated systems operate. It is evident that within this load threshold, the blue region consistently dominates, meaning that for the majority of operating points considered in this analysis, the $\alpha\beta n$-GFC exhibits higher levels of current stress.

4.2 Proposed DC-link capacitors current stresses evaluation for general load condition

The RMS current of the capacitor is evaluated by adapting the methodology used in Pei, Kang and Chen (2015) and Gopalakrishnan, Das and Narayanan (2011) for three-phase inverters. The current i_{dc} (see Figure 11) is calculated based on the 2Φ3W converter output current and modulation signals. Again, the analytical model neglects the current ripple in the output of the converter.

The general reference signal to SPWM, shown in Figure 27, is expressed as:

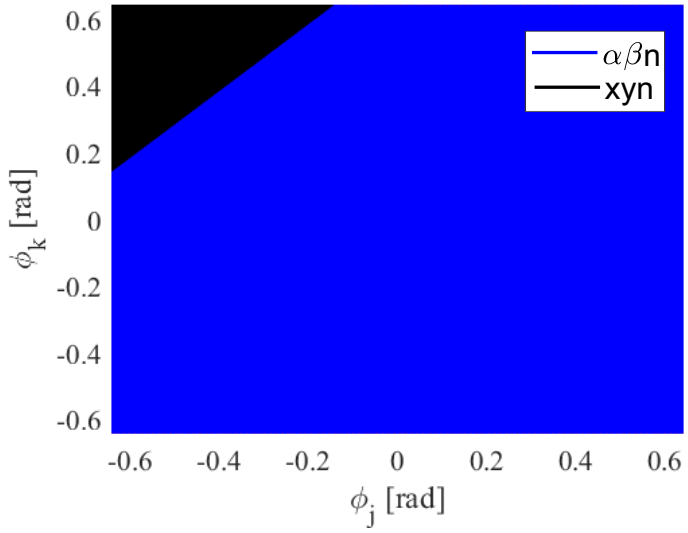

Figure 37 – Top view of the RMS current through the active switches of the neutral leg (S_5 and S_6) considering I_j=I_k, and -0.6435<ϕ<0.6435 rad.

$$\begin{cases} v_{jm}(t) = & M\sin(\omega t), \\ v_{km}(t) = & M\sin(\omega t+\theta), \\ v_{nm}(t) = & 0. \end{cases} \tag{4.51}$$

Comparing the bidirectional carrier signal v_{cr} with the three reference signals produces gate signals of S_1, S_3 and S_5, respectively, as shown in Figure 38. Figure 27 shows that half of the fundamental period can be divided into three intervals A-C. Figure 38 shows three detailed PWM waveforms for the high side switches over one carrier period during the intervals A-C. Note that when the switching frequency is high enough, the value of the reference signal during one carrier period can be assumed constant. According to the modulation waveforms, the intervals T_0, T_1, T_2, and T_3 can be solved for regions A-C, respectively, as:

$$\begin{cases} T_{0A} = & \frac{T_s}{4}(1-v_{km}) \\ T_{1A} = & \frac{T_s}{4}M(v_{km}-v_{jm}) \\ T_{2A} = & \frac{T_s}{4}M(v_{jm}-v_{nm}) \\ T_{3A} = & \frac{T_s}{4}M(1+v_{nm}) \end{cases} \tag{4.52}$$

$$\begin{cases} T_{0B} = & \frac{T_s}{4}(1-v_{jm}) \\ T_{1B} = & \frac{T_s}{4}M(v_{jm}-v_{km}) \\ T_{2B} = & \frac{T_s}{4}M(v_{km}-v_{nm}) \\ T_{3B} = & \frac{T_s}{4}M(1+v_{nm}) \end{cases} \tag{4.53}$$

$$\begin{cases} T_{0C} = & \frac{T_s}{4}\left(1 - v_{jm}\right) \\ T_{1C} = & \frac{T_s}{4} M \left(v_{jm} - v_{nm}\right) \\ T_{2C} = & \frac{T_s}{4} M \left(v_{nm} - v_{km}\right) \\ T_{3C} = & \frac{T_s}{4} M \left(1 + v_{km}\right) \end{cases} \tag{4.54}$$

where T_s is the switching period.

The DC-link current i_{dc} is obtained for each region respectively as:

$$\begin{cases} 0 & t_0 \leq t \leq t_1 \\ i_k & t_1 \leq t \leq t_2 \\ i_k + i_j & t_2 \leq t \leq t_3 \\ 0 & t_3 \leq t \leq t_5 \\ i_k + i_j & t_5 \leq t \leq t_6 \\ i_k & t_6 \leq t \leq t_7 \\ 0 & t_7 \leq t \leq t_8 \end{cases} \tag{4.55}$$

$$\begin{cases} 0 & t_0 \leq t \leq t_1 \\ i_j & t_1 \leq t \leq t_2 \\ i_j + i_k & t_2 \leq t \leq t_3 \\ 0 & t_3 \leq t \leq t_5 \\ i_j + i_k & t_5 \leq t \leq t_6 \\ i_j & t_6 \leq t \leq t_7 \\ 0 & t_7 \leq t \leq t_8 \end{cases} \tag{4.56}$$

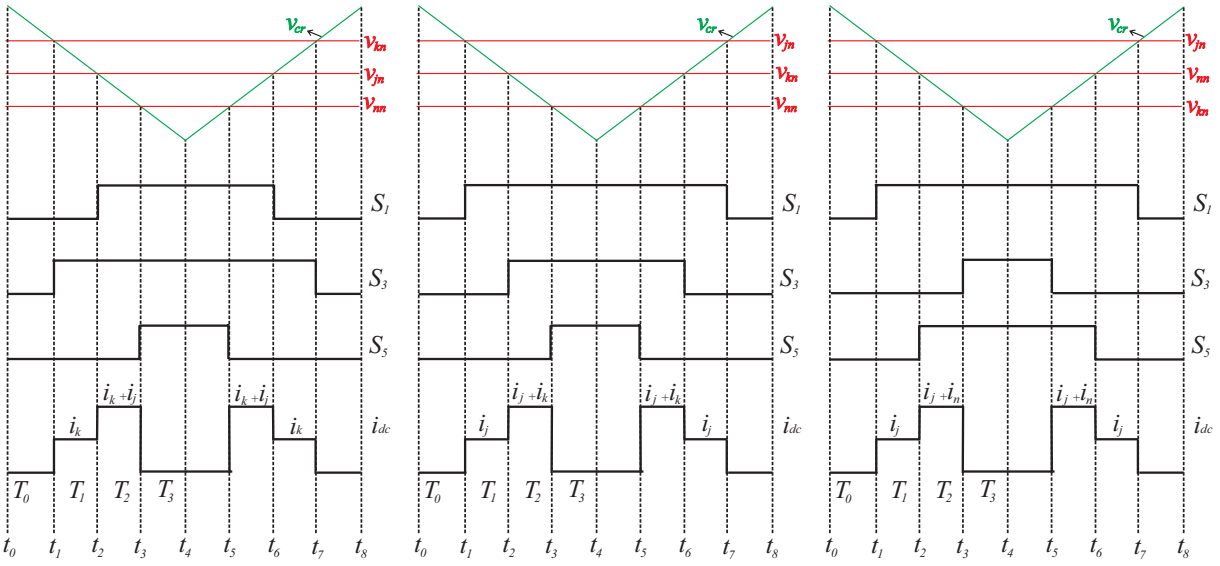

Figure 38 – Detailed PWM signals over one switching period:(a) region A. (b) region B. (c) region C.

$$\begin{cases} 0 & t_0 \leq t \leq t_1 \\ i_j & t_1 \leq t \leq t_2 \\ i_j + i_n & t_2 \leq t \leq t_3 \\ 0 & t_3 \leq t \leq t_5 \\ i_j + i_n & t_5 \leq t \leq t_6 \\ i_j & t_6 \leq t \leq t_7 \\ 0 & t_7 \leq t \leq t_8 \end{cases} \tag{4.57}$$

The average value of the DC-link current over one carrier period is for each region:

$$i_{AVG,A}(t) = \frac{1}{T_s}\int_{t_0}^{t_8} i_{dc}dt = 2\frac{T_{1A}}{T_s}i_k + 2\frac{T_{2A}}{T_s}(i_k + i_j), \tag{4.58}$$

$$i_{AVG,B}(t) = 2\frac{T_{1B}}{T_s}i_j + 2\frac{T_{2B}}{T_s}(i_j + i_k), \tag{4.59}$$

$$i_{AVG,C}(t) = 2\frac{T_{1C}}{T_s}i_j + 2\frac{T_{2C}}{T_s}(i_j + i_n). \tag{4.60}$$

The average DC-link current in each region is:

$$I_{AVG,A} = \frac{1}{\tau_A - \tau_0}\int_{\tau_0}^{\tau_A} i_{AVG,A}d\omega t = \frac{1}{\tau_A - \tau_0}\int_{\tau_0}^{\tau_A} 2\frac{T_{1A}}{T_s}i_k + 2\frac{T_{2A}}{T_s}(i_k + i_j)d\omega t, \tag{4.61}$$

$$I_{AVG,B} = \frac{1}{\tau_B - \tau_A}\int_{\tau_A}^{\tau_B} 2\frac{T_{1B}}{T_s}i_j + 2\frac{T_{2B}}{T_s}(i_j + i_k)d\omega t, \tag{4.62}$$

$$I_{AVG,C} = \frac{1}{\tau_C - \tau_B}\int_{\tau_B}^{\tau_C} 2\frac{T_{1C}}{T_s}i_j + 2\frac{T_{2C}}{T_s}(i_j + i_n)d\omega t, \tag{4.63}$$

where τ_0, τ_A, τ_B, and τ_C are the angle of the border of each region defined over half modulation signal period. Thus, the total average DC-link current is the weighted mean given by:

$$I_{dc,AVG} = \frac{\zeta_A I_{AVG,A} + \zeta_B I_{AVG,B} + \zeta_C I_{AVG,C}}{\zeta_A + \zeta_B + \zeta_C}, \tag{4.64}$$

where ζ_A, ζ_B, and ζ_C represent the percentage of regions A, B, and C respectively, in relation to the total region used for the calculation (π rad).

For the same time intervals, the DC-link RMS current over one carried period is computed as:

$$i^2_{RMS,A}(t) = \frac{1}{T_s}\int_{t_0}^{t_8} i^2_{dc}dt = 2\frac{T_{1A}}{T_s}i_k^2 + 2\frac{T_{2A}}{T_s}(i_k + i_j)^2, \tag{4.65}$$

$$i^2_{RMS,B}(t) = 2\frac{T_{1B}}{T_s}i_j^2 + 2\frac{T_{2B}}{T_s}(i_j + i_k)^2, \tag{4.66}$$

$$i^2_{RMS,C}(t) = 2\frac{T_{1C}}{T_s}i_j^2 + 2\frac{T_{2C}}{T_s}(i_j + i_n)^2. \tag{4.67}$$

The RMS DC-link current in each region is:

$$I^2_{RMS,A} = \frac{1}{\tau_A - \tau_0}\int_{\tau_0}^{\tau_A} i^2_{RMS,A}d\omega t = \frac{1}{\tau_A - \tau_0}\int_{\tau_0}^{\tau_A} 2\frac{T_{1A}}{T_s}i_k^2 + 2\frac{T_{2A}}{T_s}(i_k + i_j)^2 d\omega t, \tag{4.68}$$

$$I^2_{RMS,B} = \frac{1}{\tau_B - \tau_A}\int_{\tau_A}^{\tau_B} 2\frac{T_{1B}}{T_s}i_j^2 + 2\frac{T_{2B}}{T_s}(i_j + i_k)^2 d\omega t, \tag{4.69}$$

$$I^2_{RMS,C} = \frac{1}{\tau_C - \tau_B}\int_{\tau_B}^{\tau_C} 2\frac{T_{1C}}{T_s}i_j^2 + 2\frac{T_{2C}}{T_s}(i_j + i_n)^2 d\omega t. \tag{4.70}$$

Thus, the total RMS DC-link current is the weighted mean given by:

$$I^2_{dc,RMS} = \frac{\zeta_A I^2_{RMS,A} + \zeta_B I^2_{RMS,B} + \zeta_C I^2_{RMS,C}}{\zeta_A + \zeta_B + \zeta_C}. \tag{4.71}$$

As observed in Figure 11, the capacitor current is:

$$i_{cap} = i_{dc} - i_s, \tag{4.72}$$

where i_s is the output current of the BESS.

Assuming that all current ripple in i_{dc} is absorbed by the DC-link capacitor, i_s is equal to the average value of i_{dc}. Then, under such a condition, the RMS value of the capacitor current is:

$$I_{RMS,cap} = \sqrt{I^2_{dc,RMS} - I^2_{dc,AVG}}. \tag{4.73}$$

4.2.1 $\alpha\beta n$ DC-link capacitors current stress evaluation

For the DC-link capacitors current stress evaluation of the $\alpha\beta n$-converter, the regions A-C are limited with the borders:

$$\begin{cases} \tau_0 = & 0, \\ \tau_A = & \pi/4, \\ \tau_B = & \pi/2, \\ \tau_C = & \pi. \end{cases} \tag{4.74}$$

With the limited region, it is possible to define the weight of each region to be used in the calculation of the average and RMS currents. So the values for the $\alpha\beta n$-converter is:

$$\begin{cases} \zeta_A = & 1/4, \\ \zeta_B = & 1/4, \\ \zeta_C = & 1/2. \end{cases} \tag{4.75}$$

Thus, the average and RMS DC-link current on the $\alpha\beta n$-converter calculated by the equations (4.64) and (4.71) are:

$$I_{dc,AVG,\alpha\beta n} = I_j M \frac{\cos\phi_j}{4} + I_k M \frac{\cos\phi_k}{4}, \tag{4.76}$$

$$\begin{aligned} I^2_{dc,RMS,\alpha\beta n} = {} & I_j^2 M \tfrac{\cos 2\phi_j + 3}{6\pi} + I_k^2 M \tfrac{\cos 2\phi_k + 3}{6\pi} + I_j I_k M \tfrac{\sqrt{2}\cos(\phi_k + \phi_j)}{6\pi} \\ & + I_j I_k M \tfrac{(\sqrt{2}-2)\sin(\phi_k - \phi_j)}{2\pi}. \end{aligned} \tag{4.77}$$

Finally, the current stress of the capacitor is calculated by the equation (4.73).

4.2.2 *abn* DC-link capacitors current stress evaluation

For the DC-link capacitors current stress evaluation of the *abn*-converter, the regions A-C are limited with the borders and weights:

$$\begin{cases} \tau_0 = & 0, \\ \tau_A = & \pi/6, \\ \tau_B = & \pi/3, \\ \tau_C = & \pi. \end{cases} \tag{4.78}$$

$$\begin{cases} \zeta_A = & 1/6, \\ \zeta_B = & 1/6, \\ \zeta_C = & 2/3. \end{cases} \tag{4.79}$$

The average and RMS DC-link current on the *abn*-converter are:

$$I_{dc,AVG,abn} = I_j M \frac{\cos\phi}{4} + I_k M \frac{\cos\phi}{4} \tag{4.80}$$

$$\begin{aligned} I^2_{dc,RMS,abn} = {} & I_j^2 M \tfrac{\cos 2\phi_j + 3}{6\pi} + I_k^2 M \tfrac{\cos 2\phi_k + 3}{6\pi} + I_j I_k M \tfrac{2(\sqrt{3}-1)\cos(\phi_k + \phi_j)}{12\pi} \\ & + I_j I_k M \tfrac{(9-6\sqrt{3})\sin(\phi_k - \phi_j)}{12\pi} + I_j I_k M \tfrac{(3\sqrt{3}-6)\cos(\phi_k - \phi_j)}{12\pi} \end{aligned} \tag{4.81}$$

The RMS current of the DC-link capacitor is shown in Table 6. The average DC-link current for the *abn*-converter is equal to the $\alpha\beta n$-converter.

4.2.3 *xyn* DC-link capacitors current stress evaluation

For the DC-link capacitors current stress evaluation of the *xyn*-converter, the modulation signals are shown in Figure 39. Thus, for this case is not necessary divide the half modulation signal period in three regions, and the average and RMS currents are calculated by equations (4.63) and (4.70):

$$I_{dc,AVG,xyn} = \frac{1}{\pi}\int_0^{\pi} 2\frac{T_1}{T_s} i_j + 2\frac{T_2}{T_s}(i_j + i_n) d\omega t, \tag{4.82}$$

$$I_{dc,AVG,xyn} = I_j M \frac{\cos\phi_k}{4} + I_k M \frac{\cos\phi_k}{4} \tag{4.83}$$

$$I^2_{dc,RMS,xyn} = \frac{1}{\pi}\int_0^{\pi} 2\frac{T_1}{T_s} i_j^2 + 2\frac{T_2}{T_s}(i_j + i_n)^2 d\omega t. \tag{4.84}$$

$$I^2_{dc,RMS,xyn} = I_j^2 M \frac{\cos 2\phi_j + 3}{6\pi} + I_k^2 M \frac{\cos 2\phi_k + 3}{6\pi}. \tag{4.85}$$

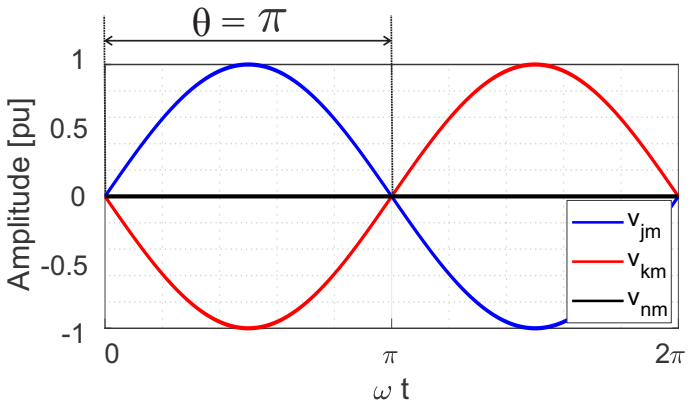

Figure 39 – 2Φ3W reference signals for *xyn*-converter.

Note that the average current remains the same for all converters considered in this dissertation. The RMS current differs among the converters, now each phase current is responsible for a portion of the RMS current, and the component that had the product of the phase currents disappears in the *xyn*-converter. For the 2Φ3W converters investigated in this dissertation, the RMS currents of the DC-link capacitor are shown in Table 6.

4.2.4 Balanced load conditions - capacitor

Figure 40 shows the RMS current in the DC-link capacitor for different modulation indexes and displacement angles. In this result, the authors assume that the converter maintains a current flow of 1 pu through the phase switches, and supplies loads with different power factors. The results are compared with simulations in PLECS. The following conclusions are stated:

- When the converter operates with the unity power factor ($\phi = 0$), the *xyn*-converter has the lowest RMS value of the capacitor current, despite presenting the highest second order harmonic current. This result highlights the effect of the high-frequency components in the capacitor current stress and therefore in the wear-out analysis.
- For the $\alpha\beta n$-converter, regardless of the power factor, the current in the capacitor is higher for the modulation index $M = 1$. For the *abn* and *xyn* converters, the behavior is different, since the capacitor RMS current is quite affected by the power factor and modulation index.

Table 6 – Analytical expressions of current stress of the DC-link capacitor for 2Φ3W GFCs.

System	$I_{RMS,cap}$
$\alpha\beta n$	$\sqrt{I_j^2 M \frac{\cos 2\phi_j+3}{6\pi} + I_k^2 M \frac{\cos 2\phi_k+3}{6\pi} + I_j I_k M \frac{\sqrt{2}\cos(\phi_k+\phi_j)}{6\pi} + I_j I_k M \frac{(\sqrt{2}-2)\sin(\phi_k-\phi_j)}{2\pi} - \frac{I_j^2 M^2 \cos^2(\phi_j)}{16} - \frac{I_k^2 M^2 \cos^2(\phi_k)}{16}}$
abn	$\sqrt{I_j^2 M \frac{\cos 2\phi_j+3}{6\pi} + I_k^2 M \frac{\cos 2\phi_k+3}{6\pi} + I_j I_k M \frac{2(\sqrt{3}-1)\cos(\phi_k+\phi_j)}{12\pi} + I_j I_k M \frac{(9-6\sqrt{3})\sin(\phi_k-\phi_j)}{12\pi} + I_j I_k M \frac{(3\sqrt{3}-6)\cos(\phi_k-\phi_j)}{12\pi} - \frac{I_j^2 M^2 \cos^2(\phi_j)}{16} - \frac{I_k^2 M^2 \cos^2(\phi_k)}{16}}$
xyn	$\sqrt{M I_a^2 \frac{\cos(2\phi_j)+3}{6\pi} + M I_b^2 \frac{\cos(2\phi_k)+3}{6\pi} - \frac{I_j^2 M^2 \cos^2(\phi_j)}{16} - \frac{I_j^2 M^2 \cos^2(\phi_k)}{16}}$

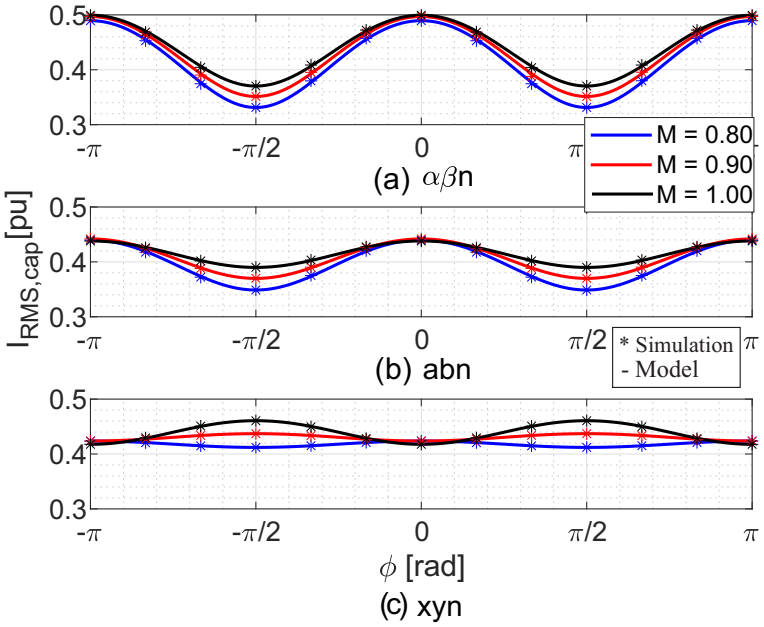

Figure 40 – RMS current of the DC-link capacitor: (a) $\alpha\beta n$; (b) *abn* and (c) *xyn*.

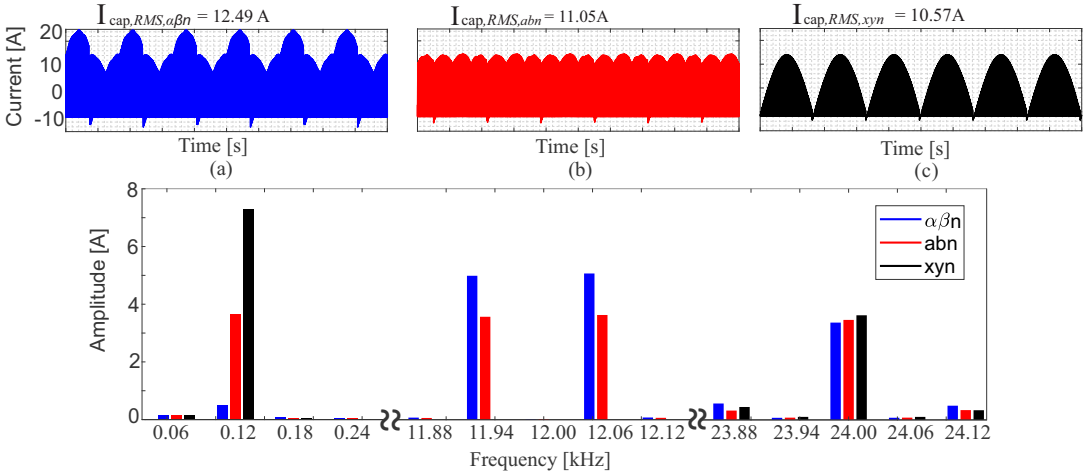

Figure 41 – Capacitor current of PLECS simulation: (a) $\alpha\beta n$-system. (b) *abn*-system. (c) *xyn*-system. (d) Capacitors current harmonic spectrum.

- The maximum error observed between the model and the simulated results is 2.1%.

The lower RMS current values for the *xyn*-converter is further investigated through simulations implemented in PLECS. Figure 41(a)-(c) show the capacitor current waveform for $\alpha\beta n$, *abn* and *xyn*-converters, respectively. Figure 41(d) compares the capacitor current harmonic spectrum for the investigated converters. The *xyn*-converter shows the highest second harmonic component value, while this component is approximately zero for the $\alpha\beta n$-converter. On the other hand, the *xyn*-converter has no harmonic component around the switching frequency, similarly to traditional full-bridge inverters with unipolar modulation. It contributes to reduce the RMS current through the DC-link capacitor.

4.2.5 Unbalanced load conditions - capacitor

4.2.5.1 Effect of current amplitude unbalance ($I_j \neq I_k$, $\phi_j = \phi_k$)

The behavior of current stress in DC-link capacitor is analyzed when the system experiences an unbalance in current amplitude, and the phase currents exhibit the same angular displacement in relation to the phase voltages (i.e., $\phi_j = \phi_k = \phi$). Figure 42 shows the currents through the DC-link capacitor under current unbalance in the phase legs of the 2Φ3W converter, considering $\phi_j = \phi_k = \phi = 0$ and $I_j = 1$. The RMS values of the current stress, obtained using Table 6, are plotted in per unit (pu) values of the rated current. Regardless of the value of the unbalance factor, the RMS current through the DC-link capacitor is always lower in the *xyn*-GFC than in the other two converters, leading to lower loss. The $\alpha\beta n$-GFC shows the highest loss value, regardless of the current unbalance between the phases.

Some operating points for different imbalance factors were simulated in PLECS to validate the model, and the values are shown in Figure 42. The maximum error obtained between the simulation and the model was 1.1%.

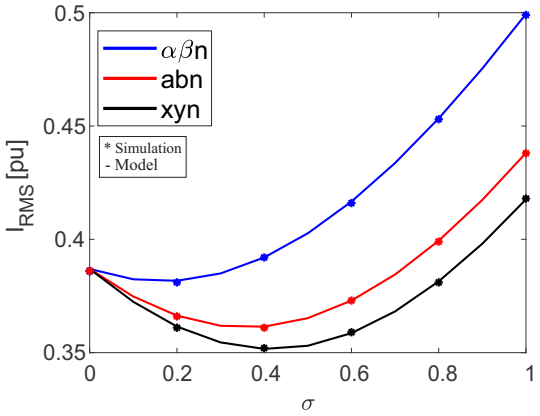

Figure 42 – RMS current through the DC-link capacitor for different unbalanced factor.

Figure 43(a) shows the effect of current amplitude unbalance on DC-link capacitor for each converter for a different angle displacement between voltage and current, and $I_j = 1$. The angle displacement has a significant impact on the current stress of the converter. There are different regions where the $\alpha\beta n$ and *xyn* converters are always the most stressed, as shown in Figure 43(b). The dashed line marks the operating region between -0.6435 $< \phi <$ 0.6435 rad, which limits the power factor between 0.8 and 1. In this operating region, the most stressed converter is the $\alpha\beta n$-GFC regardless of the unbalanced current amplitude.

4.2.5.2 Effect of different angle displacements (I_j=I_k, $\phi_j \neq \phi_k$)

For this analysis, identical current amplitudes in phases are considered (I_j=I_k=1 pu), and the effects of different angular displacements between voltage and current in

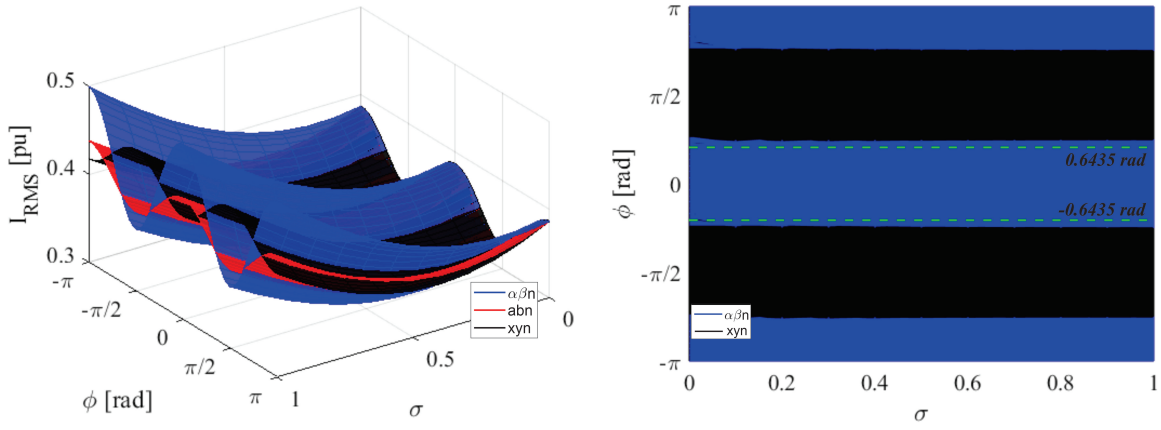

(a) (b)

Figure 43 – (a) RMS current through the DC-link capacitor for different unbalance factor and different displacement angle. (b) Top view of RMS current through the DC-link capacitor.

each phase (i.e., $\phi_j \neq \phi_k$) on DC-link capacitor current stress are investigated. Figure 44 illustrates the current stress for different values of angular displacement between voltage and current in the phases. The equations in Table 6 indicate a complex relationship between current stress and phase unbalance. It is noticeable that, depending on the region, each converter operates under higher stress than the others.

Figure 45 provides a top view of Figure 44(d), considering only the angular displacement values of each phase. It is evident that the *abn*-GFC has the smallest dominant current stress area. The other two converters exhibit areas where current stress dominates. It is expected that the *xyn*-GFC has higher stress, as it shows the largest second harmonic oscillation in the DC bus voltage. However, it is observed that the $\alpha\beta n$-GFC also has a significant area where it is the most stressed, indicating that higher-order harmonic currents also strongly influence the capacitor current stress, which consequently impacts thermal stress.

Figure 46 provides more detailed results of the current stress of the DC-link capacitor obtained in simulations using PLECS for different operating points. Similarly to semiconductors, it is observed that in most operating points, the $\alpha\beta n$-GFC and *xyn*-GFC exhibit higher stress. Only at brief ϕ_k values is it possible to notice a higher stress in the *abn*-GFC. The maximum error observed between the simulation and the model is 1.2%.

4.3 Chapter closure

In this chapter, equations were obtained to analyze the current stress in semiconductors and capacitors of 2Φ3W converters. With respect to the semiconductors, the difference in current stress occurs in the semiconductors of the neutral leg of the

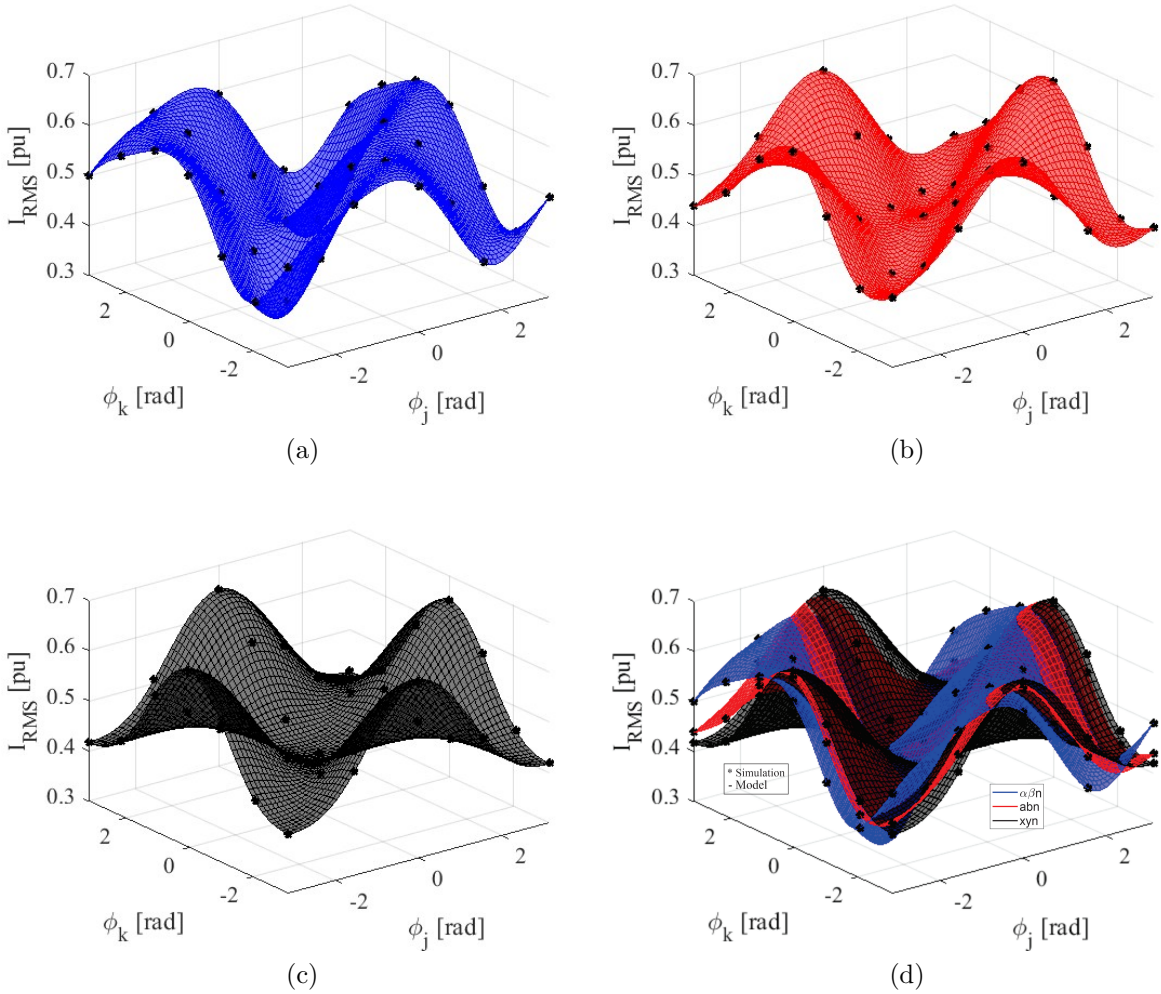

Figure 44 – RMS current in DC-link capacitor under unbalanced conditions of: (a) $\alpha\beta n$-GFC. (b) *abn*-GFC. (c) *xyn*-GFC. (d) Three GFCs types. *Remark*: The dots are the simulated points in PLECS.

converter. The equations show that, under balanced load conditions, the $\alpha\beta n$-GFC shows a higher current stress than the other two converters. Under unbalance conditions, both the $\alpha\beta n$ and *xyn* converters have larger operating regions where they are the most stressed compared to the *abn*-GFC.

From the capacitor perspective, the $\alpha\beta n$ and *xyn* converters also have more operating points where they experience higher current stress, under balanced and unbalanced load conditions. These results help to understand the reliability and thermal stress results presented in the next chapter.

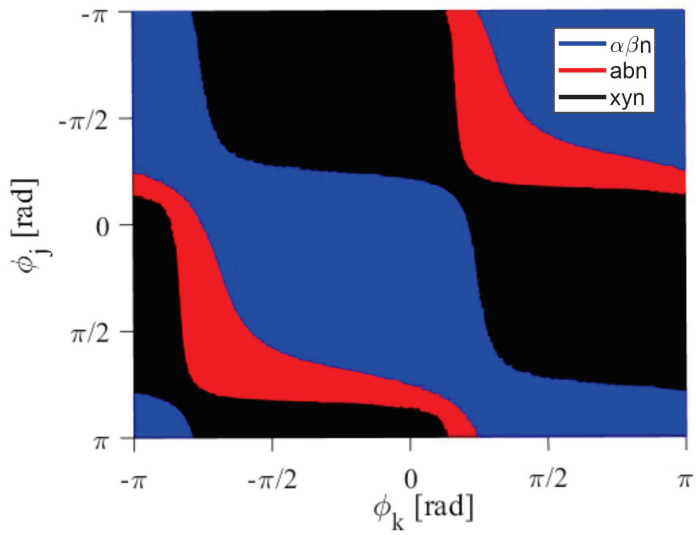

Figure 45 – Top view of the RMS current through the DC-link capacitor for different angle displacement.

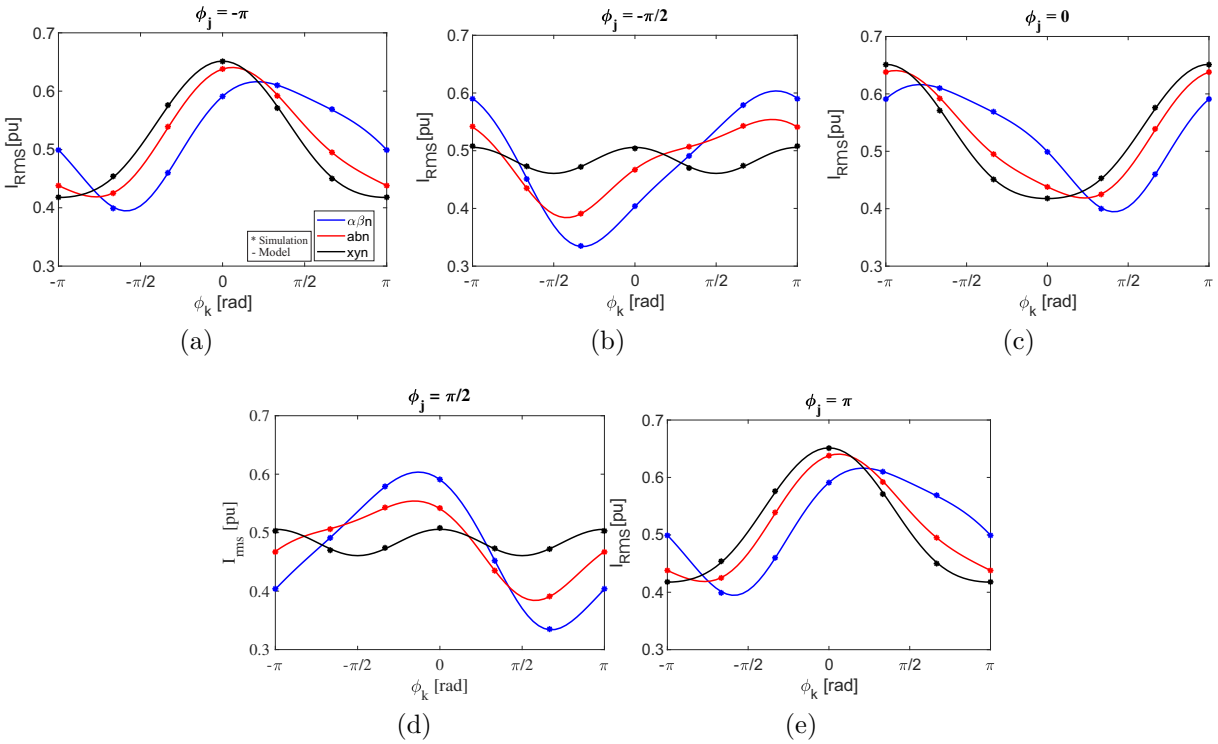

Figure 46 – RMS current through the DC-link capacitor considering I_j=$I_k = 1$, for different ϕ_k and: (a) $\phi_j = -\pi$, (b) $\phi_j = -\frac{\pi}{2}$, (c) $\phi_j = 0$, (d) $\phi_j = \frac{\pi}{2}$, (e) $\phi_j = \pi$.

5 Simulation and Experimental Results

In this chapter, the results are presented in two parts: one showing simulations and experimental outcomes for the discrete IGBTs setup and a second part demonstrating simulations and experimental results for the open semiconductor module setup.

5.1 Discrete IGBTs setup results

5.1.1 HIL and experimental results

These results validate the capacitor current, considering the use of analog-to-digital conversion and digital implementation issues for comparison with the proposed analytical model. The experimental setup developed is shown in Figure 47. Figures 48 (a)-(c) show the GFC current per phase and the DC-link current for the three converters.

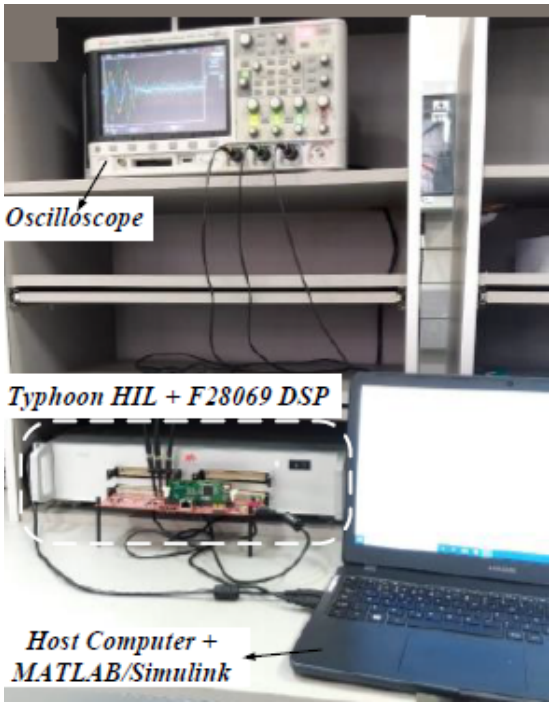

Figure 47 – Setup used for HIL results.

The prototype does not allow for direct measurement of the current passing through the capacitor. Figure 49 shows the schematic that illustrates where the current measurements were taken in the experiment. Therefore, the current was measured at the output of the voltage source on the oscilloscope with AC coupling. In practice, this means the output current minus the average output current, which theoretically represents the current drawn by the capacitor. Figures 50 (a)-(c) show the GFC current per phase and

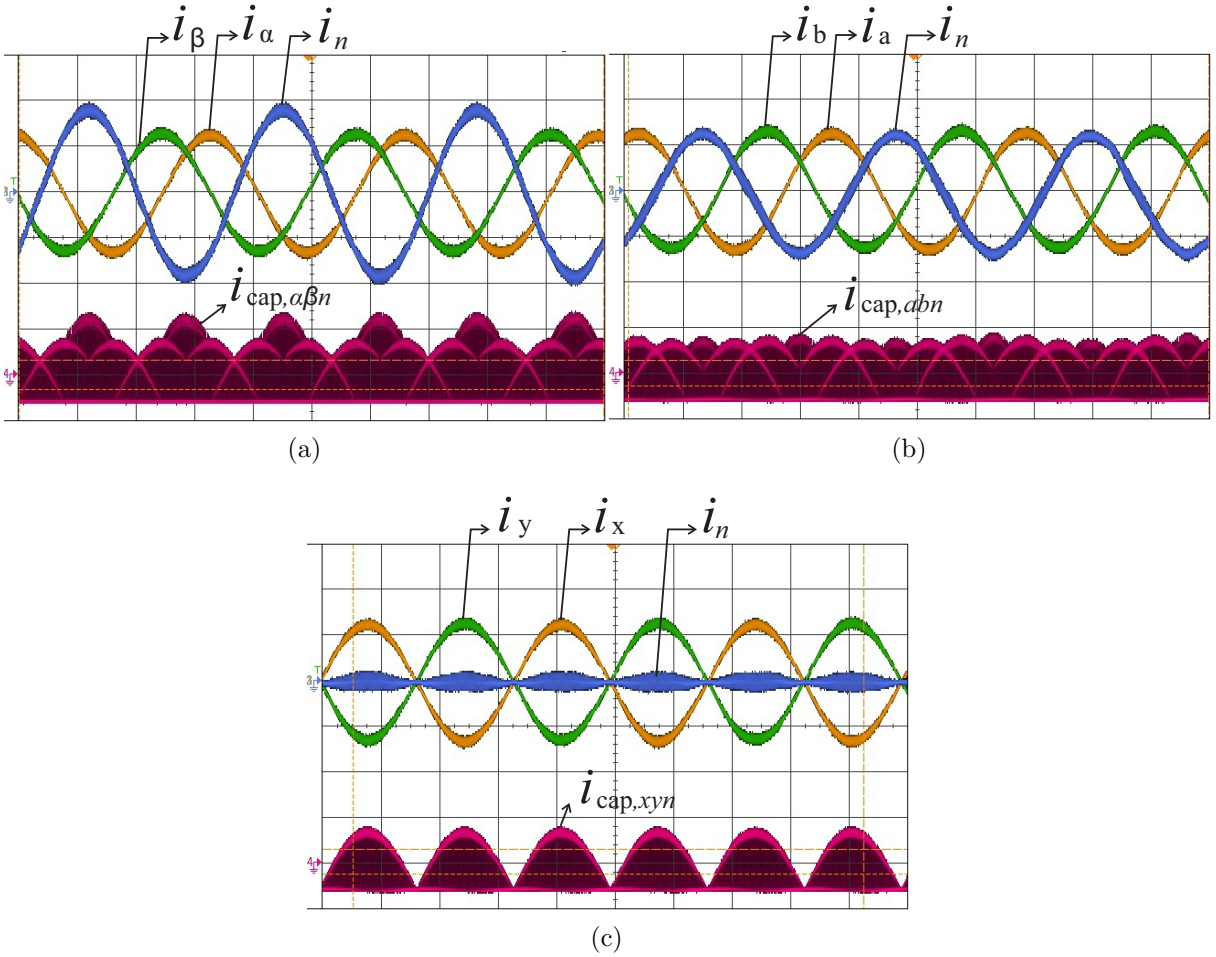

Figure 48 – Results in hardware-in-the-loop. Phase current and capacitor current of: (a) $\alpha\beta n$-GFC. (b) abn-GFC. (c) xyn-GFC.

the DC-link current ripple obtained in the experimental test. The current ripple behaves similarly to the HIL currents shown in Figure 48. The slight differences are due to the rating difference between the prototypes.

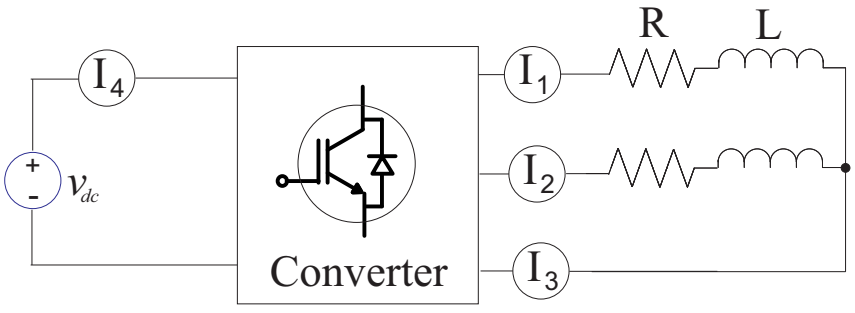

Figure 49 – Current measurements in the experimental results in the discrete IGBT setup.

To ensure a fairer comparison, an additional simulation was conducted in PLECS with the converter operating in open loop, using load and voltage values on the DC bus which are closely to those employed in the experimental setup. This simulation was designed to align the operating conditions between the experiment and the simulation, providing a more equitable basis for comparison. Figure 51 illustrates the current harmonic

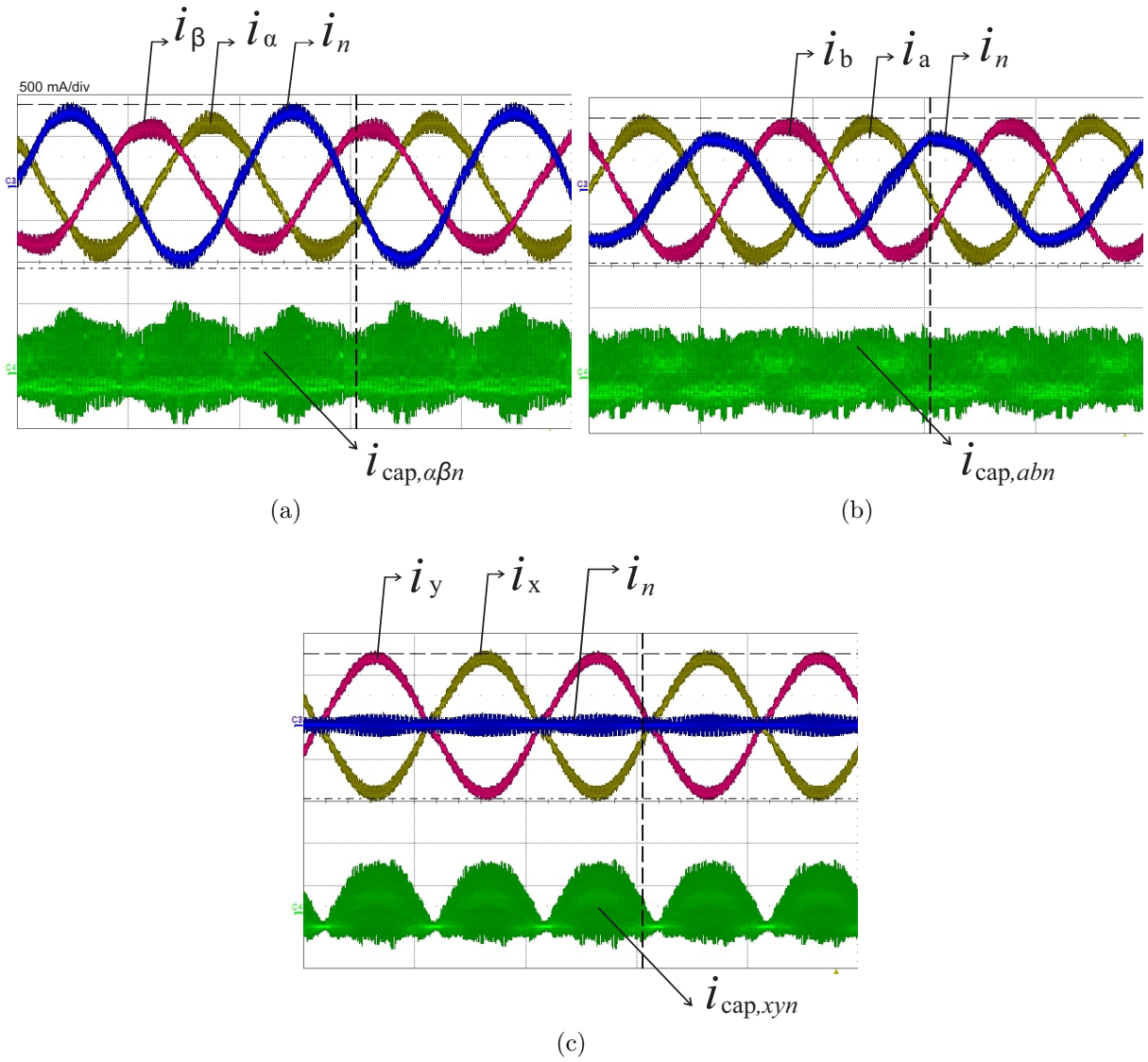

Figure 50 – Experimental results in reduced-scale prototype. Phase current and DC-link ripple current of: (a) $\alpha\beta n$-GFC. (b) abn-GFC. (c) xyn-GFC.

spectrum in the DC-link capacitor, comparing the measured values obtained from the experiment with the values obtained from the simulation, both under open-loop operation. Notably, the harmonic spectrum exhibits a similar behavior in both cases, demonstrating a strong correlation between the experimental and simulated results. Any minor discrepancies observed can be attributed to inherent non-linearities and inherent variability presented in experimental setups. These findings affirm the consistency and validity of the simulation, further supporting its reliability in accurately representing the harmonic characteristics of the system.

Notice that the $\alpha\beta n$-converter, although it does not show a second-order harmonic component, appears to visually exhibit this oscillation. A deeper investigation revealed that this visual effect is due solely to the summation of each harmonic component. Using FFT, the signal was reconstructed considering part of the spectrum, and it was found that this shape only occurs due to high-frequency components, indicating that visual analysis

without FFT of the signal can be misleading.

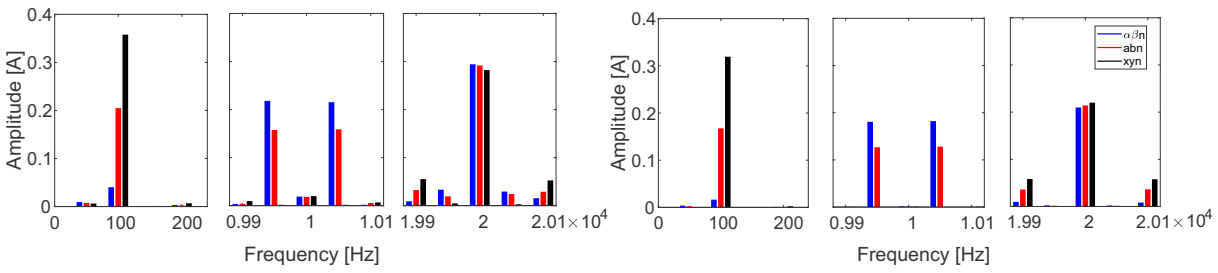

(a) (b)

Figure 51 – (a) Harmonic spectrum of the DC-link capacitor current obtained by means of the experimental test bench. (b) Harmonic spectrum of the DC-link capacitor current obtained by simulation o PLECS. *Both scenarios consider open loop operation.*

Table 7 shows the RMS values of the current in the DC-link capacitor under four different conditions: the value obtained in the simulation with closed loop, the value obtained in the HIL testing with closed loop, the value obtained in the simulation using PLECS in open loop, and the value obtained from the experiment conducted in open loop. An interesting observation is that among the four scenarios, the $\alpha\beta n$-converter exhibits the highest RMS value, while the *xyn*-converter shows the lowest value. These results indicate that, despite the higher low-frequency component in the *xyn*-converter, the overall RMS value of the capacitor current remains lower compared to the other two converters. Consequently, this difference in the RMS values has an impact on the losses, as converters with higher RMS values of the capacitor current tend to experience higher losses.

Table 7 – RMS DC-link capacitor current in PLECS simulations, HIL and experimental test bench.

Closed-loop converters			
	$\alpha\beta n$	***abn***	***xyn***
PLECS	12.49 A	11.05 A	10.57 A
HIL	12.69 A	11.11 A	10.67 A
Open-loop converters			
PLECS	431 mA	392 mA	384 mA
Experiment	519 mA	465 mA	410 mA

5.1.2 Wear-out Failure Probability

These results were obtained considering a mission profile found in EMC (2022) and shown in Figure 52, which does not take into account the characteristics of an isolated system in the Amazon region. These data are from Goiás, in the Brazilian Midwest. The thermal model adopted for losses considered the hybrid Cauer and Foster model. This

profile was chosen because it has been used in other studies and serves as a good case study for these initial results.

The junction temperature of IGBT S_1 is shown in Figure 53(a) and IGBT S_5 in Figure 53(b). The largest difference between the converters considered is found in IGBT S_5, where the neutral current circulates. For the $\alpha\beta n$-GFC, the current is higher than the phase current, increasing the temperature in this component and, consequently, the temperature of the phase leg. Since there is no current in the neutral in the *xyn*-converter, the temperature is lower than the other converters analyzed, greatly reducing the thermal stress. The hotspot temperature for one capacitor in the DC link is shown in Figure 53(c). It is noted that the temperatures present similar values for all grid configurations. The *xyn*-converter show the highest temperature, and the *abn*-converter the lowest temperature.

The histograms of annual damages for the components of the GFC are shown in Figure 54. This is a normalized histogram of the damage calculated by Monte Carlo. Normalized damage is the count of the classes divided by the total number of observations. The Monte Carlo simulation considers parametric variations, thus each simulated sample is expected to have a different annual damage value. Therefore, there is an annual damage distribution, where the sum of the histogram accounts for the sum of all 50,000 samples is equal to 1. The annual damage to IGBT S_1 is shown in Figure 54(a). Note that damage at

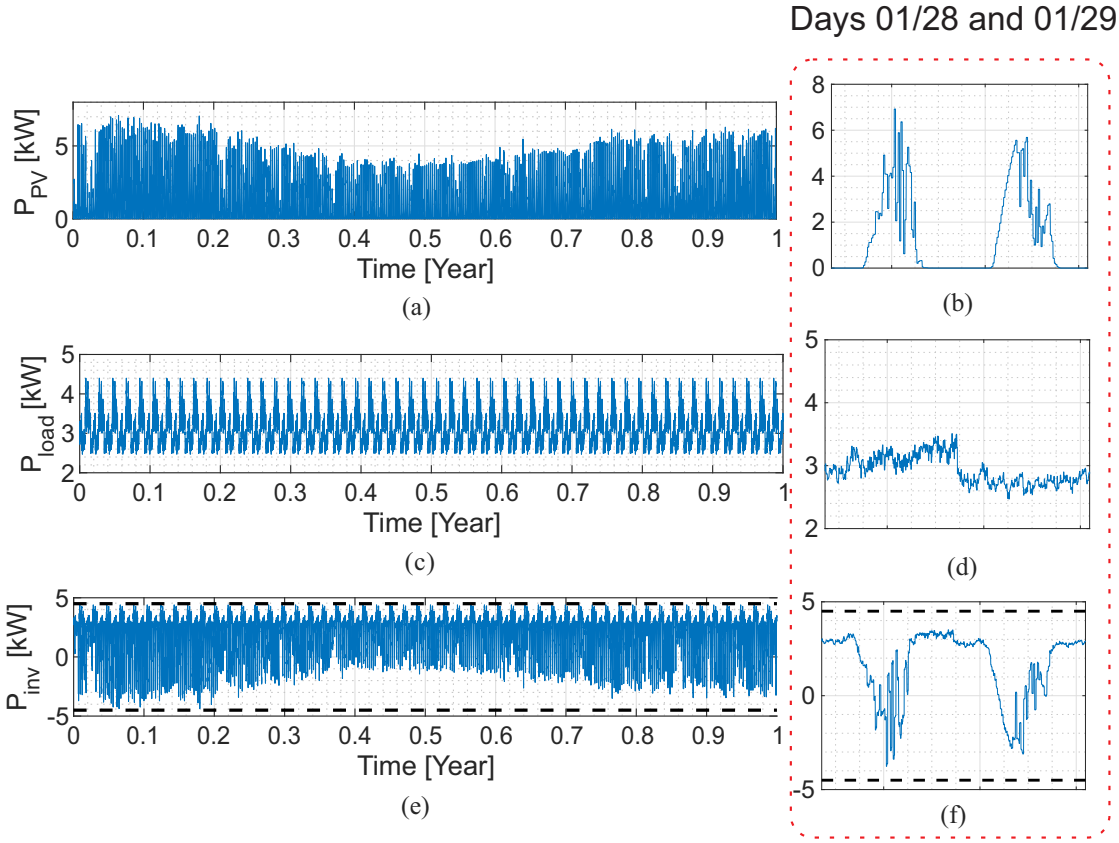

Figure 52 – Power profiles: (a) One year PV plant generation. (b) Two day PV plant generation. (c) One year load power. (d) Two day load power. (e) One year grid-forming inverter power. (f) Two day grid-forming inverter power.

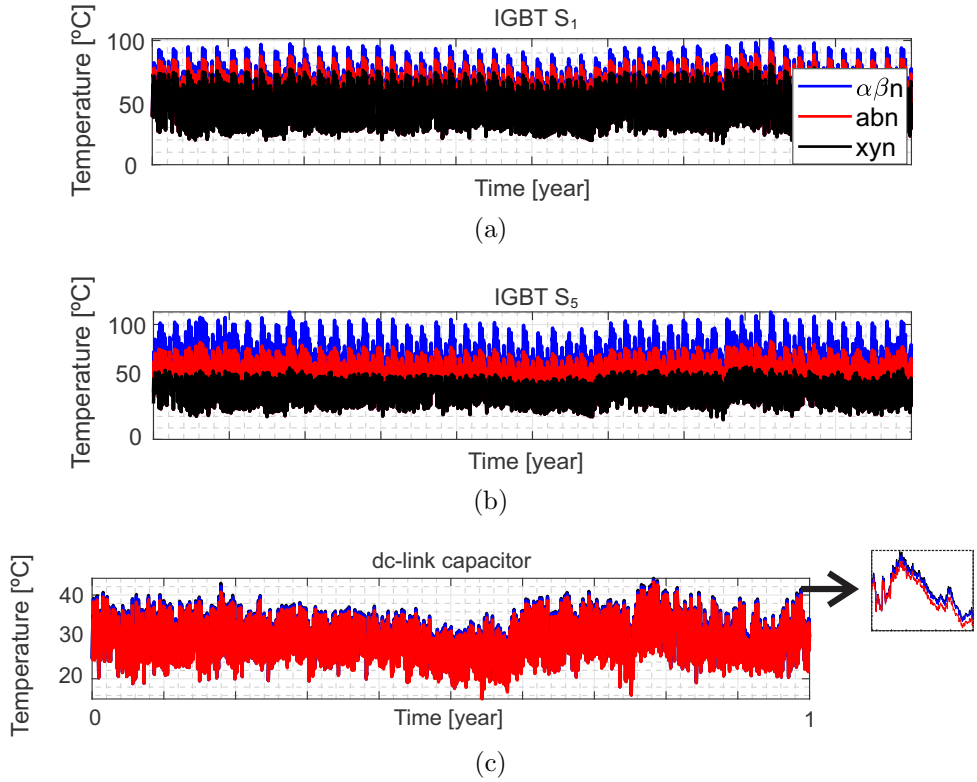

Figure 53 – Average junction temperature: (a) IGBT S_1. (b) IGBT S_5. (c) DC-link capacitor.

the same semiconductor differs among grid configurations, even though the RMS current is the same in the switches.

All semiconductors are mounted on the same heatsink, implying that the thermal impedance remains consistent throughout the converter. However, the loss look-up table for the IGBTs S_5-S_6 and diodes d_5-d_6 differs between the three converters analyzed in this study. Consequently, even under identical operational conditions, different temperatures are observed for the phase semiconductors. The thermal coupling between capacitors and semiconductors was not considered for simplicity. Furthermore, the extent of this coupling is strongly influenced by the arrangement of components within the converter. A more comprehensive analysis of this aspect is left for future research.

The $\alpha\beta n$-GFC has the largest annual damage distribution, indicating that the power component wears out faster than the other converters. The same behavior is observed for IGBT S_5, shown in Figure 54(b), where the difference in damage between semiconductors is even higher. The annual damage to the DC-link capacitor is shown in Figure 54(c). The annual damage distribution is similar for all grid configurations, and *abn*-GFC shows slightly less damage compared to the other ones.

The unreliability function of the semiconductors is shown in Figure 55(a). The results are affected by the difference in stress caused by the current flowing through the neutral leg. The *xyn*-GFC has the lowest wear-out failure probability, with a value in B_{10} equal to 35 years. In $\alpha\beta n$-GFC, the value in B_{10} is 5.7 years, which shows that the higher

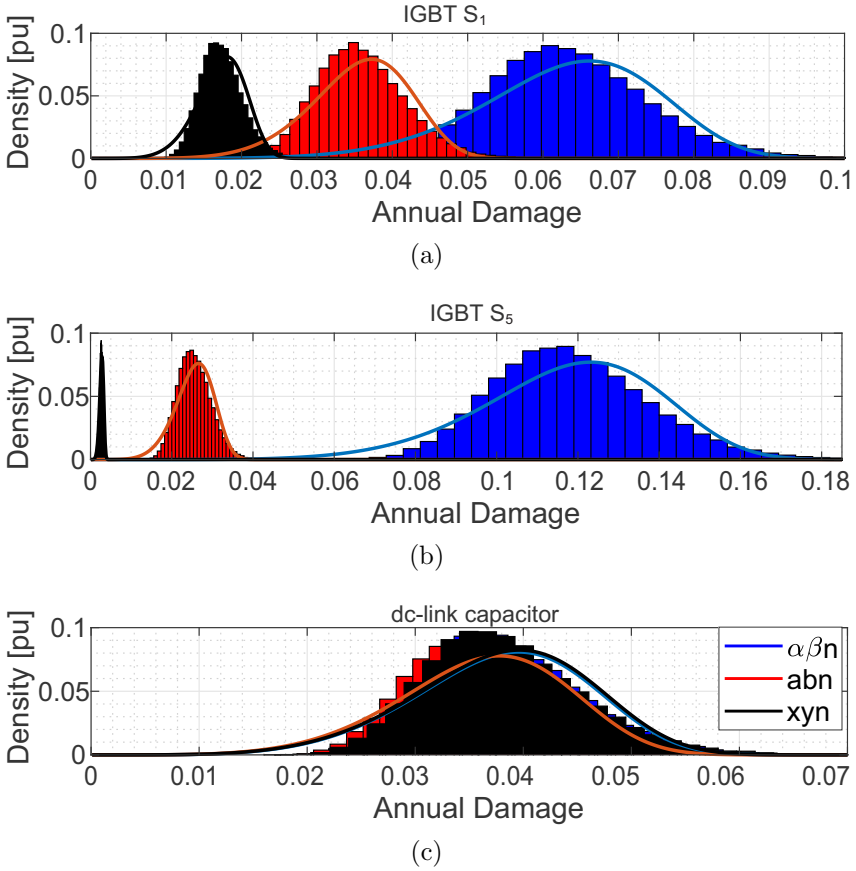

Figure 54 – Monte Carlo simulations of the components: (a) IGBT S_1. (b) IGBT S_5. (c) DC-link capacitor.

current value in these semiconductors increases the thermal stress.

The temperature difference and the annual damage distribution explain the probability of wear-out failure of the DC link capacitors shown in Figure 55(a). These results show that the high-frequency components in current affect the losses and consequently the lifetime of the capacitors. The $\alpha\beta n$-GFC displays in function B_{10} 21 years, even without low frequency oscillation in the DC-link voltage, which is related to the fact that high-frequency components affect losses. The *xyn*-GFC shows the lowest B_{10} (20.8 years), and the *abn*-GFC has the least probability of failure in the capacitors, the value in the function B_{10} is 21.9 years.

Finally, the unreliability function of the overall converter is shown in Figure 55(b). The high probability of failure for IGBTs in the $\alpha\beta n$-GFC leads to the converter level in B_{10} equal to the semiconductor level. Statistically, 10% of the samples considered fail at 5.7 years. The *xyn*-GFC shows the highest value in B_{10} (20.7 years), since the IGBTs devices are less likely to fail than the others, improving the probability of wear-out failure in 28. 11%, compared to the typical *abn*-GFC.

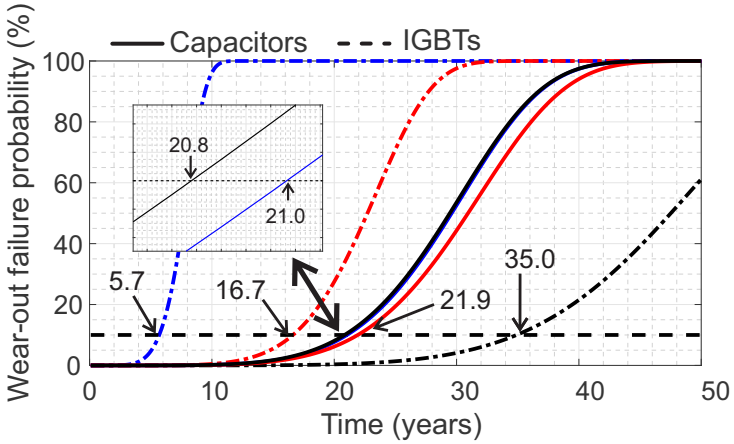

(a)

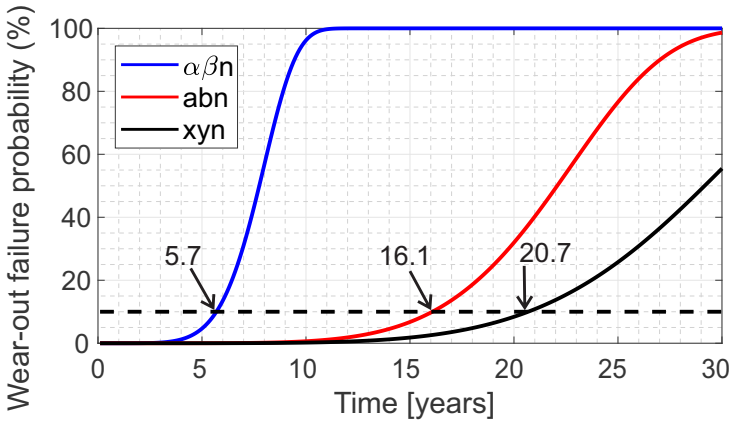

(b)

Figure 55 – (a) IGBTs and Capacitors unreliability functions. (b) Overall converter level unreliability functions.

5.1.2.1 Sensitivity analysis

Considering that the hardware is sized for the *abn*-GFC applications, the value found in B_{10} under nominal conditions is considered the benchmark. The first sensitivity analysis evaluates the impact of the power derating on the converter lifetime, considering the same hardware for all grid configurations, and varying the converter output power. It results in a cost per kilowatt (specific cost) given by:

$$K_{i,kw} = \frac{C_h}{P_n}, \tag{5.1}$$

where C_h is the hardware cost and P_n is the converter nominal power. In this analysis, the converter power was adjusted at various operating points. For each point, an unreliability analysis was performed, considering the entire system (semiconductors and capacitors). This approach allowed for a comprehensive assessment of the performance and reliability of the converter under different power conditions.

Reduce the output power of converter in the $\alpha\beta n$-GFC decreases the wear-out failure probability and the converter-level unreliability is affected as shown in Figure 56(a).

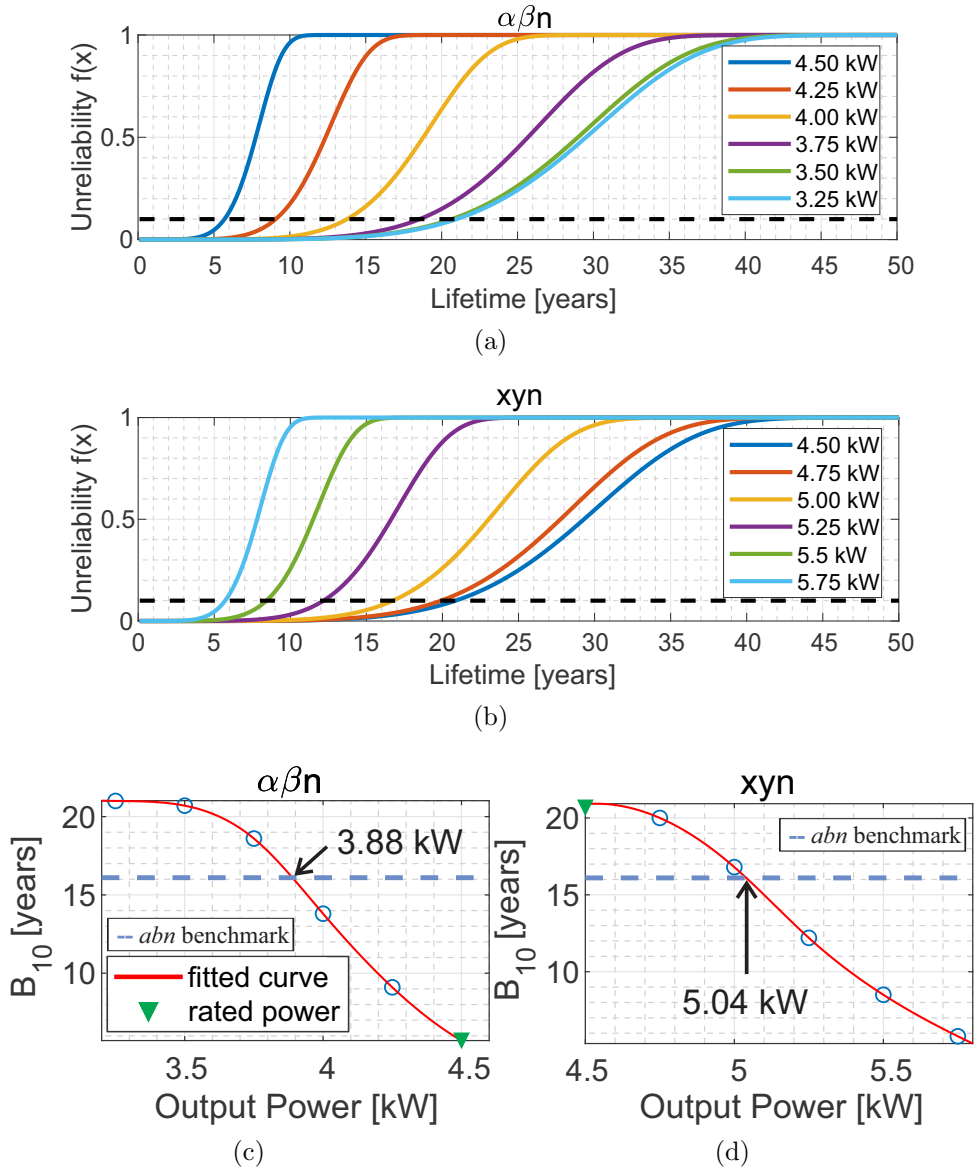

Figure 56 – Unreliability functions for different output power levels in the: (a) $\alpha\beta n$-GFC. (b) xyn-GFC. Sensitivity analysis of the output power for: (c) $\alpha\beta n$-GFC. (d) xyn-GFC.

By the fitted curve in Figure 56(c), the value of B_{10} of $\alpha\beta n$-GFC reaches 16.1 years with 3.88 kW of output power (equivalent to B_{10} in abn-GFC with 4.5kW). Figure 56(b) shows the unreliability function of the overall converter for several output powers in the xyn-GFC. As the output power increases, the reliability is reduced. The values of B_{10} and the fitted curve are shown in Figure 56(d). The B_{10} reaches 16.1 years in the fitted curve at 5.04 kW of output power.

In the study conducted by Burkart and Kolar (2013), a comprehensive cost analysis of various converter topologies is presented, considering different switching frequencies and a nominal power between 5 and 50 kW. The total cost estimation includes the prices of passive components, semiconductors, and the cooling system. The observed range of total costs ranges from € 1000 to € 2500. In the current study, with a nominal power of 4.5

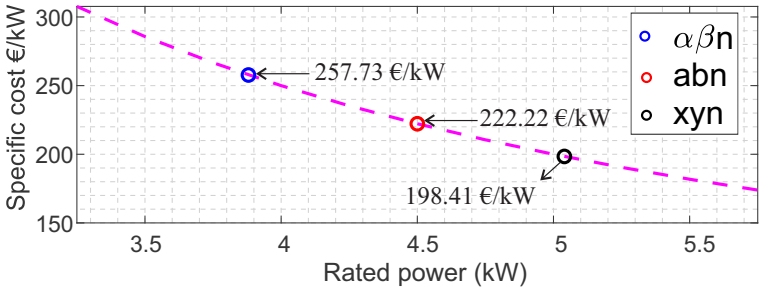

Figure 57 – Relation between specific cost and rated power for a total cost of € 1000.

kW, the lowest cost value of € 1000 was adopted for the sensitivity analysis.

Figure 57 shows the relationship between specific cost and rated power for a total converter cost of €1000. For the same total cost, it is observed that the specific cost (expressed in €/kW) decreases as the nominal power increases. In particular, when the nominal power is 3.88 kW, the $\alpha\beta n$-GFC exhibits the same level of unreliability as the *abn*-GFC, resulting in a specific cost of 257.73 €/kW. This represents a reduction of 15. 9% compared to the specific cost in *abn*-GFC with the same unreliability. On the other hand, *xyn*-GFC achieves a specific cost of 198.41 € / kW for the benchmark unreliability value, translating to a converter cost of 11.7% lower than the converter in the *abn*-GFC operating under nominal conditions.

The second sensitivity analysis determines the heatsink-to-ambient resistance for the same B_{10} lifetime of the *abn*-GFC under nominal conditions. In this second analysis, the thermal resistance of the heatsink was deliberately modified, and the resulting impact on the unreliability of the system was examined. It is worth noting that, in this study, the variation in the thermal resistance of the heatsink specifically influences the temperature of the semiconductors. However, the reported results cover the overall system-level unreliability, taking into account both semiconductors and capacitors. For comparison of different heatsink designs regarding power density, reference (Drofekik; Laimer; Kolar, 2005) shows the 'cooling system performance index (CSPI)', which is:

$$CSPI = \frac{1}{V_H . R_{th-S,a}}, \tag{5.2}$$

where V_H is the volume and $R_{th-S,a}$ is the heatsink-to-ambient thermal resistance. Assuming that all heatsinks in this work have the same CSPI, the volume is inversely proportional to the thermal resistance. In reference Drofekik, Laimer and Kolar (2005), a particular set of heatsink and fan are taken into consideration to allow effective air convection from the converter. By keeping the CSPI value constant, it ensures a consistent relationship between the heatsink volume, the fan area, and the airflow at a specific pressure drop.

Sensitivity analysis is also performed by varying the heatsink-to-ambient thermal resistance to reach the same value in B_{10} of the *abn*-GFC under nominal condition. Figure 58(a) shows the unreliability function of the overall converter for several thermal resistances in the $\alpha\beta n$-GFC. The unreliability increases as the thermal resistance increases. This is

observed in Figure 58(c) that shows the values of B_{10} for the simulated cases and the fitted curve of the points. The $\alpha\beta n$-GFC reaches 16.1 years in the fitted curve with a thermal resistance of 0.136 K/W. Figure 58(b) shows the unreliability function of the overall converter for several thermal resistance in the *xyn*-GFC. The unreliability decreases as the thermal resistance decreases. Figure 58(d) shows the values of B_{10} for the thermal resistances considered and the fitted curve of the points for the *xyn*-GFC. The converter reaches 16.1 years on the fitted curve with a thermal resistance of 0.267 K/W.

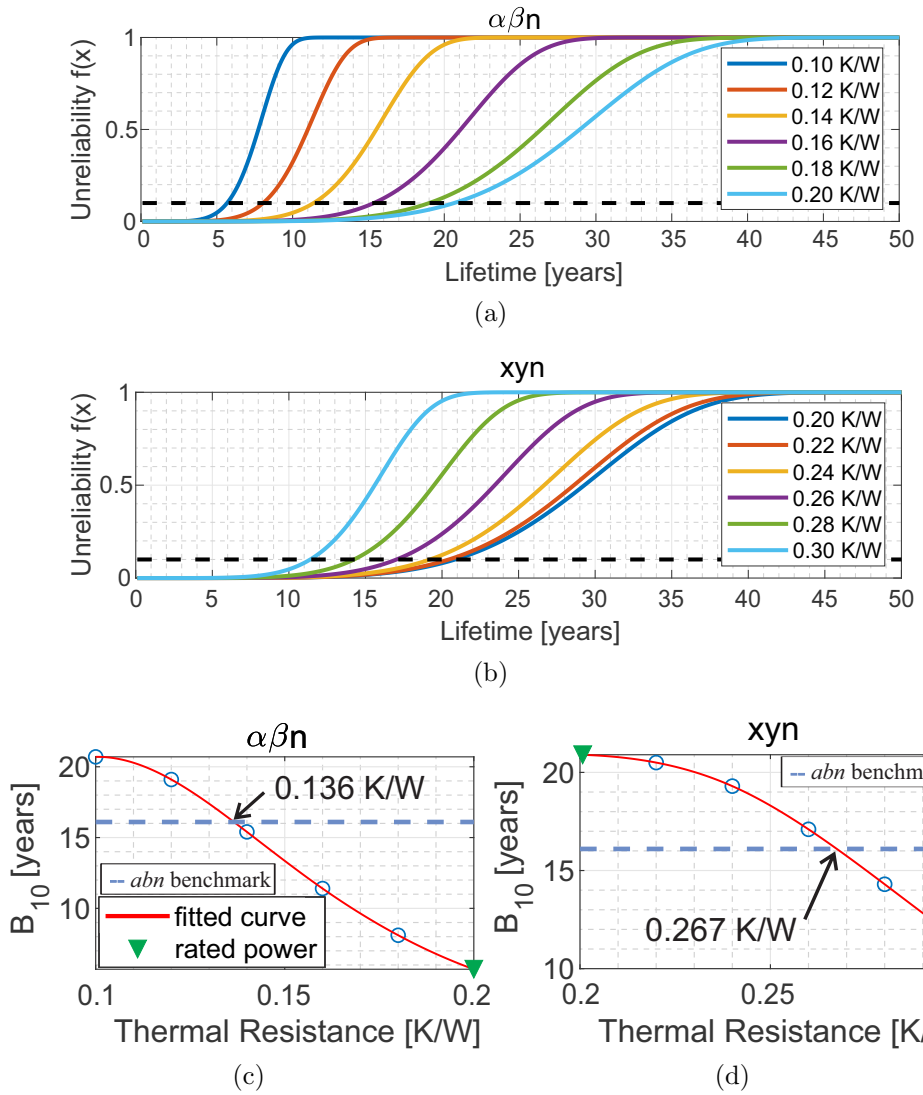

Figure 58 – Unreliability functions for different thermal resistance in the: (a) $\alpha\beta n$-GFC. (b) *xyn*-GFC. Sensitivity analysis of the thermal resistance for: (c) $\alpha\beta n$-GFC. (d) *xyn*-GFC.

For commercial non-optimized heatsinks used in converters operating in the kilowatt range with forced air cooling, the typical range of CSPI values is between 3 and 5 (Drofenik; Kolar, 2006) (Drofekik; Laimer; Kolar, 2005). In this dissertation, a CSPI value of 5 W/K/L is considered for the heatsink of the converter. Figure 59 illustrates the behavior of the converter's volume with a fixed CSPI in relation to the thermal resistance. The thermal

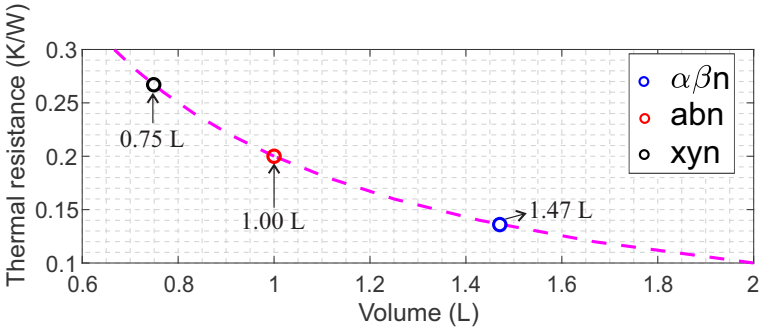

Figure 59 – Relation between volume and thermal resistance for a CSPI of 5 W/K/L.

resistance decreases as the volume increases. The three points on the curve represent the volume values for the thermal resistance in each converter studied that achieve a B_{10} value of 16.1 years. It should be noted that for the same unreliability, *xyn*-GFC would require a heatsink with a volume 25% smaller than the benchmark, which is the *abn*-GFC under rated conditions. On the other hand, for the $\alpha\beta n$-GFC, a heatsink with 47% more volume would be needed to achieve the same unreliability as the *abn* GFC.

5.1.3 Power losses and semiconductor temperature

The analytical model developed in Section 4 shows that the $\alpha\beta n$-converter tends to have higher current stress, while the *xyn*-converter exhibits the lowest current stress. The experimental setup employs an IGBT with a nominal maximum blocking voltage of 3.3 kV. However, the test is conducted using only 150V of blocking voltage, which is significantly below the nominal value. Consequently, it can be assumed that the predominant portion of semiconductor loss is due to conduction rather than switching. Therefore, it is reasonable to expect that the losses for each converter are proportional to the sum of the squares of the RMS currents in semiconductors, assuming constant equivalent series resistance. Based on the equations presented in Table 5, and considering the unity power factor and peak current of 1 pu, it is expected that the power losses of the *abn* converter will be 16.6% lower than the losses of the $\alpha\beta n$-converter. Furthermore, it is expected that the losses in the *xyn*-converter are 33. 3% lower than the losses in the $\alpha\beta n$-converter.

Figure 60 shows the power losses in the converter semiconductors as a function of the DC-link power, obtained in an experimental test bench. The $\alpha\beta n$-converter exhibits higher losses compared to the other two converters. With 500 W flowing through the DC-link, the semiconductor losses in the *abn*-converter are 18% lower than the losses in the $\alpha\beta n$-converter for the same power. Additionally, for the *xyn*-converter, losses are 41% lower than those of the $\alpha\beta n$-converter for the same power. The differences between the model and the experiment can be attributed to various factors that influence the losses in the converters. These factors include temperature effects, switching characteristics, and the material properties of each semiconductor. Currently, our stress model does not account for these specific influences, which could explain the discrepancies in the losses between

the converters. In future work, the authors plan to improve the stress model to include these additional factors for a more comprehensive and accurate analysis.

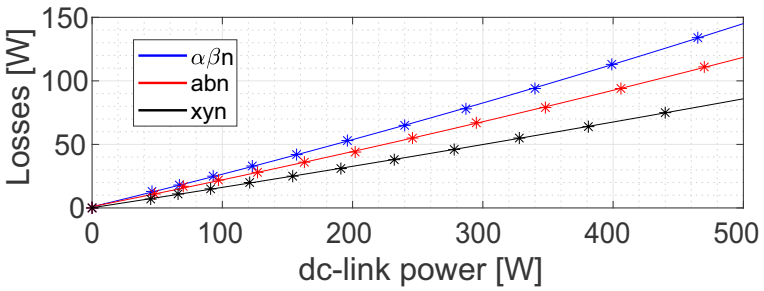

Figure 60 – Semiconductor losses of the 2Φ3W converter considering the $\alpha\beta n$, *abn* and *xyn* converters.

Figure 61 shows the case temperature of IGBTs S_1 and S_5. In the initial phase of the test, the temperature of the neutral IGBT is higher than that of the phase IGBT, which is expected, as the neutral current is higher than the phase current when the converter operates in the $\alpha\beta n$-GFC. After one hour, the temperature of IGBT S_5 reached 122 °C, while IGBT S_1 temperature was approximately 102 °C, showing a difference of about 16.4% lower than the neutral IGBT.

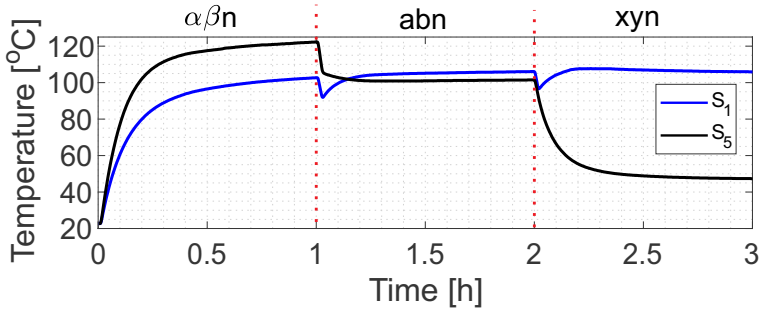

Figure 61 – Case temperature on IGBTs S_1 and S_2 of the 2Φ3W converter considering the $\alpha\beta n$, *abn* and *xyn* converters.

During the second test hour shown in Figure 61, the converter operates as an *abn*-converter. In this case, the temperatures of IGBTs S_1 and S_5 become similar, measuring 106 °C for IGBT S_1 and 102 °C for IGBT S_5. This closeness in temperature is expected because the currents are now equal. Moving on to the third hour of the experiment, it is observed that the temperature of the switch S_5 drops significantly to 48 °C. This drop is due to the neutral current being zero under these conditions, acting as a *xyn*-converter.

The temperature variations in the semiconductors align well with the losses studied previously. As seen before, the converter with the highest losses, the $\alpha\beta n$-converter, also exhibits higher temperatures in the neutral IGBT. On the contrary, the *xyn*-converter, which presents lower losses, also shows lower temperatures when operating under the same conditions.

5.2 Open module setup results

5.2.1 Unreliability Results

These results were obtained considering a mission profile presented in Section 3.3, taking into account characteristics of an isolated system in the Amazon region. The thermal model adopted for losses considered the Foster model. Figure 62(a) shows the unreliability function for the IGBT S_1 of the GFC. The value in B_{10}, which indicates the time when 10% of the samples have failed, is similar for the *abn*-GFC and $\alpha\beta n$-GFC. However, the probability of failure for the same IGBT in *xyn*-GFC is lower, reaching B_{10} in 33.1 years. Figure 62(b) shows the unreliability function for the IGBT S_5 of the GFC. It is noted that the loss lookup tables for the IGBTs S_5-S_6 and diodes d_5-d_6 differ among the three evaluated converters and the most significant disparity in thermal stress is observed among the neutral semiconductors.

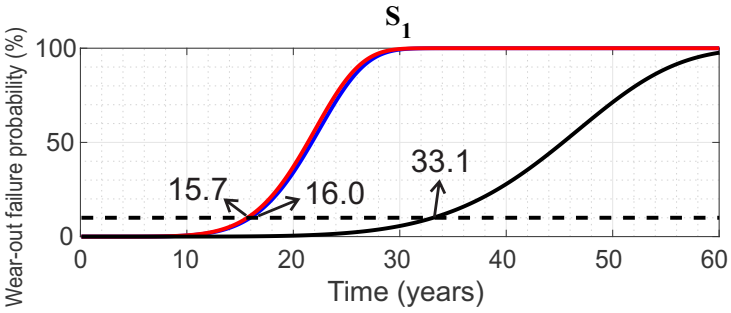

(a)

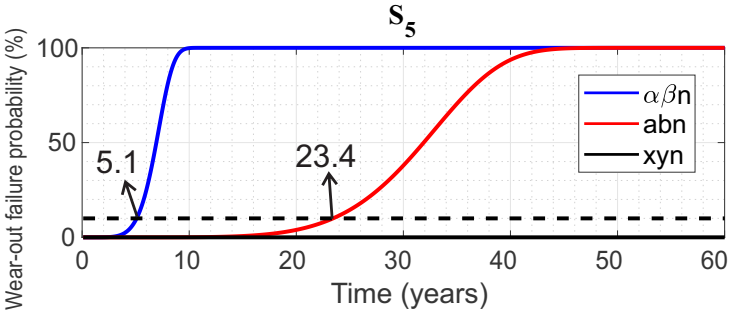

(b)

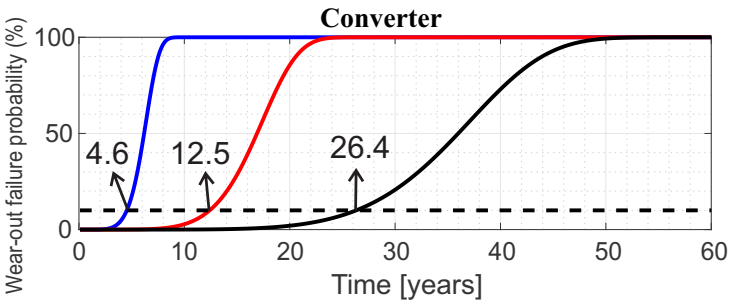

(c)

Figure 62 – (a) IGBT S_1 unreliability function. (b) IGBT S_5 unreliability function. (c) Overall converter level unreliability function considering all semiconductors.

The $\alpha\beta n$-GFC shows the highest thermal stress in the neutral leg, resulting in a low unreliability value in B_{10} for IGBT S_5 (5.1 years). For these results, the converter under balanced load is considered, in which the current through the neutral leg of the *xyn*-GFC is zero. Thus, the only loss in this IGBT is the switching one, which statistically implies that this IGBT has a low probability of failure, with its value at B_{10} estimated at 3500 years.

The unreliability of the converter considering all the IGBTs and diodes for the three converters studied in this dissertation is shown in Figure 62(c). The *xyn*-GFC has the lowest probability of failure, with a B_{10} value of 26.4 years. As expected, the $\alpha\beta n$-GFC exhibits a highest probability of failure due to the more significant thermal stress imposed on the semiconductors (4.6 years). The *xyn*-GFC presents 111.2% higher value in B_{10} than the *abn*-GFC, and 473.9% higher value in B_{10} compared to the $\alpha\beta n$-GFC.

5.2.2 Thermal Results

5.2.2.1 Balanced load conditions

The converter running under balanced load is considered in the first test, and a long-term test is conducted to allow the converter to reach steady-state temperature. The results display thermal images of the converter with flowing 585 W of output power. For each case, the converter had been in operation for one hour before capturing the images.

Figure 63 shows the module semiconductors thermal images for the $\alpha\beta n$, *abn*, and *xyn* converters. Figure 63(a) shows the temperature for the $\alpha\beta n$-GFC. Note that the neutral IGBTs and diodes experience higher stress levels than the phase ones, resulting in higher temperatures reaching 115 ^{o}C. The semiconductor temperature for the *abn*-converter is shown in Figure 63(b). Generally, the module temperature is lower than observed in the $\alpha\beta n$-GFC. Furthermore, it seems that the IGBTs exhibit similar temperatures, since the current passing through the phase and the neutral components are equal.

The *xyn*-GFC shows the lowest thermal stress, as seen in Figure 63(c). The module temperature difference is barely discernible on the temperature scale used for the other two converters. Figure 63(d) shows the temperature on different scales for visualization purposes. The temperature of the neutral IGBTs is significantly lower, and they do not exhibit hotspots like phase semiconductors. Notably, all semiconductors are mounted on the same heatsink, implying that the thermal impedance remains consistent throughout the power semiconductor module. However, even under identical operational conditions, different temperatures are observed for the phase semiconductors and, consequently, different unreliability values. In addition, the current flowing through the neutral leg contributes to the variability in the temperatures of the adjacent semiconductors.

Figure 64 shows the thermal image temperature histograms of each converter

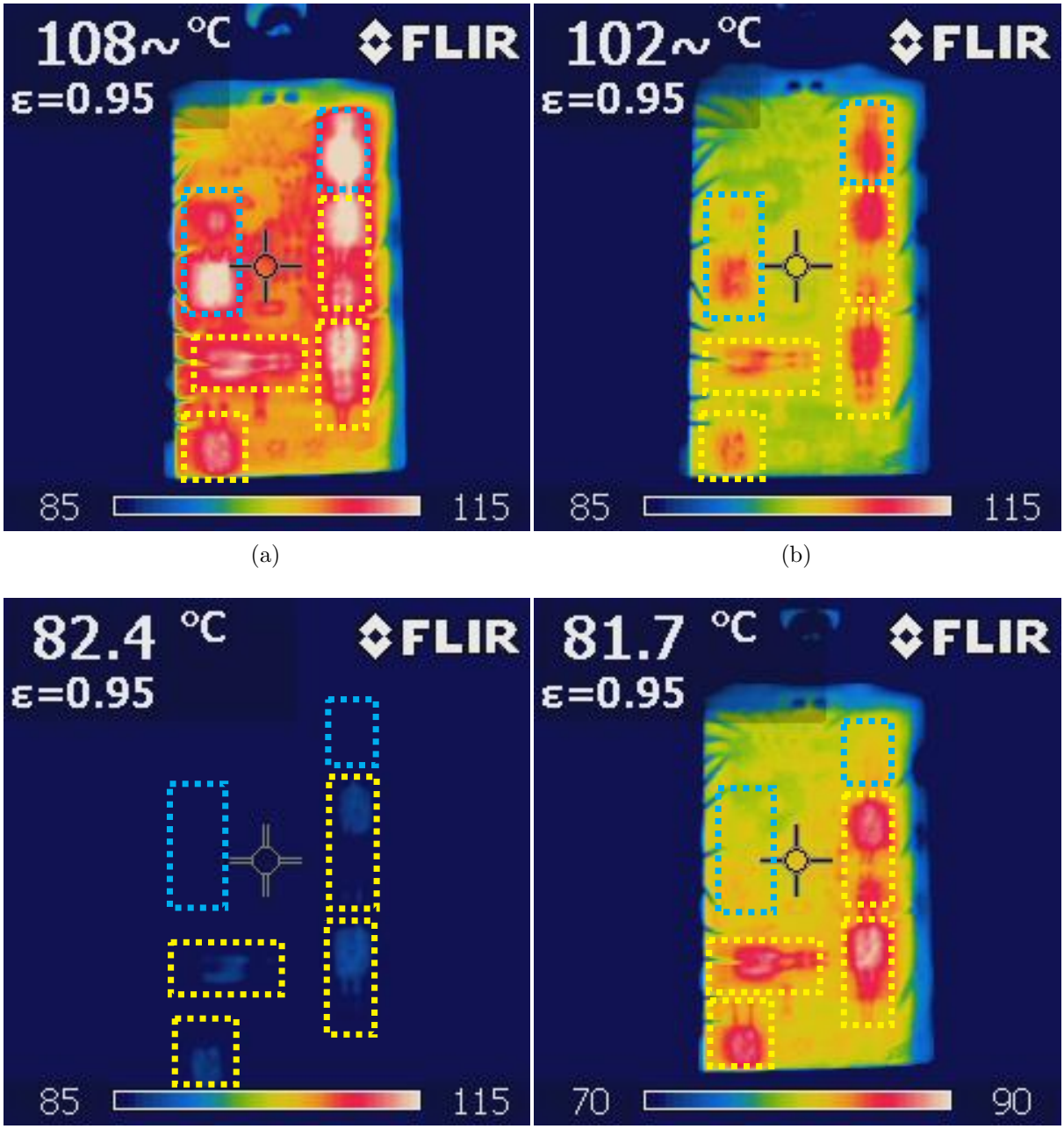

Figure 63 – Thermal images of the semiconductors of the GFC operating on: (a) $\alpha\beta n$-GFC; (b) *abn*-GFC; (c) *xyn*-GFC; (d) *xyn*-GFC with different temperature scale.

operating under balanced load conditions. These histograms show the temperature distribution between pixels in Figures 63(a), 63(b) and 63(d). The images were cropped to focus on the interior of the semiconductor module. The *xyn*-GFC has the lowest average temperature at 81.8 °C. This makes the *xyn* GFC average temperature 19.4% cooler than the *abn* GFC and 23.3% cooler than the $\alpha\beta n$ GFC.

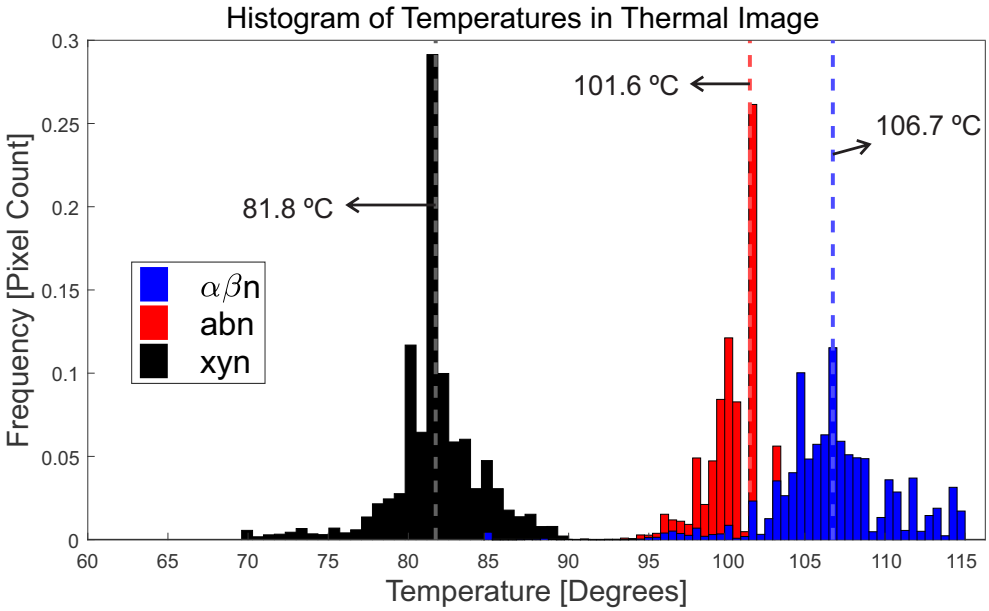

Figure 64 – Histogram of temperatures in thermal images for balanced load conditions.

5.2.2.2 Unbalanced load conditions

The test comprises operating the converter for one hour until it reaches the steady state with 500 W of output power evenly distributed between the two phases. Once steady state is achieved, a load unbalance is introduced in which one phase carries 250 W of power while the other carries 75 W. The same test is conducted for the three converters. It is worth noting that the converter runs in open-loop control configuration, meaning that the decrease in current in one phase leads to lower line-to-neutral voltage than in the other phase.

Figure 65 shows the thermal images for the $\alpha\beta n$-converter operating under load balanced and unbalanced conditions. As Figure 32 illustrates, irrespective of the unbalance, the neutral current in the converter is greater than the phase current. The module temperature is lower because the converter processes less power. However, it is still noticeable that the temperature in the neutral semiconductors is higher than that in the unbalanced phase semiconductors.

The thermal images for the *abn*-converter operating under balanced and unbalanced loads conditions are shown in Figure 66. Figure 32 shows that for a σ value of 0.5, the RMS current through the switch S_5 is higher than that through the switch S_3. Furthermore, Figure 66(b) shows that the temperature through the neutral IGBTs is slightly higher than the unbalanced phase IGBTs. In the case of *abn*-GFC, for values of σ below 0.674, the RMS current through the neutral IGBTs is higher, resulting in increased power losses and, consequently, higher temperatures in the neutral IGBTs.

Finally, Figure 67 shows the thermal images for the *xyn*-converter operating under balanced and unbalanced loads conditions. Note that the introduction of the unbalance leads to current flow through the neutral leg, resulting in a temperature hotspot in the

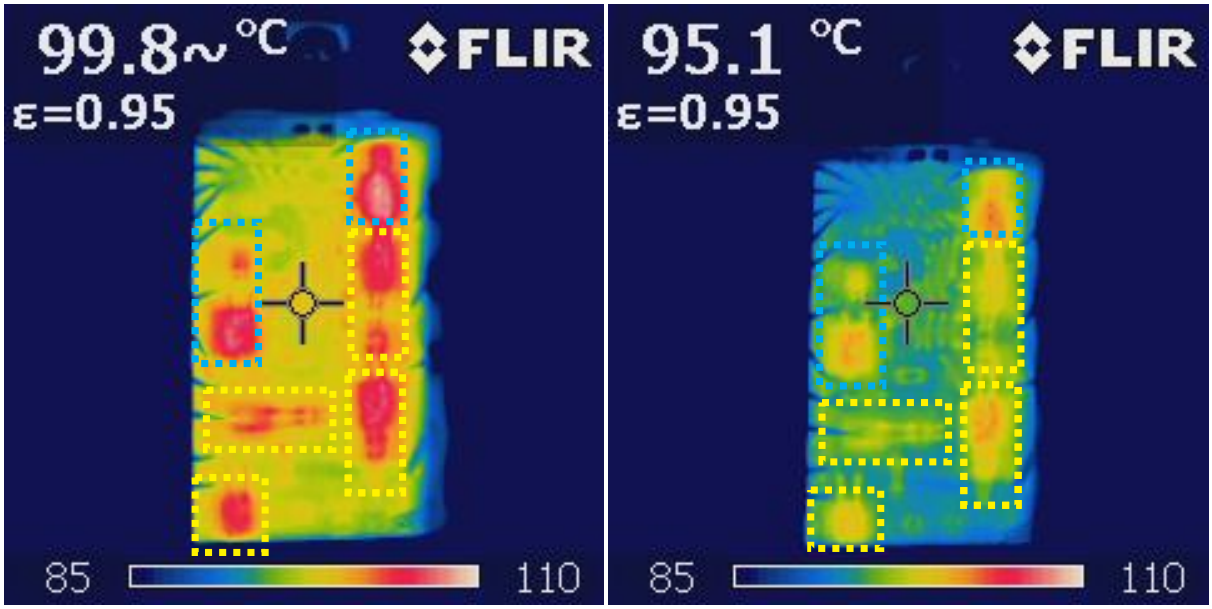

(a) (b)

Figure 65 – $\alpha\beta n$ converter operating under: (a) balanced load conditions, flowing 250W in each phase; (b) unbalanced load conditions, flowing 250W in phase j and 75 W in phase k.

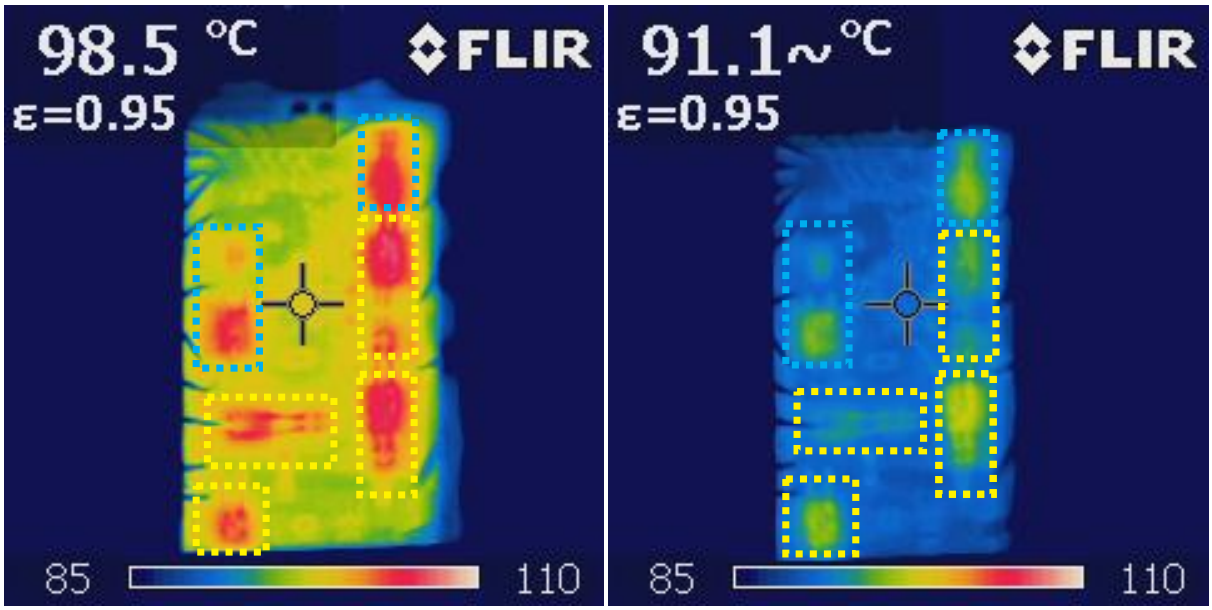

(a) (b)

Figure 66 – *abn* converter operating under: (a) balanced load conditions, flowing 250W in each phase; (b) unbalanced load conditions, flowing 250W in phase j and 75 W in phase k.

neutral semiconductors. Irrespective of the unbalance, the converter shows higher thermal stress when operating as $\alpha\beta n$-GFC while consistently exhibits lower temperatures when operating as *xyn*-GFC.

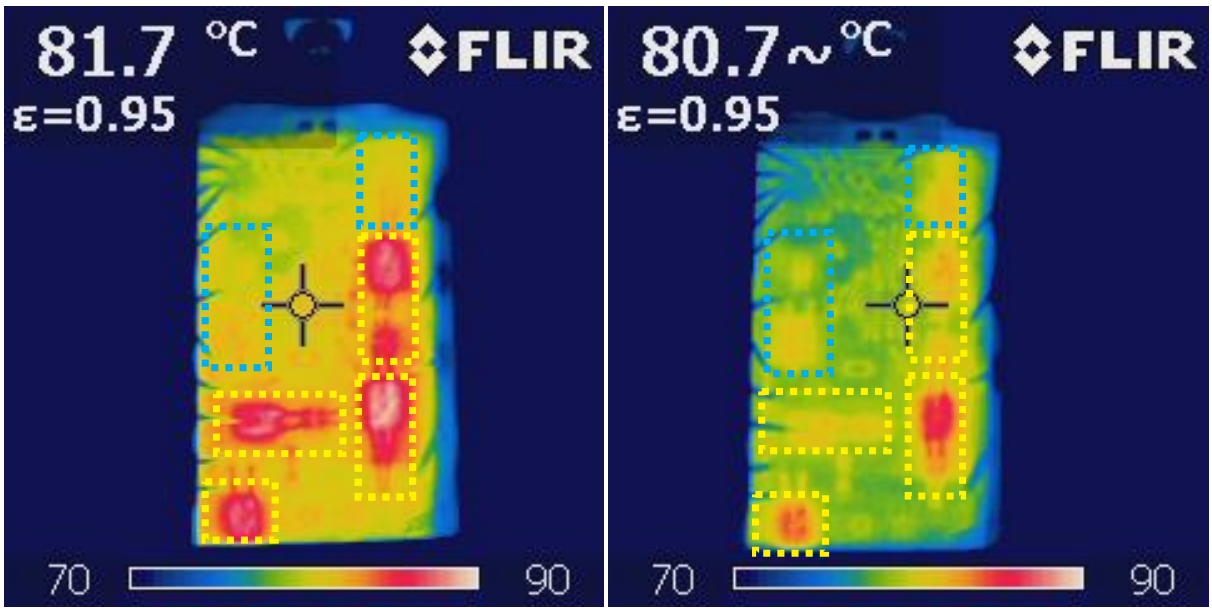

(a) (b)

Figure 67 – *xyn* converter operating under: (a) balanced load conditions, flowing 250W in each phase; (b) unbalanced load conditions, flowing 250W in phase j and 75 W in phase k.

5.3 Further discussion

For IGBT devices, the thermal stress is a function of the current through each semiconductor. Thus, the analytical model shows that the $\alpha\beta n$-GFC, which has the highest RMS current in the neutral leg semiconductor, also has a higher probability of wear-out failure. The *xyn*-GFC has the lowest probability of wear-out failure, precisely because it has less stressed semiconductors.

For DC-link capacitors, the analysis of the analytical model provides important information, not found in the literature for 2Φ3W converters. Reference (Alibeik; dos Santos Jr.; Blaabjerg, 2014) states that there are no low-frequency components on the DC-link capacitors in the $\alpha\beta n$-GFC which benefits its design. Analyzing the voltage of the DC-link capacitor and the instantaneous power, it is noticed that the *xyn*-GFC presents highest low-frequency oscillation on the DC-link capacitor. This can lead to conclusions that the $\alpha\beta n$-GFC has lower capacitor losses. However, when high-frequency components are taken into account, the conclusions are quite different. The RMS DC-link current is higher in the $\alpha\beta n$-GFC, showing that high-frequency components increase power losses in DC-link capacitors. Thus, the analytical model supports the results obtained in the wear-out analysis section that the power loss function is a complex association between capacitor RMS current, capacitor voltage and ESR frequency dependence.

5.4 Chapter closure

This chapter presented reliability results for the 2Φ3W converters. With respect to semiconductors, the fact that the $\alpha\beta n$-GFC exhibits a higher neutral current than the other converters under balanced load conditions makes it more thermally stressed, resulting in lower reliability and shorter lifespan compared to the other converters.

The thermal results confirm the better thermal performance of the *xyn*-GFC, both in the semiconductor module setup and in the setup with discrete IGBTs. The results showed that regardless of the operating conditions, the the *xyn*-GFC shows better thermal performance under balanced and unbalanced load conditions.

The quest for more reliable converters drives the field of power electronics to seek ideas to improve the heat dissipation of the components, thus reducing the risk of failure. The next chapter introduces the use of oil-immersed converters, to improve the thermal performance of the converters and increase their reliability, particularly in 2Φ3W converter applications.

6 Oil immersed two-phase three-wire converter

The pursuit of size reduction remains a longstanding objective in the field of power electronics (Jahns; Dai, 2017). The quest for component size reduction raises concerns regarding device temperatures, particularly in power semiconductor devices. The combination of smaller surface areas and higher switching frequencies poses greater challenges and emphasizes the importance of efficient heat dissipation for the optimal performance and functionality of these devices.

In the pursuit of improved heat dissipation, liquid plate cooling has been explored as a potential solution. However, this approach typically involves additional systems and components such as secondary circulation systems and heat exchangers, which add complexity and cost to the overall system (Abdullah et al., 2019). This chapter focuses on the evaluation of an alternative approach that involves using an insulating and thermally conductive liquid as the ambient medium for the electronic system.

Liquid immersion cooling has a long history of usage in power devices for transformers and high-voltage rectifiers (Pires et al., 2020). However, in recent years, it has gained popularity and is being more commonly employed in modern electronics applications, including data centers (Tuma, 2010). Reference (Tuma, 2010) presents an evaluation of liquid immersion cooling methods, specifically passive 2-phase immersion cooling and all-liquid cooling. In reference (Pires et al., 2020), a prototype press-pack diode with two heat sinks is immersed in a tank of mineral oil, utilizing natural convection cooling. The paper showcases the experimental results of this setup, demonstrating the promising potential of liquid immersion cooling for enhancing heat dissipation in power devices.

Reference (Mahanta, 2020) investigates renewable alternatives to mineral oil, including the Cargill FR3 fluid. FR3 fluid is derived from soy and offers several advantages, such as being non-toxic, biodegradable, and environmentally friendly. The goal is to explore sustainable options that align with environmental considerations while maintaining or improving performance. In (Turnbull; Venkataramanan; Ludois, 2023), the authors present their initial experimental findings using Cargill FR3 fluid, to protect submerged electronics from electric field breakdown. This innovative approach opens up new possibilities for designing electronics with an increased power density and smaller footprints. Furthermore, the paper proposes that immersion of electronics in the insulating FR3 fluid will enhance thermal power dissipation, further improving the overall performance of the system.

This chapter presents an empirical investigation to demonstrate the potential performance improvement achieved by immersing test prototypes in insulating fluids to enhance heat dissipation. The use of Cargill FR3, a liquid with improved electrical and thermal properties, as the ambient medium replaces the conventional air cooling approach.

6.1 Thermal Characteristics in Liquid-immersed Converters

When air is replaced with an insulating liquid that has a higher voltage withstand capacity, there is the potential to achieve smaller package sizes. In the thermal design of power devices and circuits, the heat transfer coefficient between the device and the surrounding environment, typically air, plays a critical role. In particular, the heat transfer coefficients between flat surfaces and liquids are significantly higher than those associated with ambient air.

The thermophysical properties of air and FR3 are obtained from (Nellis; Klein, 2021) under nominal conditions, and (Martin, 2008) respectively, and are summarized in Table 8. The unique properties of FR3 are notable for their positive impact on thermal characteristics. Notably, FR3 exhibits a higher thermal conductivity compared to air, which improves its ability to effectively transfer heat. Additionally, FR3 possesses a lower thermal diffusivity compared to air. This combination of characteristics ensures improved heat dissipation from the environment where FR3 is used, providing greater efficiency in thermal management.

Table 8 – Key Thermal and Physical Properties of Air at nominal T= 26.85 ^{o}C (300K) and Cargill FR3 (Nellis; Klein, 2021) (Martin, 2008).

Property	**Air**	**FR3**
Density $[kg/m^3]$	1.177	920
Expansion coefficient $[m/C]$	3.33	0.75
Specific heat $[kJ/kg \cdot C]$	1.01	1.88
Thermal Conductivity $[mW/m \cdot K]$	26.4	167
Thermal Diffusivity $[mm^2/s]$	22.27	0.097
Insulating Strength $[kV/mm]$	3	25

This chapter aims to investigate the thermal characteristics of a three-phase full-bridge converter and to assess the stress on semiconductors. Both prototypes used the same converter PCB, with one operating in air as shown in Fig. 25b, and the other immersed in oil as shown in Fig. 68. In the case of the oil-immersed converter, the box was carefully sealed to ensure no oil leakage and a pump was incorporated to circulate the oil within the system. It is important to note that the pump's sole function is to circulate the liquid and that there is no heat exchange mechanism present within the box.

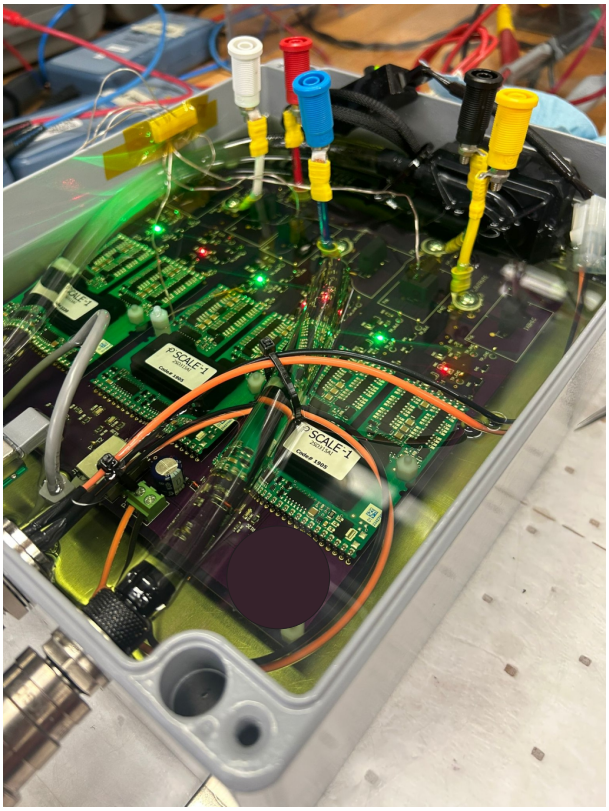

Figure 68 – 2Φ3W converter immersed in oil.

6.2 Thermal Performance of Liquid-immersed Power Converter

For the analysis of the thermal performance of the oil-immersed converter, the case temperatures of S_1 (phase IGBT) and S_5 (neutral IGBT) were monitored in an experiment carried out to compare the temperatures in the oil-immersed converter and in the air. The experiment has a duration of three hours. The voltage on the DC bus is kept constant at 200 V, with an RL load connected at the output with the values presented in Table 4. The experiment starts with the $\alpha\beta n$-GFC, after one hour, the converter switches to operate as *abn*-GFC, and finally it operates as *xyn*-GFC.

Figure 69 shows the current flowing in the output of the converters during the experiment in both converters. The temperatures measured during the experiment are shown in Figure 70. In the first hour, the temperature of the neutral IGBT is higher than that of the phase IGBT in both converters. As shown in Figure 69(a), the neutral current is higher than the phase current, therefore, a higher temperature is expected in neutral IGBT. When comparing the converters, the operation of the converter immersed in FR3 results in a temperature reduction for the IGBTs. The neutral IGBT experiences a temperature decrease of 30.8%, and the phase IGBT shows a temperature decrease of 33.6% compared to the IGBTs operating in the air converter.

When the *abn*-GFC begins to operate, the temperature of IGBT S_5 decreases. As

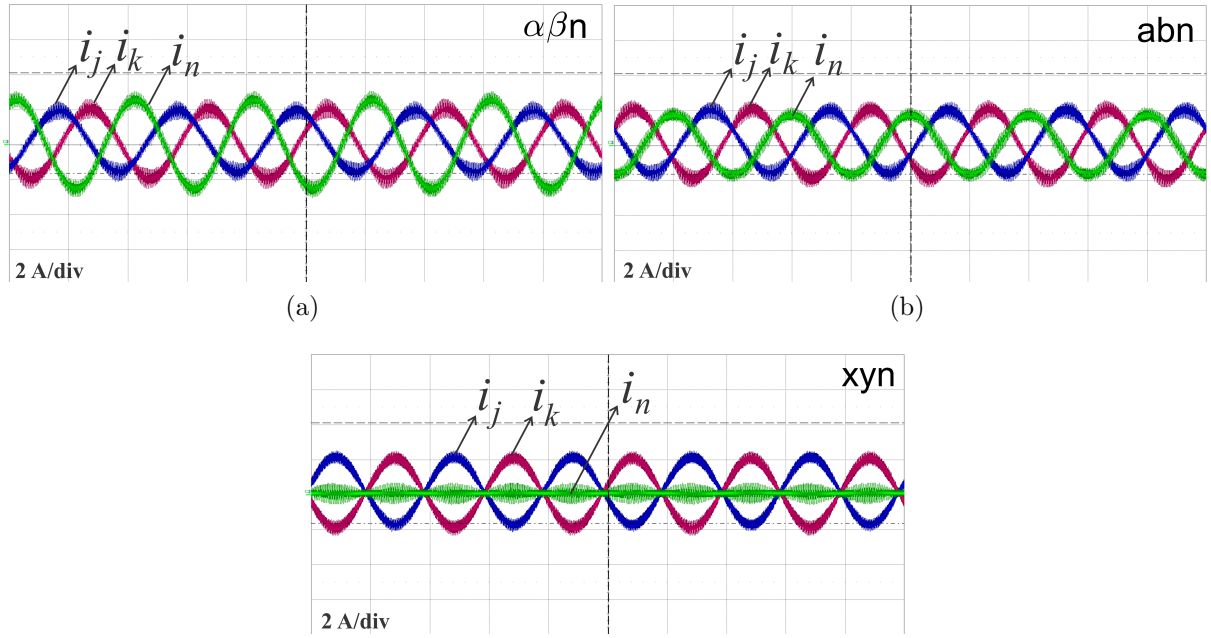

Figure 69 – Current during the experiment for: (a) $\alpha\beta n$-GFC. (b) *abn*-GFC. (c) *xyn*-GFC.

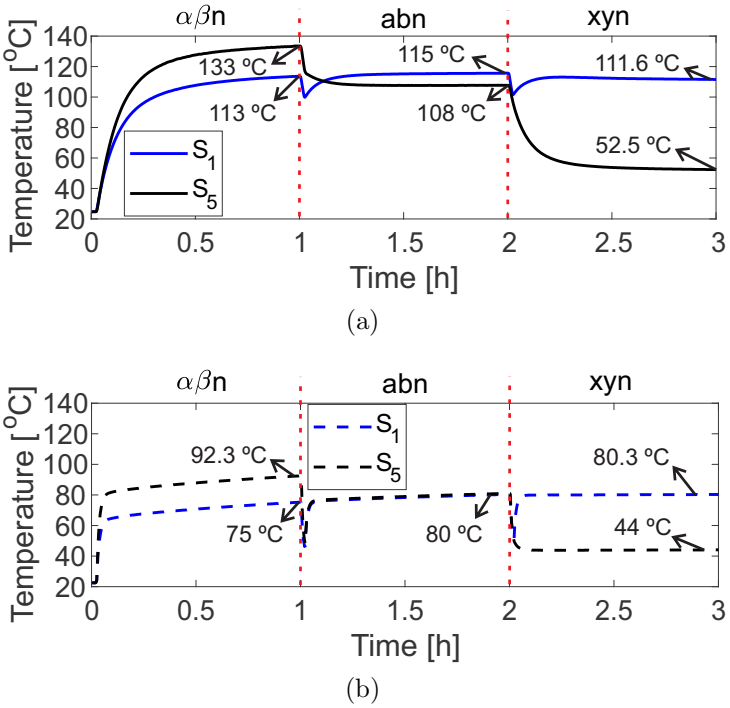

Figure 70 – Case temperature of the IGBTs S_1 and S_5 for: (a) air converter. (b) oil-immersed converter.

indicated in Figure 69(b), the neutral current is now slightly lower than the phase current, which is reflected in the temperature displayed in the IGBTs. Once again, it is observed that the temperatures are lower in the FR3-immersed converter, with a reduction of 30.4% for the IGBT S_1 and 25.6% for the IGBT S_5.

Finally, the *xyn*-GFC starts operating during the last hour of the experiment. As

the system is balanced, it is observed that the neutral current is zero, as shown in Figure 69(c). During this hour, the converter exhibits the greatest temperature disparity among the IGBTs. Figure 70(a) shows that the temperature difference between the IGBTs in the air converter is 61.4 °C, while in the oil-immersed converter it is 36.3 °C as shown in Figure 70(a).

These results demonstrate that the operation of power converters immersed in oil is highly promising. Simple immersion in oil enhances the thermal performance of the converter, resulting in lower thermal stress compared to that of the same converter operating in air. Immersion in oil, coupled with heat extraction techniques, can enable these converters to be applied in high-power scenarios with a high power density and low volume.

6.3 Voltage Breakdown Analysis in Liquid-Immersed Power Converter

The use of oil-immersed converters has great applicability in medium voltage converters. A cursory comparison of the insulating strength of air (nominally about 3kV/mm) with an insulating fluid Cargill FR3 (nominally about 25kV/mm) indicates a potential for a 10-fold improvement in voltage withstand capacity that can be achieved in electric circuits immersed in FR3 compared to air (Cargill, 2021).

To assess this potential, the dielectric properties of FR3 were tested against air using the converter design PCB. High-voltage breakdown measurements between selected points on the PCB were performed using a Hi-Pot tester under ambient air conditions and under ambient FR3 conditions. Figure 71 shows the unpopulated PCB under test.

The test involves applying voltage across the PCB terminals until a voltage breakdown occurs. Initially, the test was carried out with the PCB exposed to air and subsequently immersed in FR3. Throughout the test, both the DC and AC voltage were applied between the dc-link terminals and the three-phase output of the converter.

Table 9 presents the Hi-Pot outcomes for dc and ac voltage applications at the PCB terminals. Notably, during the dc voltage test, it is evident that a voltage breakdown accompanied by sparks occurs on the air PCB when the voltage ranges between 3 and 4.5 kV. In contrast, upon submerging the board in FR3, no voltage breakdown accompanied by sparks is observed, even up to the Hi-Pot's maximum dc voltage limit of 11.8 kV.

Analogous findings are evident in the AC voltage test. During this assessment, the PCB exposed to air exhibits voltage breakdown with sparks at a maximum terminal voltage of 3.3 kV. On the contrary, the PCB immersed in FR3 withstands the test successfully without experiencing voltage breakdown. These results highlight the considerable potential

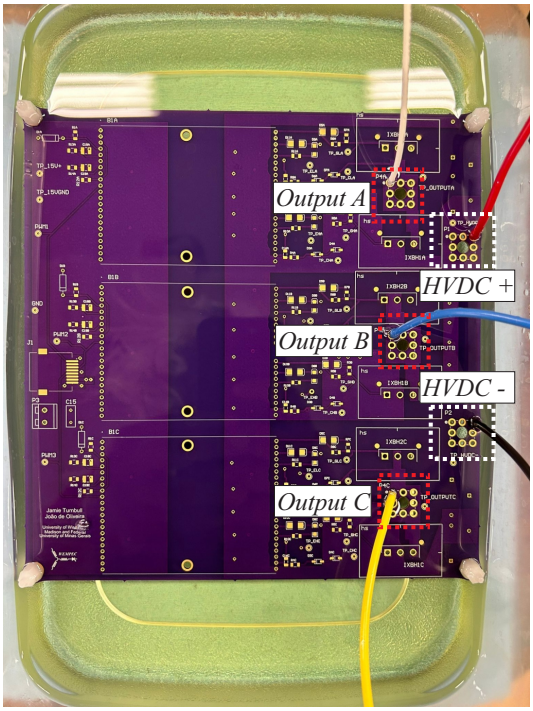

Figure 71 – Hi-Pot test on the PCB.

of the oil-immersed converter for medium-voltage applications. When submerged in oil, the converter becomes capable of operating at elevated voltage levels within a more compact volume, thereby yielding a converter with higher power density.

Table 9 – Hi-Pot results for dc and ac voltage application at the PCB terminals.

HVDC Hi-Pot	**Test Voltage**	
Terminals	**Air**	**FR3**
HVDC+ to HVDC-	4 kV - Fail with spark	11.8 kV - Pass
HVDC+ to 3 phase output	4.5 kV - Fail with spark	11.8 kV - Pass
HVDC- to 3 phase output	3.5 kV - Fail with spark	11.8 kV - Pass
HVAC Hi-Pot	**Test Voltage**	
Terminals	**Air**	**FR3**
HVDC+ to HVDC-	3.2 kV - Fail with spark	11.3 kV - Pass
HVDC+ to 3 phase output	3.3 kV - Fail with spark	11.3 kV - Pass
HVDC- to 3 phase output	3.3 kV - Fail with spark	11.3 kV - Pass

Although this dissertation focuses on low-power converters and low-voltage applications, these results demonstrate that the immersed converter can withstand voltage surges caused, for example, by atmospheric discharges. The results showed that high voltages can be applied without voltage breakdown occurring in the converter.

6.4 Chapter closure

This chapter demonstrates the significant potential of oil-immersed converters, specifically utilizing Cargill FR3 in this dissertation. The tests indicate improved

heat exchange performance, resulting in lower operating temperatures across all tested conditions.

The thermal performance of the 2Φ3W converter, especially the *xyn*-converter, is enhanced when immersed in oil. Additionally, initial empirical tests indicate that immersion in oil allows this converter to be applied in medium voltage because of the improved dielectric characteristics exhibited by the oil.

There are still some aspects that need further exploration in this study of oil-immersed converters. The first is related to component degradation. All components used were originally designed to operate in air, and it is not known how they will degrade when immersed in FR3. Another important aspect is to analyze the moisture content of the oil. The tests were conducted in a controlled environment, but it is crucial to monitor the oil's moisture levels to prevent accidents. Lastly, heat extraction techniques are essential to apply this converter in higher power applications.

7 Conclusions

This dissertation proposed the *xyn*-converter used in isolated two-phase three-wire AC power grids. The use of this converter topology ensures greater reliability of converters in two-phase three-wire systems. General analytical expressions are proposed to evaluate current stresses in the GFC operating in three different grid configurations in terms of line voltage displacement angles (i.e., 90°, 120° and 180°). It also compared the wear-out prediction of the IGBTs and dc-link capacitors, and performs tests to show the thermal behavior of semiconductors.

In terms of lifetime, the *xyn*-GFC demonstrates superior results by exhibiting a lower probability of failure compared to the other two converters. Experiments demonstrate that the *xyn*-converter experiences lower thermal stress. Regardless of whether the converter supplies balanced or unbalanced loads, the temperatures recorded in the *xyn*-GFC are consistently lower compared to the other converters when considering the same power level. Conversely, $\alpha\beta n$-GFC exhibits greater thermal stress in all cases, indicating higher temperatures. Under balanced load conditions, the *xyn* converter shows a 19. 4% lower average temperature than *abn*-converter, and 23.3% lower average temperature than $\alpha\beta n$ converter, using the open module prototype. The results validated the proposed analytical expressions.

In this study, the thermal performance of a two-phase three-wire converter was investigated. Empirical results indicated that the use of oil-immersed converters improves the thermal performance of the converter. The temperature of the IGBTs was observed to undergo a reduction of up to 33.6% when immersed in oil. The dielectric characteristics of the oil were also examined. The HiPot test indicated that higher voltage values can be used in the oil-immersed converter, making its application in medium voltage very attractive, as the converter can operate with higher voltages and smaller volume.

7.1 Research perspectives

Although many aspects related to 2Φ3W converters have been studied in this dissertation, some interesting points can be explored in future research, such as:

- Thermal analysis of DC-link capacitors: As indicated, from a reliability point of view, the DC-link capacitors show similar reliability values. Experimental results can help to understand the thermal stresses to which these capacitors are subjected during operation.

- More detailed study of 2Φ3W converter control: Future studies should include proposal control strategies that allow the operation of such converters in weaker 2Φ3W grids and maximize the useful life of these converters.
- Study of the control of 2Φ3W converters under the conditions of asymmetric voltage faults. Propose a control with sequence injection to mitigate these asymmetric voltage faults.
- Reliability analysis of the 2Φ3W systems and not just the converter: A system with different loads and various generation sources can be explored. Experiments considering a complete 2Φ3W grid will be important to implement 2Φ3W systems in isolated locations similar to those studied in this dissertation.

With these and other ideas, the author hopes that the studies presented continue to lead to new discoveries, further analysis, and do not end with this dissertation.

References

Abdullah, Y.; Li, X.; Wang, K.; Wang, J.; Liu, L.; Bala, S. High temperature design of a gan based modular integrated drive with natural cooling using metal clad pcbs. In: *2019 IEEE Energy Conversion Congress and Exposition (ECCE)*. 2019. p. 4012–4017. 112

Aberilla, J. M.; Gallego-Schmid, A.; Stamford, L.; Azapagic, A. Design and environmental sustainability assessment of small-scale off-grid energy systems for remote rural communities. *Applied Energy*, v. 258, p. 114004, 2020. ISSN 0306-2619. Available in: <https://www.sciencedirect.com/science/article/pii/S0306261919316915>. 37

Albertsen, A. *Electrolytic capacitor lifetime estimation*. 2021. Available in: <http://jianghai-america.com/uploads/technology/JIANGHAI_Elcap_Lifetime_-_Estimation_AAL.pdf>. 58

Alderton, S. *Hybrid Micro-Grids with Bioenergy and Solar PV for Rural Electrification in Mipindiaú, Brazil*. Thesis (Master) — Department of Chemical & Biological Engineering University of Sheffield, 2020. 30

Alibeik, M.; dos Santos Jr., E. C.; Blaabjerg, F. Symmetrical components and power analysis for a two-phase microgrid system. *Power and Energy Conference at Illinois (PECI)*, 2014. 41, 51, 110

Alonso, A. M. S.; de Oliveira, J. H.; Brandao, D. I.; Bonaldo, J. P.; Paredes, H. K. M.; Marafao, F. P. Cpt-based control strategy for a two-phase three-wire pv inverter: A multifunctional perspective and a comprehensive review. *Eletrônica de Potência (SOBRAEP)*, v. 27, 2022. 40, 47

Alonso, A. M. S.; Paredes, H. K. M.; Filho, J. A. O.; Bonaldo, J. P.; Brandão, D. I.; Marafão, F. P. Selective power conditioning in two-phase three-wire systems based on the conservative power theory. *IEEE Ind. Appl. Soc. Annu. Meet.*, 2019. 46

Andrade, C. S. *Energia elétrica e as populações tradicionais do Estado do Amazonas: aprendizados a partir da experiência na Comunidade do Roque na Reserva Extrativista do Médio Juruá*. Thesis (Ph.D.) — Federal University of Rio de Janeiro, 2010. 29, 30

Antonopoulos, A.; D'Arco, S.; Hernes, M.; Peftitsis, D. Limitations and guidelines for damage estimation based on lifetime models for high-power igbts in realistic application conditions. *IEEE Trans. Emerg. Sel. Topics Power Electron.*, p. 1–1, 2020. 56, 57

Bakeer, A.; Chub, A.; Shen, Y. Reliability evaluation of isolated buck-boost dc-dc series resonant converter. *IEEE Open Journal of Power Electronics*, v. 3, p. 131–141, 2022. 45, 47

Bayerer, R.; Herrmann, T.; Licht, T.; Lutz, J.; Feller, M. Model for power cycling lifetime of igbt modules – various factors influencing lifetime. *CIPS*, 2008. 57

Bierhoff, M. H.; Fuchs, F. W. Semiconductor losses in voltage source and current source igbt converters based on analytical derivation. *2004 IEEE PESC*, v. 4, p. 2836–2842 Vol.4, 2004. 67

Brito, E. M. d. S. *Lifetime Evaluation of Photovoltaic Inverters with Capability of Reactive Power Support*. Thesis (Ph.D.) — Federal University of Minas Gerais, 2021. 57, 59

Brito, E. M. da S.; Cupertino, A. F.; Pereira, H. A.; Mendes, V. F. Reliability-based trade-off analysis of reactive power capability in pv inverters under different sizing ratio. *International Journal of Electrical Power & Energy Systems*, v. 136, p. 107677, 2022. ISSN 0142-0615. 45, 47

Burkart, R.; Kolar, J. W. Component cost models for multi-objective optimizations of switched-mode power converters. In: *2013 IEEE Energy Conversion Congress and Exposition*. 2013. p. 2139–2146. 100

Cabana-Jiménez, K.; Candelo-Becerra, J. E.; Sousa Santos, V. Comprehensive analysis of microgrids configurations and topologies. *Sustainability*, v. 14, n. 3, 2022. ISSN 2071-1050. Available in: <https://www.mdpi.com/2071-1050/14/3/1056>. 38

Callegari, J.; Silva, M.; de Barros, R.; Brito, E.; Cupertino, A.; Pereira, H. Lifetime evaluation of three-phase multifunctional pv inverters with reactive power compensation. *Electric Power Systems Research*, v. 175, p. 105873, 2019. ISSN 0378-7796. Available in: <https://www.sciencedirect.com/science/article/pii/S0378779619301865>. 12, 45

Cargill. *FR3 fluid properties: standard acceptance values and typical values*. 2021. 7 p. Available in: <https://www.cargill.com/doc/1432160189547/fr3-dielectric-fluid-data-sheet.pdf>. 116

Chen, S.; Chen, Z.; Yu, W. Multiple pr current regulator based dead-time effects compensation for grid-forming single-phase inverter. In: *IEEE Energy Conversion Congress and Exposition*. 2018. p. 3134–3141. 62

Chilipi, R. S. R.; Al Sayari, N.; Al Hosani, K. H.; Beig, A. R. Adaptive notch filter-based multipurpose control scheme for grid-interfaced three-phase four-wire dg inverter. *IEEE Trans. Ind. Appl.*, v. 53, n. 4, p. 4015–4027, 2017. 31

Choi, U.-M.; Blaabjerg, F.; Lee, K.-B. Study and handling methods of power igbt module failures in power electronic converter systems. *IEEE Transactions on Power Electronics*, v. 30, n. 5, p. 2517–2533, 2015. 12, 44

Ciappa, M. Selected failure mechanisms of modern power modules. *Microelectronics Reliability*, v. 42, n. 4, p. 653–667, 2002. ISSN 0026-2714. Available in: <https://www.sciencedirect.com/science/article/pii/S0026271402000422>. 45

Cruz, E. C. A.; Aniceto, L. A. *INSTALAÇÕES ELÉTRICA: fundamentos, práticas e projetos em instalações residnciais e comerciais*. : Editora Érica, 2019. 76

Cupertino, A. F.; Lenz, J. M.; Brito, E. M.; Pereira, H. A.; Pinheiro, J. R.; Seleme, S. I. Impact of the mission profile length on lifetime prediction of pv inverters. *Microelectronics Reliability*, v. 100-101, p. 113427, 2019. ISSN 0026-2714. 30th European Symposium on Reliability of Electron Devices, Failure Physics and Analysis. Available in: <https://www.sciencedirect.com/science/article/pii/S0026271419305438>. 45

dos Santos Jr., E. C.; Alibeik, M. Microgrid system with voltages in quadrature. *IEEE Energy Conversion Congress and Exposition*, 2015. 41, 47

Drofekik, U.; Laimer, G.; Kolar, J. W. Theoretical converter power density limits for forced convection cooling. *International Conference on Power Electronics Intelligent Motion Power Quality.*, p. 608 – 619, 2005. 101, 102

Drofenik, U.; Kolar, J. W. Analyzing the theoretical limits of forced air-cooling by employing advanced composite materials with thermal conductivities > 400w/mk. In: *4th International Conference on Integrated Power Systems*. 2006. p. 1–6. 102

EMC. *Weather Station. Federal University of Goias (UFG) - School of Electrical, Mechanical and Computer Engineering (EMC)*. 2022. Available in: <https://sites.google.com/site/sfvemcufg/weather-station>. 95

EPE. *solated systems. Planning of assistance to Isolated System. Horizon 2024 - Cycle 2019*. 2019. Available in: <https://www.epe.gov.br/sites-pt/publicacoes-dados-abertos/publicacoes/PublicacoesArquivos/publicacao-452/EPE-NT-Planejamento%20SI-ciclo_2019_rev1.pdf>. Access in: June 21, 2021. 29

EPE. *Planning of assistance to Isolated System. Horizon 2023-2027 - Cycle 2022*. 2022. 12, 28, 29

Fajardo, M.; Viola, J.; Restrepo, J.; Quizhpi, F.; Aller, J. Two-phase active power filter direct current control with capacitor voltages estimation and balance. In: *2015 IEEE Workshop on Power Electronics and Power Quality Applications (PEPQA)*. 2015. p. 1–6. 40, 47

Falck, J.; Felgemacher, C.; Rojko, A.; Liserre, M.; Zacharias, P. Reliability of power electronic systems: An industry perspective. *IEEE Ind. Electron. Mag.*, v. 12, n. 2, p. 24–35, 2018. 44

Fani, B.; Shahgholian, G.; Haes Alhelou, H.; Siano, P. Inverter-based islanded microgrid: A review on technologies and control. *e-Prime - Advances in Electrical Engineering, Electronics and Energy*, v. 2, p. 100068, 2022. ISSN 2772-6711. Available in: <https://www.sciencedirect.com/science/article/pii/S2772671122000407>. 16, 39

Fearnside, P. M. *Hidrelétricas na Amazônia: impactos ambientais e sociais na tomada de decisões sobre grandes obras*. 2015. Available in: <https://repositorio.inpa.gov.br/bitstream/1/4684/1/hidreletricas_na_Amazonia_v1.pdf>. Access in: October 10, 2023. 31

Ferreira, V. d. N. *Confiabilidade de Inversores: Avaliação e Redução dos Efeitos de Ciclos Térmicos em Módulos de Potência.* Thesis (Ph.D.) — Federal University of Minas Gerais, 2016. 43, 44

Fortescue, C. L. Method of symmetrical co-ordinates applied to the solution of polyphase networks. *Transactions of the American Institute of Electrical Engineers*, v. 37, n. 2, p. 1027–1140, 1918. 41

Furtado, P. C. d. S.; Barbosa, P. G. Model predictive controller for two-phase three-wire grid-connected converters. In: *2019 IEEE 15th Brazilian Power Electronics Conference and 5th IEEE Southern Power Electronics Conference (COBEP/SPEC)*. 2019. p. 1–6. 12, 31, 32, 40, 47

Furtado, P. C. d. S.; Barbosa, P. G.; Rodrigues, M. d. C. B. P. A shunt active compensation strategy with zero neutral current in two-phase three-wire systems. In: *2015 IEEE Eindhoven PowerTech*. 2015. p. 1–5. 40, 47

Furtado, P. C. d. S.; Rodrigues, M. d. C. B. P.; Barbosa, P. G. Adaptation of the instantaneous power theory for two-phase three-wire systems and its application in shunt active power filters. In: *2015 IEEE 13th Brazilian Power Electronics Conference and 1st Southern Power Electronics Conference (COBEP/SPEC)*. 2015. p. 1–5. 40

Furtado, P. C. de S. *Contributions to power conditioning techniques in two-phase three-wire electric networks*. Thesis (Ph.D.) — Federal University of Juiz de Fora, 2019. 16, 32

Furtado, P. C. S.; Rodrigues, M. C. B. P.; Braga, H. A. C.; Barbosa, P. G. Two-phase three-wire shunt active power filter control by using the single-phase p-q theory. In: *Brazilian Power Electron. Journal (SOBRAEP)*. 2014. v. 19, n. 3, p. 03–311. 40

Gopalakrishnan, K. S.; Das, S.; Narayanan, G. Analytical expression for rms dc link capacitor current in a three-level inverter. *Centenary Conference - Electrical Engeneering*, 2011. 79

Graovac, D.; Purschel, M. Igbt power losses calculation using the data-sheet parameters. In: *Infineon Technologies AG, Neubiberg, Germany*. 2009. 53

Gupta, A.; Doolla, S.; Chatterjee, K. Hybrid ac–dc microgrid: Systematic evaluation of control strategies. *IEEE Transactions on Smart Grid*, v. 9, n. 4, p. 3830–3843, 2018. 38

Gyamfi, K. S.; Gaura, E.; Brusey, J.; Trindade, A. B.; Verba, N. Understanding household fuel choice behaviour in the amazonas state, brazil: Effects of validation and feature selection. *Energies*, v. 13, n. 15, 2020. ISSN 1996-1073. Available in: <https://www.mdpi.com/1996-1073/13/15/3857>. 29, 30, 33, 60

Henry, L. *Design and implementation of off-grid systems*. : Springer International Publishing, 2018. (Off-Grid Electrical Systems in Developing Countries). 31

IBGE. *National Household Sample Survey(Pesquisa Nacional por Amostra de Domicílios)*. 2019. Available in: <https://educa.ibge.gov.br/jovens/conheca-o-brasil/populacao/21130-domicilios-brasileiros.html>. Access in: June 21, 2021. 28

IEA. *For the first time in decades, the number of people without access to electricity is set to increase in 2022*. 2022. Available in: <https://www.iea.org/commentaries/for-the-first-time-in-decades-the-number-of-people-without-access-to-electricity-is-set-to-increase-in-2 Access in: October 18, 2023. 12, 27

IEEE. Ieee guide for selecting and using reliability predictions based on ieee 1413. *IEEE Std 1413.1-2002*, p. 1–106, 2003. 43, 44

IEEE. Standard framework for the reliability prediction of hardware. 2009. 42

IEMA. *Um milhão estão sem energia elétrica na Amazônia, mostra IEMA*. 2019. Available in: <https://energiaeambiente.org.br/um-milhao-estao-sem-energia-eletrica-na-amazonia-20191125>. 28

Infineon. Infineon. transient thermal measurements and thermal equivalent circuit models. v. 1.2, 2020. 54

IRENA. Off-grid renewable energy solutions. 2018. 37

IRENA. Off-grid renewable energy statistics 2022. 2022. 12, 27, 28

Jahns, T. M.; Dai, H. The past, present, and future of power electronics integration technology in motor drives. *CPSS Transactions on Power Electronics and Applications*, v. 2, n. 3, p. 197–216, 2017. 112

J.Bryan; Duke, R.; Round, S. Decentralized generator scheduling in a nanogrid using dc bus signaling. In: *IEEE Power Engineering Society General Meeting, 2004.* 2004. p. 977–982 Vol.1. 40

Kaleybar, H. J.; Kojabadi, H. M.; Brenna, M.; Foiadelli, F.; Fazel, S. S. A two-phase three-wire quasi-z-source based railway power quality compensator for ac rail networks. In: *2017 IEEE International Conference on Environment and Electrical Engineering and 2017 IEEE Industrial and Commercial Power Systems Europe (EEEIC / I CPS Europe).* 2017. p. 1–6. 41

Kanavaros, D.; Oriti, G.; Julian, A. L. Novel implementation and comparison of active and reactive power flow control methods in a single phase grid-connected microgrid. *IEEE Trans. Ind. Appl.*, v. 56, n. 2, p. 1631–1639, 2020. 31

Kasal, G. K.; Singh, B. Voltage and frequency controllers for an asynchronous generator-based isolated wind energy conversion system. *IEEE Trans. Energy Convers.*, v. 26, n. 2, p. 402–416, 2011. 31

Katiraei, F.; Iravani, R.; Hatziargyriou, N.; Dimeas, A. Microgrids management. *IEEE Power and Energy Magazine*, v. 6, n. 3, p. 54–65, 2008. 37, 38

Kersting, W. H. Center tapped transformer and 120/240 volt secondary models. In: *IEEE Rural Electric Power Conference.* 2008. p. A1–A1–7. 31, 41

Kshatri, S. S.; Dhillon, J.; Mishra, S.; Haghighi, A. T.; Hunt, J. D.; Patro, E. R. Comparative reliability assessment of hybrid si/sic and conventional si power module based pv inverter considering mission profile of india and denmark locations. *Energies*, v. 15, n. 22, 2022. ISSN 1996-1073. Available in: <https://www.mdpi.com/1996-1073/15/22/8612>. 45, 47

Lenz, J. M.; Pinheiro, J. R. Mission profile impact on capacitor reliability in pv single-stage inverters. In: *International Conference on Renewable Energy Research and Applications.* 2018. p. 976–981. 58

Li, Y.; Vilathgamuwa, D. M.; Loh, P. C. Microgrid power quality enhancement using a three-phase four-wire grid-interfacing compensator. *IEEE Trans. Ind. Appl.*, v. 41, n. 6, p. 1707–1719, 2005. 31

Lidula, N.; Rajapakse, A. Voltage balancing and synchronization of microgrids with highly unbalanced loads. *Renewable and Sustainable Energy Reviews*, v. 31, p. 907–920, 2014. ISSN 1364-0321. Available in: <https://www.sciencedirect.com/science/article/pii/S1364032113008599>. 40

Lopes, J.; Moreira, C.; Madureira, A. Defining control strategies for microgrids islanded operation. *IEEE Transactions on Power Systems*, v. 21, n. 2, p. 916–924, 2006. 40

Lotfi, H.; Khodaei, A. Hybrid ac/dc microgrid planning. *Energy*, v. 118, p. 37–46, 2017. ISSN 0360-5442. Available in: <https://www.sciencedirect.com/science/article/pii/S0360544216318175>. 38

Lutz, J.; Schwabe, C.; Zeng, G.; Hein, L. Validity of power cycling lifetime models for modules and extension to low temperature swings. In: *2020 22nd European Conference on Power Electronics and Applications (EPE'20 ECCE Europe)*. 2020. p. P.1–P.9. 57

Ma, K.; Blaabjerg, F. The impact of power switching devices on the thermal performance of a 10 mw wind power npc converter. *Energies*, v. 5, n. 7, p. 2559–2577, 2012. ISSN 1996-1073. Available in: <https://www.mdpi.com/1996-1073/5/7/2559>. 44

Ma, K.; Blaabjerg, F. Reliability-cost models for the power switching devices of wind power converters. In: *IEEE International Symposium on Power Electronics for Distributed Generation Systems (PEDG)*. 2012. p. 820–827. 56

Ma, K.; Blaabjerg, F.; Liserre, M. Electro-thermal model of power semiconductors dedicated for both case and junction temperature estimation. In: *Proc. PCIM*. 2013. p. 1042–1046. 54

Mahanta, D. K. Green transformer oil: A review. In: *2020 IEEE International Conference on Environment and Electrical Engineering and 2020 IEEE Industrial and Commercial Power Systems Europe (EEEIC / I&CPS Europe)*. 2020. p. 1–6. 112

Martin, D. *Evaluation of the dielectric capability of ester based oils for power transformers*. Thesis (Ph.D.) — The University of Queensland, 2008. 16, 113

Nellis, G.; Klein, S. *Introduction to Engineering Heat Transfer*. : Cambridge United Kingdom: Cambridge University Press, 2021. 16, 113

Nieslony, A. Rainflow counting algorithm. *MATLAB File Exchange Central*, 2003. 56

NREL, N. R. E. L. *National Solar Radiation Database*. 2023. Available in: <https://nsrdb.nrel.gov/>. 60

O'Connor, P. D. T.; Kleyner, A. *Practical Reliability Engineering*. : Wiley, 2012. 41, 42, 43

Pecht, M.; Dasgupta, A. Physics-of-failure: An approach to reliable product development. In: *Proc. Int. Integrated Reliability*. 1995. p. 14. 43

Pei, X.; Kang, Y.; Chen, J. Analysis and calculation of dc-link current and voltage ripple for three-phase inverter with unbalanced loads. *IEEE Trans. Power Electron.*, 2015. 79

Peyghami, S.; Wang, H.; Davari, P.; Blaabjerg, F. Mission-profile-based system-level reliability analysis in dc microgrids. *IEEE Transactions on Industry Applications*, v. 55, n. 5, p. 5055–5067, 2019. 45, 47

Pires, I. A.; Silva, R. A.; Pereira, I. T. O.; Faria, O. A.; Maia, T. A. C.; Filho, B. d. J. C. An assessment of immersion cooling for power electronics: An oil volume case study. *IEEE Transactions on Industry Applications*, v. 56, n. 3, p. 3231–3237, 2020. 112

Planas, E.; Andreu, J.; Gárate, J. I.; Martínez de Alegría, I.; Ibarra, E. Ac and dc technology in microgrids: A review. *Renewable and Sustainable Energy Reviews*, v. 43, p. 726–749, 2015. ISSN 1364-0321. Available in: <https://www.sciencedirect.com/science/article/pii/S1364032114010065>. 38, 40

Reigosa, P. *Smart Derating of Switching Devices for Designing More Reliable PV Inverters*. Thesis (Master) — Power Electronics and Drives, Department of Energy Technology Aalborg University, 2014. 45

Reigosa, P. D.; Wang, H.; Yang, Y.; Blaabjerg, F. Prediction of bond wire fatigue of igbts in a pv inverter under a long-term operation. *IEEE Trans. Power Electron.*, v. 31, n. 10, p. 7171–7182, 2016. 58, 59

Rocha, A. V. *Confiabilidade e Resiliência de Conversores de Média Tensão Baseados em IGCT*. Thesis (Ph.D.) — Federal University of Minas Gerais, 2014. 41, 42, 43

Rodrigues, M. C. B. P.; Furtado, P. C. S.; Rodrigues, C. R. B. S.; Ferreira, R. A. F.; Ferreira, A. A.; Barbosa, P. G.; Braga, H. A. C. Development of a small-signal model for a two-phase three-wire active power filter. *Brazilian Power Electronics Conference (COBEP)*, 2017. 40

Sangwongwanich, A.; Blaabjerg, F. Reliability assessment of fault-tolerant power converters including wear-out failure. In: *2022 IEEE Applied Power Electronics Conference and Exposition (APEC)*. 2022. p. 300–306. 45, 47

Sangwongwanich, A.; Yang, Y.; Sera, D.; Blaabjerg, F. Lifetime evaluation of grid-connected pv inverters considering panel degradation rates and installation sites. *IEEE Trans. Pow. Elect.*, v. 33, n. 2, p. 1225–1236, 2018. 45, 59

Sangwongwanich, A.; Zhou, D.; Liivik, E.; Blaabjerg, F. Mission profile resolution impacts on the thermal stress and reliability of power devices in pv inverters. *Microelectronics Reliability*, v. 88-90, p. 1003–1007, 2018. ISSN 0026-2714. 29th European Symposium on Reliability of Electron Devices, Failure Physics and Analysis (ESREF 2018). Available in: <https://www.sciencedirect.com/science/article/pii/S0026271418305158>. 45

Schmidt, R.; Zeyss, F.; Scheuermann, U. Impact of absolute junction temperature on power cycling lifetime. In: *2013 15th European Conference on Power Electronics and Applications (EPE)*. 2013. p. 1–10. 57

Schonbergerschonberger, J.; Duke, R.; Round, S. Dc-bus signaling: A distributed control strategy for a hybrid renewable nanogrid. *IEEE Transactions on Industrial Electronics*, v. 53, n. 5, p. 1453–1460, 2006. 40

Silva, R.; de Barros, R.; Boaventura, W.; Cupertino, A.; Pereira, H. Correction strategy for wear-out prediction of pv inverters considering the mission profile resolution effects. *Microelectronics Reliability*, v. 135, p. 114605, 2022. ISSN 0026-2714. Available in: <https://www.sciencedirect.com/science/article/pii/S0026271422001299>. 45

Silva, R. M.; Brandao, D. I.; Fogli, G. A.; Mendes, V. F.; Sousa, C. V. Comparison among two-phase three-wire ac off-grid power systems. In: *IEEE 15th Brazilian Power Electronics Conference and 5th IEEE Southern Power Electronics Conference*. 2019. p. 1–6. 46, 47, 49

Sintamarean, N.; Wang, H.; Blaabjerg, F.; Rimmen, P. P. A design tool to study the impact of mission-profile on the reliability of sic-based pv-inverter devices. *Microelectronics Reliability*, v. 54, n. 9, p. 1655–1660, 2014. ISSN 0026-2714. SI: ESREF 2014. Available in: <https://www.sciencedirect.com/science/article/pii/S0026271414002510>. 45

Song, Y.; Wang, B. Survey on reliability of power electronic systems. *IEEE Trans. Power Electron.*, 2013. 33, 45, 52, 59

Sousa, R. O. d. *Proposal of Minimum SM Voltage Control for Losses Reduction and Reliability Improvement in MMC-based STATCOM.* Thesis (Ph.D.) — Federal University of Minas Gerais, 2022. 54

Trindade, A.; Cordeiro, L. Automated formal verification of stand-alone solar photovoltaic systems. *Solar Energy*, v. 193, p. 684–691, 2019. ISSN 0038-092X. Available in: <https://www.sciencedirect.com/science/article/pii/S0038092X1930965X>. 28

Tuma, P. E. The merits of open bath immersion cooling of datacom equipment. In: *2010 26th Annual IEEE Semiconductor Thermal Measurement and Management Symposium (SEMI-THERM)*. 2010. p. 123–131. 112

Turnbull, J. E.; Venkataramanan, G.; Ludois, D. Experimental evaluation of liquid immersed electronics for high density power converters. In: *2023 IEEE Applied Power Electronics Conference and Exposition (APEC)*. 2023. p. 1600–1607. 112

Ushakov, I. A. *Probabilistic reliability models.* : Wiley, 2012. 42

Viola, J.; Fajardo, M.; Aller, J. M.; Restrepo, J.; Quizhpi, F. Grid connected inverter with active power filter capabilities for two-phase systems. *IEEE Third Ecuador Technical Chapters Meeting*, 2018. 40, 47

Wang, H.; Li, C.; Zhu, G.; Liu, Y.; Wang, H. Model-based design and optimization of hybrid dc-link capacitor banks. *IEEE Trans. Power Electron.*, 2020. 54

Wang, H.; Liserre, M.; Blaabjerg, F.; de Place Rimmen, P.; Jacobsen, J. B.; Kvisgaard, T.; Landkildehus, J. Transitioning to physics-of-failure as a reliability driver in power electronics. *IEEE Trans. Emerg. Sel. Topics Power Electron.*, v. 2, n. 1, p. 97–114, 2014. 44

Wang, H.; Ma, K.; Blaabjerg, F. Design for reliability of power electronic systems. In: *IECON 2012 - 38th Annual Conference on IEEE Industrial Electronics Society*. 2012. p. 33–44. 43

Wu, C.; Luo, A.; Shen, J.; Ma, F. J.; Peng, S. A negative sequence compensation method based on a two-phase three-wire converter for a high-speed railway traction power supply system. *IEEE Transactions on Power Electronics*, v. 27, n. 2, p. 706–717, 2012. 41

Yang, Y.; Sangwongwanich, A.; Blaabjerg, F. Design for reliability of power electronics for grid-connected photovoltaic system. *CPSS Transactions on Power Electronics and Applications*, v. 1, n. 1, p. 92–103, 2016. 45, 59

Yepes, A. G.; Freijedo, F. D.; Lopez Óscar; Doval-Gandoy, J. Analysis and design of resonant current controllers for voltage-source converters by means of nyquist diagrams and sensitivity function. *IEEE Transactions on Industrial Electronics*, v. 58, n. 11, p. 5231–5250, 2011. 62

Biography

João Henrique de Oliveira born in 09/21/1989 in Timóteo – MG, received the B.S. degree in electrical engineering in 2014 from Federal University of Viçosa (UFV), the M.S. degree in 2016, and the Ph.D. degree in 2024 from the Federal University of Minas Gerais (UFMG). His main interests are control and reliability of power converters, microgrid control and power quality. He is a member of IEEE.

E-mail: joao.holiveira@yahoo.com.br